Microelectrochemical imaging of corrosion reactions

Doctoral thesis

Author:
Dániel Filotás
Doctoral School of Chemistry,
Department of General and Physical Chemistry

Doctoral supervisors:
Dr. Lívia Nagy
Prof. Dr. Géza Nagy
Co-supervisor:
Prof. Dr. Ricardo M. Souto

Head of the Doctoral School:
Prof. Dr. Ferenc Kilár

University of Pécs, 2018.

Contents

Preface 5
Contribution statement 6
Publications not included in the dissertation 6
Acknowledgements 9
Motivation 10
Aims of the work 11
Part I. Introduction 12
I.1. Scanning Electrochemical Microscopy (SECM) 12
I.1.1. Modes of the SECM 13
I.1.2. Feedback mode 14
I.1.3. Generator/collector modes 15
I.1.3. Redox competition mode 16
I. 1.4. Potentiometric mode 16
I.2. Electric field measurements with the Scanning Vibrating Electrode Technique (SVET) 18
I.3. Ion selective electrodes (ISE) 22
I.3.1. Brief history of ISE development 22
I.3.2. The theory of the ionophore based ion selective electrode response 23
I.3.2. Role of the membrane components 24
I.3.3. The phase boundary model (PBM) 25
I.3.4. The diffusion layer model (DLM) 26
I.3.5. The Nernst-Planck-Poisson Model (NPP) 27
I.3.6. Practical potentiometric measurements 28
I.3.8. Application of ion selective microelectrodes in corrosion research 29
I.3.9. Multi-barrel microelectrodes in life sciences 30
I.3.10. Multi-barrel electrodes in SECM studies 30
I.4. Fundamentals of magnesium corrosion 32
I.4.1. Magnesium corrosion 32
I.4.2. Anomalous hydrogen evolution on anodically polarized magnesium 33
I.4.3. Electrochemical testing of magnesium corrosion 39
3.5. Remarks on the magnesium corrosion 40
Part II. Experimental 41
II.1. Materials 41
II.2. Equipments 42
II.2.2. Applied potentiostats 42
II.3. Scanning electrochemical microscopy 42
II.4. Scanning vibrating electrode technique 43
II.5. Samples 44
II.6. Electrodes 46
II.6.1. Preparation of the Pt microelectrodes 46
II.6.2. Preparation of the pH sensitive antimony microelectrodes 46
II.6.3. Preparation of the ion selective microelectrodes 47

II.6.4. Preparation of multi-barrel electrodes 49
II.6.5. Calibration of the ion selective microelectrodes 53
II.6.6. Measurement of the dynamic response of the microelectrodes 55
II.6.7. Characterization of the Cu ISME 56
II.6.8. Examination of the "cross-talk" effect of the double-barrel electrodes 60
II.6.9.The possibility of enhanced selectivity obtained in simultaneous measurements .. 61
II.6.10. Establishment of the probe-sample distance in potentiometric SECM 63
Part III. Results and Discussion 66
Chapter 1 66
Double-barrel electrodes for SECM imaging of the corrosion of Zn-based materials 66
III.1.1. Resume 66
III.1.2. Simultaneous measurement of Zn^{2+} dissolution and pH distribution above the Zn-Fe galvanic pair 66
III.1.3. Imaging the cut edge of galvanized steel 68
III.1.4. Transient signal of the ISME's 70
III.1.5. Simultaneous operation of the Zn and Cu ISME containing double barrel above Cu^{2+} and Zn^{2+} point sources 72
Chapter 2 75
Potentiometric SECM imaging of the galvanic corrosion of Mg 75
III.2.1. Resume 75
III.2.2. Electric field effects on the potentiometric signal 76
III.2.3. Elimination of the electric field effects using double-barrel electrodes 81
III.2.4. SECM imaging of the corrosion reactions of magnesium 83
Chapter 3 89
Investigation of hydrogen evolution on anodically polarized magnesium 89
III.3.1. Resume 89
III.3.2. General comparison of the corrosion of pure Mg and AZ63 alloy 90
III.3.3. Effect of the nodic polarization on hydrogen evolution 91
III.3.4. Effect of Mg^{2+} ions on the hydrogen evolution rate 95
III.3.5. Effect of a complexing agent for Mg^{2+} ion on the hydrogen evolution rate 99
III.3.6. SVET measurements on anodically polarized samples 100
Chapter 4 102
Investigation of the anomalous hydrogen evolution on magnesium during galvanic corrosion 102
III.4.1. Resume 102
III.4.2. SVET measurements above the AZ63 anode of the AZ63/Fe galvanic pair 102
III.4.3. Characterization of the Mg-Al galvanic pair 105
III.4.4. Hydrogen evolution on the Mg-Al galvanic couple in the presence of Mg^{2+} ions 107
III.4.5. Hydrogen evolution on the Mg-Al galvanic couple in the presence of EDTA .. 109
Conclusions 111
References 112

Preface

The work this dissertation based on was carried out mainly at the University of Pécs and partly at the University of La Laguna, Spain. Although the thesis contains unpublished results, as well, it is based on the following publications:

1. D. Filotás, B. M. Fernández-Pérez, J. Izquierdo, L. Nagy, G. Nagy, R. M. Souto
   Novel dual microelectrode probe for the simultaneous visualization of local Zn^{2+} and pH distributions in galvanic corrosion processes
   ***CORROSION SCIENCE* 114:** pp. 37-44. (2017)
   (IF: 5.245, D1)

2. D. Filotás, A. Asserghine, L. Nagy, G. Nagy
   Short-term influence of interfering ion activity change on ion-selective micropipette electrode potential; another factor that can affect the time needed for imaging in potentiometric SECM
   ***ELECTROCHEMISTRY COMMUNICATIONS* 77**: pp. 62-64. (2017)
   (IF: 4.396, Q1)

3. D. Filotás, B. M. Fernández-Pérez, J. Izquierdo, A. Kiss, L. Nagy, G. Nagy, R. M. Souto
   Improved potentiometric SECM imaging of galvanic corrosion reactions
   ***CORROSION SCIENCE* 129:** pp. 136-145. (2017)
   (IF: 5.245, D1)

4. D. Filotás, B. M. Fernández-Pérez, A. Kiss, L. Nagy, G. Nagy, R. M. Souto
   Double barrel microelectrode assembly to prevent electrical field effects in potentiometric SECM imaging of galvanic corrosion processes
   ***JOURNAL OF THE ELECTROCHEMICAL SOCIETY* 165:** pp C270-C277
   (IF: 3.259, Q1)

5. D. Filotás, B. M. Fernández-Pérez, L. Nagy, G. Nagy, R M Souto
   An investigation of hydrogen generation from anodically polarized AZ63 magnesium alloy using scanning microelectrochemical methods
   JOURNAL OF THE ELECTROCHEMICAL SOCIETY (submitted)
   (IF: 3.259, Q1)

Contribution statement

The results shown in this dissertation are obtained in own experimental work under the supervision of Dr. Lívia Nagy, Prof. Dr. Géza Nagy and the co-supervision of Prof. Dr. Ricardo M. Souto. The first drafts of the papers were written entirely by me and I always tried to do the lion's share of the revisions, as well. The SVET experiments performed in La Laguna were carried out with the help of B. M. Fernández Pérez. Publication 2 is based on shared work with A. Asserghine. Publication 4 is a continuation of the common work started with A. Kiss (for the preliminary work, see ref. 160.)

Publications not included in the dissertation

1. R. M. Souto, D. Filotás, B. M. Fernández-Pérez, L. Nagy, G. Nagy
New developments in scanning microelectrochemical techniques: A highly sensitive route to evaluate degradation reactions and protection methods with chemical selectivity
***APPLIED MECHANICS AND MATERIALS* 875:** pp 19-23. (2018)

2. D. Filotás, T. Nagy, L. Nagy, P. Mizsey, G. Nagy
Extended investigation of electrochemical CO_2 reduction in ethanolamine solutions by SECM
***ELECTROANALYSIS* 30:** pp. 690-697. (2018)
(IF: 2.851, Q2)

3. A. Asserghine, D. Filotás, L. Nagy, G. Nagy
Scanning electrochemical microscopy investigation of the rate of formation of a passivating TiO_2 layer on a Ti G4 dental implant
***ELECTROCHEMISTRY COMMUNICATIONS* 83:** pp. 33-35. (2017)
(IF: 4.396, Q1)

4. A. Kiss, D. Filotás, R. M. Souto, G. Nagy
The effect of electric field on potentiometric Scanning Electrochemical Microscopic imaging
***ELECTROCHEMISTRY COMMUNICATIONS* 77:** pp. 138-141. (2017)
(IF: 4.396, Q1)

5. A. El Jaouhari, A. El Asbahani, M. Bouabdallaoui, Z. Aouzal, D. Filotás, E.A. Bazzaoui, L. Nagy, G. Nagy, M. Bazzaoui, A. Albourine, D. Hartmann
Corrosion resistance and antibacterial activity of electrosynthesized polypyrrole
***SYNTHETIC METALS* 226**: pp. 15-24. (2017)
(IF: 2.435, Q2)

6. D. Filotás, I. Z. Bátai, G. Pozsgai, L. Nagy, E. Pintér, G. Nagy
Highly sensitive potentiometric measuring method for measurement of free H_2S in physiologic samples
***SENSORS AND ACTUATORS B-CHEMICAL* 243:** pp. 326-331. (2017)
(IF: 5.401, Q1)

7. D. Filotás, B. M. Fernández-Pérez, J. Izquierdo, L. Nagy, G. Nagy, R. M. Souto
Combined amperometric/potentiometric probes for improved chemical imaging of corroding surfaces using Scanning Electrochemical Microscopy
***ELECTROCHIMICA ACTA* 221:** pp. 48-55. (2016)
(IF: 4.798, Q1)

8. Z. Hajna, E. Saghy, M. Payrits, A. A. Aubdool, E. Szoke, G. Pozsgai, I. Z. Batai, L. Nagy, D. Filotas, Z. Helyes, S. D. Brain, E. Pinter
Capsaicin-sensitive sensory nerves mediate the cellular and microvascular effects of H_2S via TRPA1 receptor activation and neuropeptide release.
***JOURNAL OF MOLECULAR NEUROSCIENCE* 60:**(2) pp. 157-170. (2016)
(IF: 2.229, Q3)

9. J. Izquierdo, B.M. Fernández-Pérez, D. Filotás, Z. Őri, A. Kiss, R. T. Martín-Gómez, L. Nagy, G. Nagy, R. M. Souto
Imaging of concentration distributions and hydrogen evolution on corroding magnesium exposed to aqueous environments using scanning electrochemical microscopy
***ELECTROANALYSIS* 28:**(10) pp. 2354-2366. (2016)
(IF: 2.851, Q2)

10. A. El Jaouhari, D. Filotás, A. Kiss, M. Laabd, E. A. Bazzaoui, L. Nagy, G. Nagy, A. Albourine, J. I. Martins, R. Wang, M. Bazzaoui
SECM investigation of electrochemically synthesized polypyrrole from aqueous medium
***JOURNAL OF APPLIED ELECTROCHEMISTRY* 46:**(12) pp. 1199-1209. (2016)
(IF: 2.235, Q2)

11. D. Filotás, L. Nagy, R. Skoda-Földes, L. Kollár, G. Nagy
Electrochemical experimental study for the characterization of tetraferrocenyl-cavitand, synthetized in click-reaction
***ELECTROANALYSIS* 27:**(1) pp. 38-41. (2015)
(IF: 2.471, Q2)

12. D. Filotás, L. Nagy, T. R. Kégl, Z. Csók, L. Kollár, G. Nagy
Synthesis and electrochemical properties of the tetraferrocenyl-cavitand in dimethyl formamide solvent using platinum and carbon working electrodes
***ELECTROANALYSIS* 27:**(3) pp. 799-807. (2015)
(IF: 2.471, Q2)

13. L. Nagy, D. Filotas, M. Boros, G. Pozsgai, E. Pinter, G. Nagy
Amperometric cell for subcutaneous detection of hydrogen sulfide in anesthetized experimental animals.
***PHYSIOLOGICAL MEASUREMENT* 35:**(12) pp. 2475-2487. (2014)
(IF: 1.576, Q2)

Cumulative impact factor: 56.255
h-index: 4
Citations: 30

Acknowledgements

First of all, I would like to express my greatest gratitude to Dr. Lívia Nagy and Prof. Dr. Géza Nagy for their continuous guidance and help since the day I started my work in their lab as a 2nd year bachelor student. All my scientific success is due to their competence, helpfulness, and dedication to science, their social capital and their ability to push students through their limits.

Ricardo M. Souto has also a remarkable contribution to my career. I have spent almost 5 months in his laboratories altogether. He is a great exemplar of how to be an excellent scientist and great musician at the same time. He gave me fascinating topics and treated me as family, when I was in Tenerife. ¡Gracias por todo!

Abdelilah Asserghine is a great friend of mine and a great example of how small the world is, as we have common friends in Morocco. I'd like to grab the opportunity here to thank him for his help in research, making an amicable atmosphere in our lab with the jokes we'll remember forever.

I know Bibiana Maria Fernández Pérez since 2014 and she is the most helpful person in the world. She introduced me SECM and SVET techniques during my master studies. I thank her being my guide in the lab and in Tenerife, as well.

I thank András Kiss, whose enthusiasm for research inspired me a lot during my studies and I learned a lot from him during the common work and discussions.

Apart from my ERASMUS trips, I had the opportunity to visit other laboratories during my PhD. Hence I express my appreciation for the hospitality to Dr. Mohammed Bazzaoui at the Ibn Zohr University, Morocco, Prof. Dr. Petr Skládal at the Masaryk University, Czech Republic and Prof. Dr. Frank-Michael Matysik at the University of Regensburg, Germany.

I am thankful to my family, all my professors, group mates, colleagues and friends who supported me during my studies and whom I can't mention here by name due to the limited space.

Pécs, 2018.

Dániel Filotás

Motivation

I hope the readers may forgive me for this very personal introduction, but I think my journey toward PhD studies in chemistry is worth a memento. In elementary school I didn't like chemistry. I have been waiting so much for the last chemistry class that when the day eventually came I ran a circle of triumph around the school. „Two more years in high school, then no more chemistry for my whole life"- I thought. Then it came to pass, in my second year of high school chemistry I realized that I started to like chemistry, as I was the only one in our class who understood the nomenclature of the organic compounds. Hence I enrolled the chemistry preparatory course for the early graduation exam. And another revelation came: I like the other parts of chemistry, too, except electrochemistry. So in short, I ended as a chemistry student at the University of Pécs. After the first year, there was a meeting where the professors introduced their research topics student can join and with their own results can participate the Scientific Students' Conference. Surprisingly, the most interesting topic for my taste was about *in vivo* H_2S measurements in anaesthetized mice using electrochemical sensors. Despite, it was electrochemistry, the topic itself aroused my interest, I decided to join professor Nagy's group. It turned out that my preconception was wrong again and electrochemical research is much more (and much more interesting) than what I learned before in high school. After the defense of my Bachelor's thesis, I started to work on another topic, the electrochemical characterization of tetraferrocenyl-cavitands. The results obtained were demonstrated in the national student research competition. It seemed to be obvious to use the same topic for writing my Master's thesis. But eventually, I didn't do so.

I was entitled for a 2-month ERASMUS traineeship to Tenerife, where I started to deal with ion selective microelectrodes and scanning electrochemical microscopy. I found the electrochemical imaging of corrosion processes a fascinating area and although I hesitated before, by the time I have arrived back to Hungary, I already knew that I would like to continue my studies in PhD. With shorter and longer intermezzos, I could continue the same topic that was moved to the investigation of Mg corrosion during my second stay in Tenerife. I focused on how to perform reliable potentiometric measurements on polarized magnesium and meanwhile I started to use the amperometric generator collector mode of the SECM to investigate the negative difference effect.

Although, during the 3 years, I was involved in many different projects, I decided to include these two main topics in this dissertation: enhanced imaging of corrosion reactions with ion selective microelectrodes and the investigation of the anomalous hydrogen evolution on anodically polarized magnesium.

Aims of the work

Corrosion reactions – anodic, cathodic half-cell and side reactions – are occurring simultaneously on the surfaces exposed to corrosive environment. Localized information helps to get a deeper insight into the degradation of materials and facilitates the development of new anti-corrosive treatments. Simultaneously collected, localized information is a great step further.

In order to obtain spatially resolved chemical information of multiple species in the same time, new type of electrodes has to be developed. Monitoring of pH changes along with metal-ion concentration is particularly attractive.

Metal-ion concentration in the adjacent solution can be readily measured using ion selective microelectrodes. However, poor selectivity can be a limiting factor in these measurements. The problem of selectivity was subdivided into two areas in this research: the role of the time-dependent selectivity coefficient was investigated, as well as the „conventional" selectivity coefficient, the one everybody knows from the Nikolsky equation.

As a trumpet player, I am interested in the corrosion of brass, but the lack of copper(II) ion selective microelectrode made the developement of the new ISME necessary.

In potentiometric SECM, the electrice field contribution in the case of polarized samples or galvanic corrosion is an old problem, I also faced in my earlier studies. This is very emphatic in the case of magnesium corrosion, hence from the zinc and copper based materials I turned my eyes toward magnesium.

Dealing with magnesium, I've seen peculiar behavior of magnesium anodes that is often referred as the „negative difference effect" in the literature. For this reason, as I finished with the electric field related experiments, I wanted to dig deeper into this problem. In this work, it seemed obvious to detect the hydrogen evolved on the magnesium surface that can be done amperometrically.

Although my results are sorted into 4 apparently independent chapters in the Results and discussion, one ensue from the other: as I started to work on something, my experiences inspired to next direction of the research.

Part I. Introduction

I.1. Scanning Electrochemical Microscopy (SECM)

Scanning probe microscopy (SPM) is a branch of the microscopy where the pixels of the eventual image are obtained by sequentially implemented local measurements. The computer constructs the image from the individual results of the local measurements. Profilometry may be regarded as the ancestor of this group, where the stylus is dragged over the surface and the tip deviations of the mean height was determined using a simple electric circuit [1]. In 1967, the technique was made 3 dimensional by Williamson et al. and showed that the asperities of surfaces follow the Gaussian distribution [2]. The invention of scanning tunneling microscopy (STM) became more widely known and more respected, as well, considering that the inventors, Binning and Rohrer received the Nobel prize in 1986 [3]. This pioneering work led to the invention of a series of other scanning probe techniques reaching several tens of different techniques distinguished by the probe or the operating principle.

Scanning Electrochemical Microscopy (SECM) is a special member in the family of the scanning probe techniques invented by Allen J. Bard in 1989 [4]. Spatially resolved, chemical information can be gathered from different surfaces or liquid/liquid, liquid-gas interfaces. The keyword here is chemical, since the electrochemical signal measured at each „pixel" can provide concentration distribution of different species besides the possibility of the recording of topographic images.

The illustration of the SECM instrument can be seen in **Fig 1**. The amperometric variant employs a three electrode setup, where the working electrode is moving above the sample according to the computer controlled 3D positioner. The electrochemical measurements and the polarization of the sample are implemented by the bipotentiostat that is controlled by the computer. The signal is amplified and acquired by the analog-to-digital converter. The data of local measurements are stored with the corresponding spatial and/or temporal coordinates.

The potentiometric SECM is often referred as scanning ion selective electrode technique (SIET), although the use of this term is mitigated throughout this work. It is very similar to the amperometric SECM, with the exception that a two electrode potentiometric cell is used for the measurements. A voltage follower is also interconnected between the electrodes and the measuring device. Merely a voltmeter can be used for the measurement, but in such case, no polarization on the sample can be done. Hence usually a bipotentiostat capable for voltage measurement and polarization is employed.

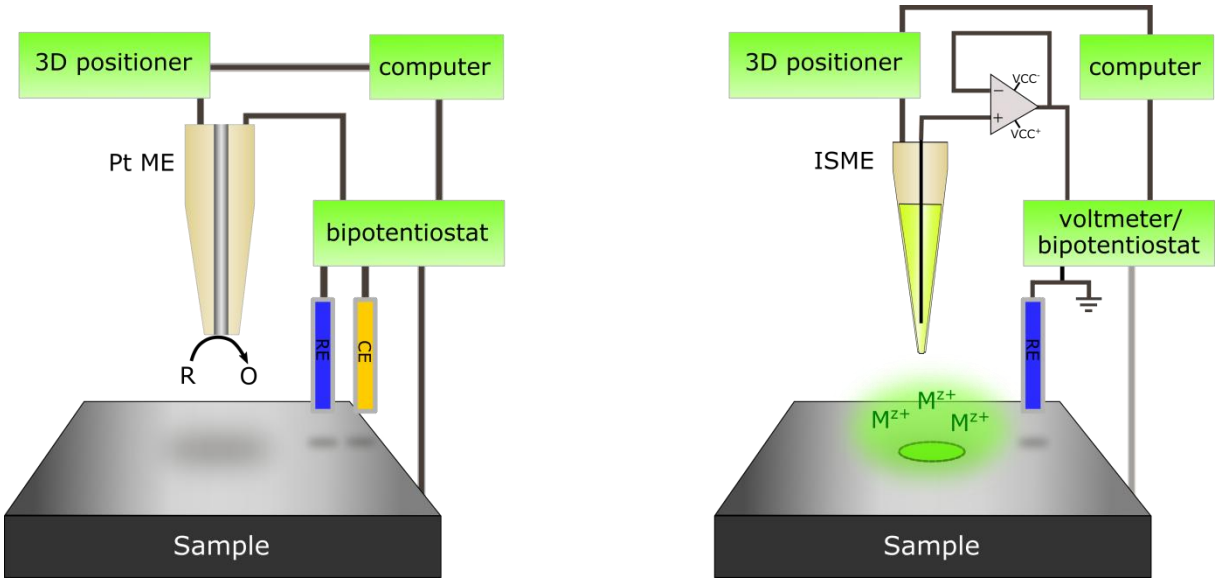

Fig 1. Schemes of the amperometric (left) and potentiometric (right) operation of the SECM.

I.1.1. Modes of the SECM

In this Section, the most often used modes of the amperometric SECM will be introduced briefly. In **Fig 2**, the schemes of these modes are depicted. **Fig 2A** demonstrates the hemispherical diffusion of the electroactive species toward the electrode surface. This is general for microelectrodes and happens in the bulk of the solution. *R* represents the reduced form of a reversible redox mediator. The potential of the microelectrode is kept at a potential where $R - ne^- \rightarrow O$ reaction occurs and controlled by diffusion. If it is so, the following equation applies for the current:

$$i_{t,\infty} = 4nFDac \qquad (1)$$

where *n* is the number of electrons involved in the electrode reaction, *F* is the Faraday constant, *D* is the diffusion coefficient of the mediator, *a* is the radius of the microelectrode, *c* is the concentration of the mediator.

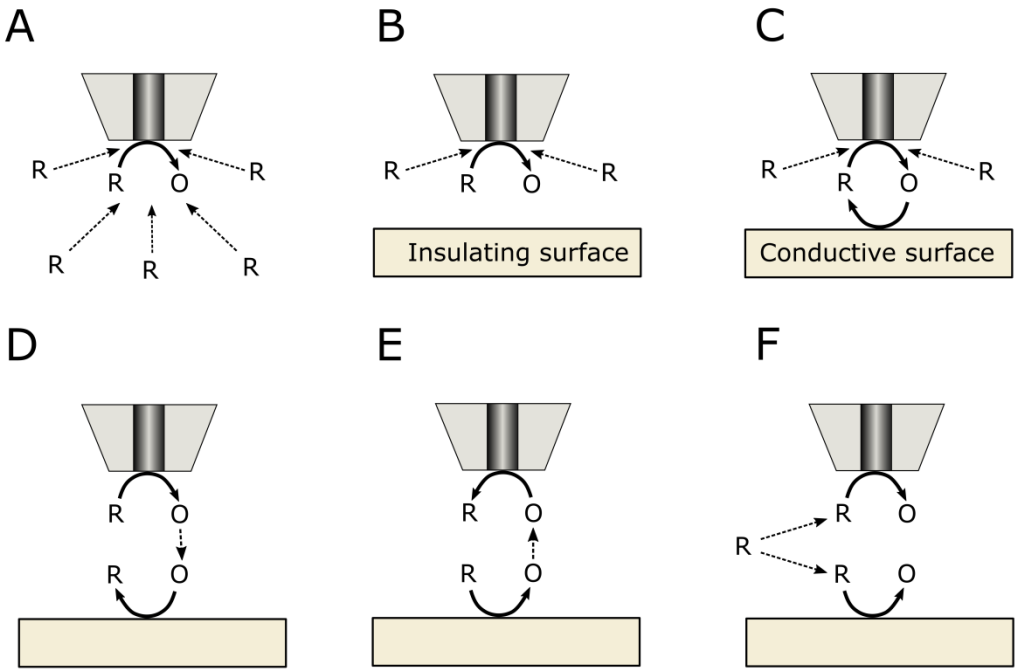

Fig 2. Operating modes of the amperometric SECM. A: hemispheric diffusion of the mediator toward the electrode surface, B: negative feedback effect, C: positive feedback effect, D: tip generator, sample collector mode (TG-SC), E: sample generator, tip collector mode (SG-TC), F: redox competition mode.

I.1.2. Feedback mode

If the tip is brought a few tip diameter distances from an insulating surface (**Fig 2B**), the current will decrease, because of the hindered mass transport of the mediator toward the microelectrode surface. This phenomenon called *negative feedback* has a definite distance dependence that is utilized in the SECM practice and can be described as follows:

$$\frac{i}{i_\infty} = \frac{1}{0.292 + 1.515\frac{a}{d} + 0.6553exp\left(-2.4035\frac{a}{d}\right)} \quad (2)$$

where i and i_∞ are the current and the limiting current, d is the distance from the insulating surface. The a/d quotient is often marked as L. It has to be mentioned that the constants in Eq (2) would be different if the RG value were different from 10. The RG value is the ratio of the diameter of the microelectrode counting the glass shield around the metal wire and the disk diameter.

If the tip approaches a conducting surface, the regeneration of the product of the electrode reaction can occur; hence an apparent concentration increase of R is sensed by the

tip expressed in the increase of the steady state current. This effect is referred as *positive feedback* and the current changes according to Eq (3).

$$\frac{i}{i_\infty} = 0.68 + 0.78377\frac{a}{d} + 0.3315\exp\left(-1.0672\frac{a}{d}\right) \quad (3)$$

The applied mediators can be any reversible redox species that does not react with the electrolyte and the sample. A few examples are: ferrocene-methanol [5], $[Fe(CN)_6]^{4-}$ [6], $[Ru(NH_3)_6]^{3-}$ [7], I^- [8].

The feedback effect is a pivotal phenomenon in SECM that can be exploited to determine the tip-substrate distance and surface topology can be imaged. In **Fig 3**, the negative and positive feedback responses are demonstrated.

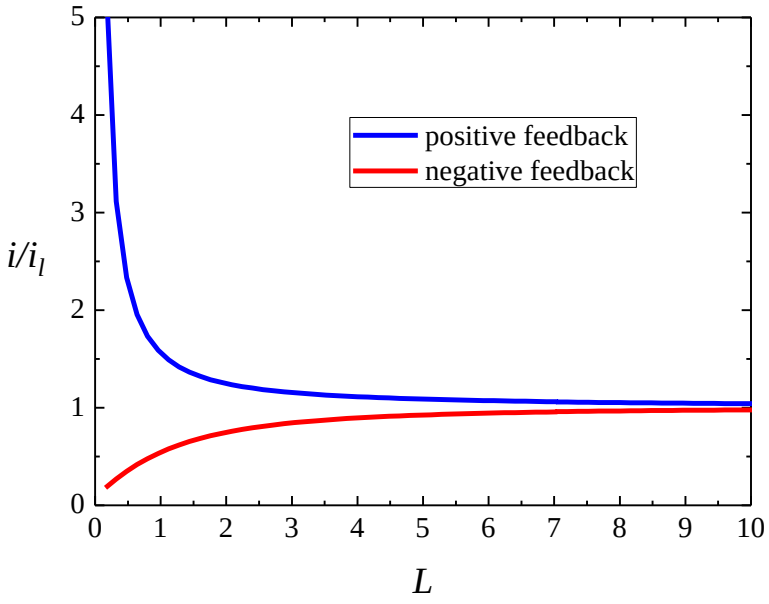

Fig 3. The change of the voltammetric current with respect to the tip-sample distance. The positive feedback effect occurs if the substrate is a conductive surface; the negative feedback occurs when the tip approaches an insulating surface.

I.1.3. Generator/collector modes

In many situations, for instance, where the mediator signal is perturbed, the generator collector mode can be applied. The potential of the collector is usually kept at a potential where the species producFed on the generator can be electrochemically reduced or oxidized.

In tip generation substrate collection mode (TG-SC), the tip is used to produce *O* that reacts on the surface of the sample as it is depicted in Fig 2D. Since *O* reacts on the surface, the positive feedback loop can be avoided. In theory, the substrate current should be zero, when the tip is not operating, however, unfortunately a large backgound current is measured.

Hence, if TG-SC mode comes up as the tool of the investigation, usually the substrate size is minimized as possible. Then the faradaic current measured during the experiment should be corrected by subtracting the background current when no generation occurs at the tip.

This method was used to release chloride ions in the proximity of a stainless steel sample, in order to investigate pitting corrosion [9].

A more widely spread method is the substrate generation tip collection (SG-TC) mode, where the tip is used as a detector to map the reaction product generated by the substrate. In corrosion research this is of practical importance, since the dissolving ions produced in the anodic half cell reaction can be detected by the tip and the local concentration is reflects on the local corrosion activity. In the literature there are a series of cations and neutral species that could be measured amperometrically. Corrosion processes producing Fe^{2+} [10], Ni^{2+} [11], Cu^{2+} [12], Cr^{2+} [13], Ti^{3+} [14] could be measured in aqueous media whereas Zn^{2+} in organic medium [15] was detected. The drawback of this method is that some metals, Mg for instance, have the reduction potential outside of the potential window of the solvent. On the other hand, the amperometric detection suffers from poor selectivity, that can be overcome by applying ion selective microelectrodes in potentiometric mode.

I.1.3. Redox competition mode

The redox competition mode of the SECM is a rather new variant of operation introduced by Schumann and coworkers [16]. In the case of the simplest approach, both the substrate and the tip is polarized at the same potential, consequently the probe and the sample will compete for the redox species in the solution. As a matter of fact, the sample does not have to be polarized if the reaction extorted on the probe takes place spontaneously on the sample. In the bulk the hemispherical diffusion provides a well defined mass transport flow towards the probe surface, and as the tip travels above the embedding resin at a constant height the residual current limited by the feedback effect remains constant. However the local concentration of the mediator decreases due to the reaction taking place on the sample surface, hence a current decrease is expected above those areas where the consumption of the mediator occurs. Sometimes the reaction at the surface is unexpected and attributing the current change solely to the feedback effect in approach curves can be a flaw. Hence it is advisable to perform constant height measurement to ensure that the choice of mediator is appropriate for the investigation of the system with the approach curves in feedback mode.

I. 1.4. Potentiometric mode

Although potentiometric SECM is not much younger than the amperometric one, the amperometric operation highly outnumbers the potentiometric SECM measurements, which is less than 1 % of all experiments. Even so, the use of potentiometric probes provides the possibility of detection of species having their redox potential beyond the solvent window (i.e. alkali and alkaline earth metals in aqueous solutions).

The first potentiometric SECM measurements were carried out by using solely metal microelectrodes (Ag, Sb) [17]. Horrocks et al. prepared dual functioning antimony

microelectrodes operating in both amperometric and potentiometric mode. The antimony microelectrode belongs to the family of the so-called metal/metal oxide electrodes that are known to be pH sensitive. Antimony has a very narrow potential window where it is stable. Although this makes it useless in a series of conventional voltammetric applications, the SECM requirements are different. To wit, this narrow potential window happens to cover the oxygen reduction potential, therefore in SECM measurements it can be used for O_2 detection in amperometric mode. This is very advantageous, because the major "flaw" of the passive, potentiometric operation is that it does not allow precise probe positioning. Therefore the desired tip-sample distance can be established using the amperometric *Z* approach curves employing the dissolved oxygen as mediator, and then localized pH measurements can be performed in potentiometric mode [17]. Although oxygen is not a reversible redox mediator, the negative feedback effect can occur above insulating surfaces. It has to be noticed that when it comes to corroding surfaces, where the cathodic reaction is often the reduction of oxygen, the mixed negative feedback effect and redox competition occurs, hence the *Z* approach curve has to be recorded above the resin. With the metal electrodes, only a very limited set of ionic species (i.e., H^+ and Ag^+, Cl^-) can be detected. As a step forward, the use of micropipette type ion-selective microelectrodes has successfully overcome the main drawback of the amperometric SG-TC, TG-SC modes, namely the poor selectivity. Nevertheless, ISME's have their disadvantages in difficult probe positioning, short lifetime, fragility. The problem of probe positioning could be resolved using double-barreled tips containing gallium microelectrodes [18], yet it hasn't come into general use. One of the main focus of this dissertation is the application of ion selective microelectrodes in SECM, hence their operation will be demonstrated in Section I.3. in more details.

I.2. Electric field measurements with the Scanning Vibrating Electrode Technique (SVET)

Although the dissertation mainly focuses on my work with Scanning Electrochemical Microscopy, Chapter 3 and 4 in Part III contains some measurements using the Scanning Vibrating Electrode Technique (SVET), hence a brief introduction to SVET can be found here. Besides, the theory behind the technique may help understanding the problems that will be later described in Chapter 2 in Part III.

As a matter of fact, as many tools of corrosionists, SVET was first introduced in biological research and applied for years solely for electrophysiological studies [19,20]. Nowadays, the most significant use of this technique is the investigation of corrosion processes following the pioneering work of H. Isaacs reported in the 70's [21].

Aqueous corrosion involves the anodic oxidation of the metal and the cathodic reduction of a species from the solution. The flow of electrons within the metallic phase does not cause ohmic potential variation because of the high conductivity of the metal. On the other hand, the current in the aqueous phase is carried by ions and will produce potential differences between the anodic and the cathodic areas. The Laplace equation shows the distribution of potential:

$$\nabla^2 \varphi = 0, \tag{4}$$

where ∇^2 is the Laplace operator, φ is the potential. Taking the gradient of the potential, we will get the electric field (E).

In their recent review article, Bastos et al. use the following example to explain localized current measurements [22]. Let's consider two electrodes facing each other in 4 cm distance. Their surface is 1.5-1.5 cm^2 and 100 μA is flowing and therefore, the current density is 66.6 μA cm^{-2}.

A reference electrode was moved between the two electrodes to measure the ohmic drop against another reference electrode kept in a fixed position. The potential difference ($\Delta\varphi$) measured in Δr distance will give the electric field (E) in the solution (with specific conductivity of κ), and the current density can be calculated using the following equation:

$$i = \kappa \cdot E = -\kappa \cdot \frac{\Delta\varphi}{\Delta r} \tag{5}$$

This is a simple example of the Scanning Reference Electrode Technique (SRET) which has been used a long time ago [23], but since this technique is susceptible to noise, SVET became widespread instead. The sensing probe of SVET is a single microwire of PtIr alloy that vibrates at small amplitude owing to the piezoelectric benders driven by sine wave oscillators at two different, optimized frequencies, one for each orthogonal axis of vibration. At the extremes of the vibration the potential of the pseudo-reference electrode is measured that results in a sinusoidal signal modulation. This is measured using a lock-in amplifier that enhances the signal-to-noise ratio significantly. The relationship between the measured

potential difference and the current density is determined by calibration using a current point source that drives known current. Then a proportionality factor is calculated by the software and used during the real measurements. It has to be mentioned that if the conductivity of the electrolyte changes, the calculated current densities may differ from the actual ones.

A schematic drawing of the measurement cell is shown in **Fig 4**. The vibrating electrode (1) is attached to a plastic cantilever and connected to two piezoelectric vibrators for the two orthogonal vibrations. A platinized platinum wire is used as reference electrode (2) and another wire is the ground (3). The samples (4) are, similarly to the SECM experiments, embedded in epoxy resin and the solution reservoir is made by wrapping adhesive tape around the epoxy mount.

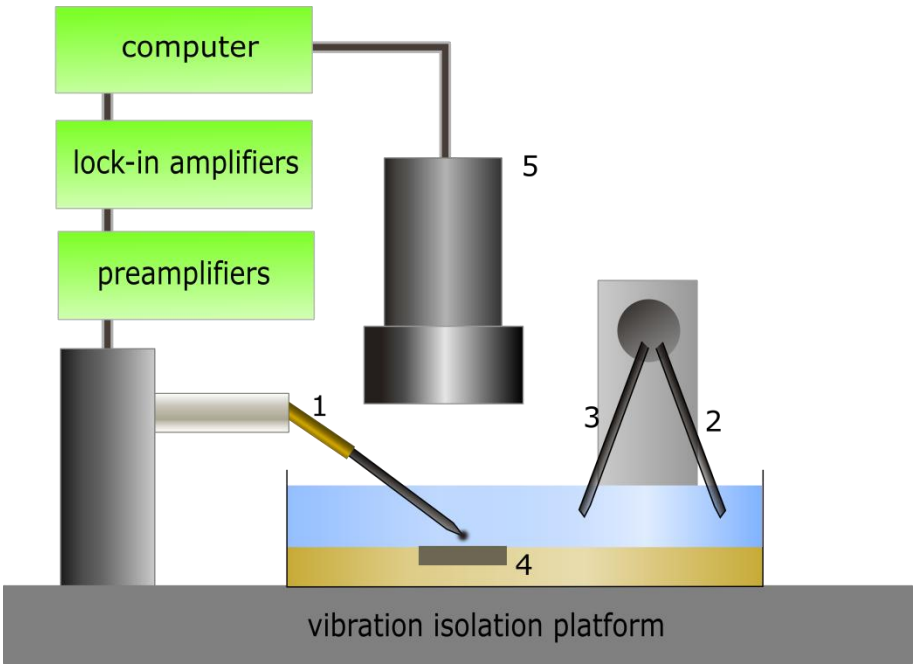

Fig 4. Schematic drawing of the SVET equipment. 1: vibrating probe connected to piezo controllers; 2, 3: platinum reference electrodes attached to a stagnant stage; 4: the sample of interest immersed in the test electrolyte; 5: microscope camera.

In corrosion research, SVET maps are often presented with the corresponding photographs of the sample. The optical pictures show the accumulated corrosion, whereas the SVET map shows the actual active sites on the surface at the moment the photograph was taken. This is very similar to the SECM studies; nevertheless, SVET measurements show the cathodic and anodic areas at the same time. In SECM, only localized pH measurement can reveal these areas simultaneously, although in lower resolution, since the local acidification accompanying the anodic half-cell reactions comes with small pH changes, as opposed to the cathodic half-cell reactions that cause greater pH changes in the adjacent solution of the

sample. On the other hand, SVET does not provide the identification of the sensed species, hence it is often used in combination with SECM [24-27].

As opposed to the example described above, the cathodic and anodic sides are often side by side on corroding surfaces. Hence, usually the vertical (*Z*) component of the current density is presented, showing the ionic fluxes perpendicular to the surface.

Current density is a vectorial parameter. Following the convention, positive current is the flux toward the solution from the anodic sides, and the negative current is the flux toward the sample surface. That is, the release of positively charged cations from the surface results in positive current density, whereas the electrons will be captured in reduction processes taking place on the cathodic sites which current density is accepted with negative sign. When it comes to the current densities measured by the tip vibrating in two orthogonal axis (*Z* and *X*), the situation is somewhat more complicated than the above mentioned sign convention.

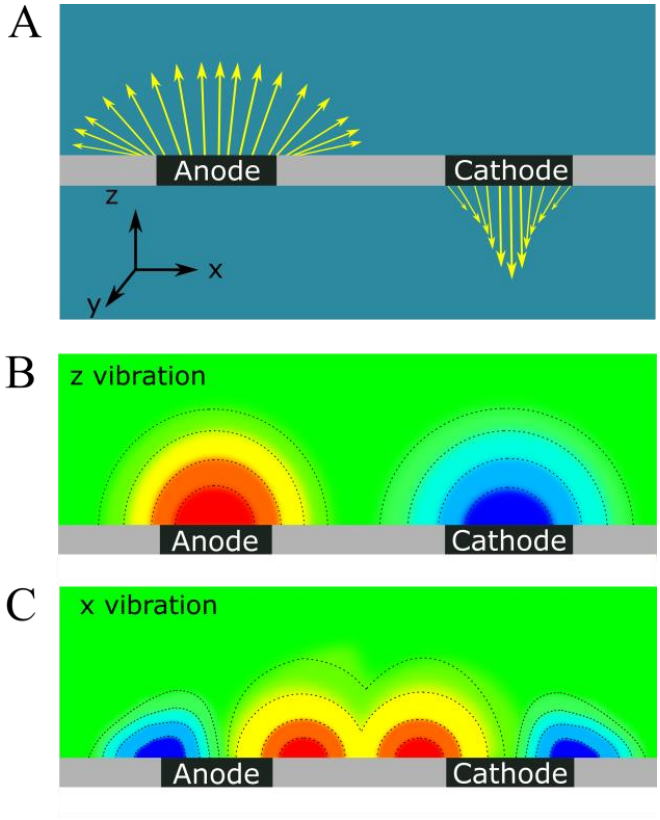

Fig 5. Illustration of the current and potential line distributions above a galvanic pair. **A** shows the sample and some ionic current vectors as the anode and the cathode are coupled. **B** illustrates the expected ionic current distribution measured by the SVET in the case of the *Z* vibration. Red and blue colors belong to the highest anodic and cathodic current densities andlocated where the current density vector is parallel to the vibration. **C** represents the vibration axis parallel to the sample, where the maxima and minima in the signal are collected when the current density vectors parallel to the sample, namely at the edges.

Fig 5A shows a corroding sample with an anode-cathode pair well separated from each other. The yellow arrows imply the current density vectors. In the case of the *Z* vibration, the arrows are in the positive *Z* direction on the anode and in the negative direction on the cathode. In **Fig 5B** the local current densities are „plotted". The green color represents zero current, which is in the bulk of the solution, far from the active sites. Red color indicates positive current densities and blue color shows negative current densities. On the other hand, in the case of the horizontal vibration on the *X* axis, namely, parallel to the sample surface, the centers of the anode and the cathode drive zero current (the current density vectors are perpendicular to the *X* axis). The vectors pointing to the right side will appear as red spots in the maps, whereas the vectors pointing to the left side are represented as negative currents. The dashed lines in **Fig 5B** and **5C** resemble the equipotential lines (**A**) and the current density lines (**B**).

Although SVET utilizes the electric field arising in the corrosion process to estimate the ionic currents, in potentiometric SECM measurements, the electric field affects the measured signal. The resolution for this problem will be discussed in Chapter 2 within the Results and discussion part.

I.3. Ion selective electrodes (ISE)

I.3.1. Brief history of ISE development

The first ion selective electrode was the glass electrode – the „best" chemical sensor ever since, as it is the only sensor possessing 12 orders of magnitude linearity range [28]. The first approach of the solid state membrane electrode was done by Tümpler in 1921 [29]. Kolthoff and Sanders made a disk shape membrane of molten silver chloride [30]. However, Hungarian researchers proudly count the start of the history of the ion selective electrodes from the report of the silver iodide based iodide selective crystalline membrane electrodes, invented by Ernő Pungor [31]. Indeed, the theoretical foundations of the ISE's were laid down in the following year [32], and the appearance of the ion exchanger ISE's led to an enormous development in the field [33]. Apart from the membrane based ion-selective electrodes, the solid state ISE's are another populous group. The famous fluoride selective electrode – the only device that can measure fluoride ion activity up to now– utilizes the dislocations of the lanthanum fluoride crystal doped with europium ions where the fluoride ions can selectively fit [34]. In parallel to the development of the ion selective electrodes, the miniaturization of the glass type electrodes was also started by life scientists, who were interested in local activity measurements in living cells [35]. Liquid membrane based ion-selective microelectrodes are used since 1971 [36]. The thin organic liquid membrane plugged in the tip separates the internal filling solution from the analyte solution. The micropipette glass, however, is hydrophilic, hence the internal solution can leak along the glass wall and the sample solution can crawl slowly. As the two aqueous solutions "find the way" to each other, the ISME ceases functioning. To avoid this, surface pretreatment is used to apply to hydrophobize the inner glass surface of the tip.

In the next years, the further decrease of tip size led to the development of double-barrel electrodes [37]. In this case, the silanization has to be applied solely on the ISME barrel while the reference barrel has to be left hydrophilic. Since the regular silanization is done by exposing the micropipettes to the saturated vapor of the silanazing agent, this can be challenging. Nevertheless, nitrogen overpressure applied on the reference barrel during the silanization can solve the problem.

Gyurcsányi et al. introduced the solid contact potassium selective microelectrode. It consists of an 8 μm diameter carbon fiber sealed in the micropipette [38]. The polished the tip results in a carbon disc microelectrode. It is coated then with conductive polymer and the ion selective cocktail. The all solid state arrangement advantageously decreases the resistance of the ion-selective microelectrodes.

I.3.2. The theory of the ionophore based ion selective electrode response

Ion selective electrodes are potentiometric devices, consisting of a selective transducer transferring ion activity of ideally a single species in the solution to electric potential. The most famous ion selective electrode is the pH sensitive glass electrode, although, by applying membranes with different permselectivity, a great number of other ionic species can be detected [39-42]. Regardless the type of the membrane, the same fundamental, thermodynamic equations apply. As the first approach, an ion selective electrode containing measuring cell can be described by the following cell diagram in **Fig 6**:

reference electrode || sample solution a_i | ion selective membrane| $a_{i,ref}$, a_{Cl^-}, AgCl(s) |Ag

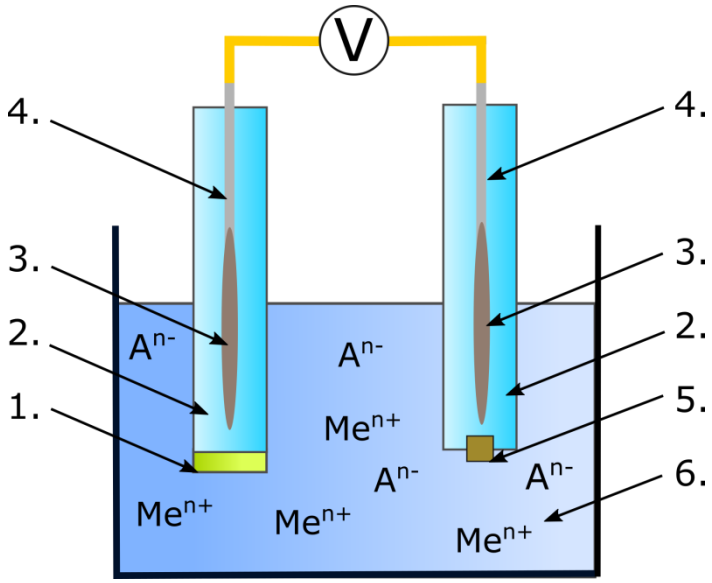

Fig 6. Sketch of the potentiometric cell containing the ion selective electrode. 1: ion selective membrane; 2: inner filling solution; 3: AgCl; 4: silver wire; 5: porous plug; 6: sample solution.

The potential of the ion selective electrode is measured against the reference electrode and contains two components: (1) the potential of the internal reference electrode and (2) the membrane potential. The latter is governed by the activity difference of the analyte ion in the sample and in the internal solution of the ISE:

$$E = E^0 + \frac{2.303RT}{z_i F} log \frac{a_{i,sample}}{a_{i,ref}} \tag{6}$$

In fact, the measured potential comprises also the diffusion potential, defined as:

$$\Delta\varphi_{diff} = -\frac{RT}{zF} \frac{\sum(u_i/z_i)(c_{i2} - c_{i1})}{\sum u_i\,(c_{i2} - c_{i1})} ln \frac{\sum c_{i2}u_i}{\sum c_{i1}u_i} \tag{7}$$

which contribution can be neglected, if large quantities of electrolyte are added that does not take part in the electrode reaction, and the mobility of the anions and cations are equal.

I.3.2. Role of the membrane components

The organic membrane / aqueous sample phase boundary plays a very important role in the potentiometric response. As it can be seen in **Fig 7**, the ionophore captures the ion of interest (in the example, potassium ion) and balanced distributions are formed in the bulk of the organic and the aqueous phase. Only a few nm thick portion of the phase boundary will differ (marked with dotted rectangle), where the charge separation takes place. There will be a small excess of the anions in the aqueous phase, whereas a small fraction of the cations in the organic phase are complexed by the hydrophobic ionophore. This charge separation will contribute to the formation of the phase boundary potential. Also, a lipophilic anion is usually added to the ion selective membrane, in many cases a tetraphenyl-borate derivative, and it is often referred as ion excluders or anionic sites. This hydrophobic anion prevent the extraction of the anions in the sample to the organic phase. Its concentration has to be kept low, because high concentration of the ion excluder causes high concentration of the cation of interest in the membrane and if there is no free ionophore, the membrane loses its selectivity towards the cation of interest.

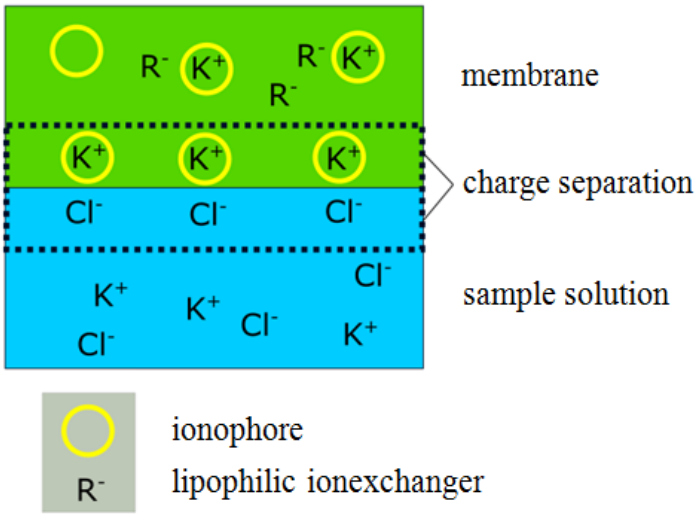

Fig 7. Scheme of the partition of the analyte cation between the sample solution and the ion selective membrane.

The mechanical properties and the resistance of the membrane are enhanced by adding a polymer component, usually PVC. The glass transition temperature of the polymer is lowered by plasticizers.

I.3.3. The phase boundary model (PBM)

The historically first model on the ion selective electrode response, the phase boundary model, was based on the observation that the uneven distribution of charge carrier species in liquid-liquid interface will result in a potential difference. The model states that the membrane potential comprises three terms: the two phase boundary potentials at the inner and outer surface of the membrane, and the diffusion potential within the membrane. However, the diffusion potential was shown to be negligible [43]. The boundary potential difference was named after Donnan, who modeled this phenomenon considering the electrolytes separated by a membrane that allows only one ionic species to pass through [44]. The PBM assumes electroneutrality in the membrane except the boundary and total equilibrium. The electrochemical potential arisen from the charge separation compensates the differences between the chemical potentials. Besides these assumptions, fast ion transport, ideal selectivity, ideal immiscibility, and the availability of the individual ion activity instead of the mean activity was presumed. Then, the electrical potential of the phase boundary was formulated as:

$$\varphi_{PB} = \frac{RT}{z_i F} lnk_i + \frac{RT}{z_i F} ln\left(\frac{c_i^M}{c_i^S}\right) \tag{8}$$

where c_i^M and c_i^S are the concentrations of the ith component with z_i charge in the membrane and the solution respectively, and *R*, *T*, *F* have their usual meaning. The ion partition constant can be defined using the chemical potentials:

$$k_i = \exp\left(\frac{\mu_i^{\ominus(S)} - \mu_i^{\ominus(M)}}{RT}\right) \tag{9}$$

Nikolsky was the first who applied the PBM to the glass electrode, modeling the glass membrane permeable to H^+ ions and not to Na^+ ions. The general form of the well-known formula is:

$$\varphi_{PB} = const. + \frac{RT}{z_i F} ln\left(c_i^S + K_{IJ} c_j^S\right) \tag{10}$$

where K_{IJ} is the equilibrium constant for the ion exchange reaction (with rate constants k_1 of the forward reaction, and k_2 of the backward reaction):

$$K_{IJ} = \frac{k_1}{k_2} = \frac{c_i^S c_j^M}{c_i^M c_j^S} \tag{11}$$

It has to be mentioned that the equations above do not take the diffusion potential (φ_D) into account. Eisenman modified the expression using the mobilities (u_1 and u_2) and the diffusion coefficients (D_1 and D_2) of the ions [45]:

$$\varphi_{PB} + \varphi_D = const + \frac{RT}{z_i F} ln\left(c_i^S + \frac{u_j}{u_i} K_{IJ} c_j^S\right) = const + \frac{RT}{z_i F} ln\left(c_i^S + \frac{D_j}{D_i} K_{IJ} c_j^S\right) \quad (12)$$

The IUPAC recommended form contains the limit of detection (LOD) and the semi-empirical selectivity coefficient (K_{IJ}^{POT}):

$$\varphi_{membrane} = const + \frac{RT}{z_i F} ln\left(c_i^S + K_{IJ}^{POT}\left(c_j^S\right)^{z_i/z_j} + LOD\right) \quad (13)$$

I.3.4. The diffusion layer model (DLM)

The phase boundary model neglects the fact that an electric potential can be generated in the membrane because of the different diffusion rates of the ionic species. Taking into consideration the transport in the membrane, Lewenstam set up the diffusion layer model in his PhD thesis in 1977 [46]. The model deals with the spatial change of the concentrations in the membrane and neglects the temporal changes. Besides, the surface concentration was assumed to be equal to the bulk concentration. The time-dependent response can be modeled by applying the so-called surface coverage factor (*s*(*t*)) that is defined as follows:

$$s(t) = \frac{c_{j0}^M(t)}{c_{i0}^M(t) + c_{j0}^M(t)} = \frac{K_{IJ} c_{j0}^S(t)}{c_{i0}^S(t) + c_{j0}^S(t)} \quad (14)$$

where the superscripts *M* and *S* indicate the membrane/solution interface, and the bulk of the solution, respectively. All the concentrations above are valid for the same time *t*. In the equilibrium, when *t* approaches infinite, the surface coverage factor is expressed as:

$$s(t \to \infty) = \frac{c_{j0}^M(t \to \infty)}{c_{i0}^M(t \to \infty) + c_{j0}^M(t \to \infty)} = \frac{K_{IJ} c_j^S}{c_i^S + c_j^S} \quad (15)$$

The model assumes linear concentration changes within the Nernst diffusion layer (*d*). The fluxes of *i* and *j* in the interface can be given:

$$J_J = -J_I = D_j^S \frac{c_j^S - c_{jo}^S(t)}{d} = D_i^S \frac{c_i^S - c_{io}^S(t)}{d} \quad (16)$$

It is noteworthy that the diffusion coefficients are different in the membrane and in the solution. Hence similarly to the concentrations, the superscripts *M* and *S* mean the membrane and the solution phases. Eventually, we will get the equation for the membrane potential, by combining Eq (14) (15) and (16):

$$\varphi_{membrane} = const + \frac{RT}{z_i F} ln\left\{\frac{[1 - s(t)]K_{IJ} + s(t)\frac{D_j^M}{D_i^M} K_{IJ}}{[1 - s(t)]K_{IJ} + s(t)\frac{D_j^S}{D_i^S}} \cdot \frac{c_i^S + \frac{D_j^S}{D_i^S} c_j^S}{c_i^M}\right\} \quad (17)$$

The most important „lesson" in this model, is the time dependency of the selectivity coefficient. For most analytical purposes, it is not a pivotal factor, since the time required for the measurements (e.g. waiting for the stable value) is sufficient to reach the equilibrium. However, in SECM measurements, when the local measurements are done in rapid succession, it can become influential.

According to the DLM, the selectivity coefficient varies between two limiting values:

$$K_{IJ}^{POT}(t \to 0) = \frac{D_j^S}{D_i^S} \approx 0 \tag{18}$$

$$K_{IJ}^{POT}(t \to \infty) = \frac{D_j^M}{D_i^M} K_{IJ} \tag{19}$$

All in all, the DLM provides a better insight into the potentiometric response of the ISE. However, Eq (17) is a complex expression, especially considering that the total number of the sites on the membrane, hence the electrode potential, cannot be calculated directly. Several further developments have been done using the basic DLM to improve the characterization of the sensor response [47-49].

I.3.5. The Nernst-Planck-Poisson Model (NPP)

It can be easily admitted that the aforementioned models can lead to biased results because they did not consider migration. The ionic species are charge carriers, hence their motion is definitely affected by the outer electric field and they can also generate it. For these reasons, as the computation techniques developed, it was reasonable to consider migration as a possible contributor to the flux, using the Nernst-Planck equation only for one axis (x):

$$J_i^j(x,t) = -D_i^j \frac{\partial c_i^j}{\partial x}(x,t) - \frac{z_i F}{RT} D_i^j \left(c_i^j \boldsymbol{E}^j\right)(x,t) + c_i^j v^j(x,t) \tag{20}$$

where the three terms are diffusion, migration and convection, respectively. $\boldsymbol{E}$ is the electric field that generates migration, v^j velocity of the stream caused by the convection. The electric field is the change of the electric potential with the distance ($\partial\varphi/\partial x$). For the NPP model, the Poisson equation is also used:

$$-\frac{\partial^2 \varphi(x,t)}{\partial x^2} = \frac{F}{\varepsilon_j} \sum_i z_i \, c_i^j(x,t) \tag{21}$$

The total current equation is:

$$I(t) = F \sum_{i=1}^{r} z_i J_i^j(x,t) + \varepsilon_j \frac{\partial \boldsymbol{E}^j(x,t)}{\partial t} \tag{22}$$

The NPP model works with fewer assumptions and simplifying conditions, than the previous two models. It assumes the independence of the dielectric permittivity and the diffusion coefficient from the concentration. The geometry is limited to one dimension and only ideal solutions are considered.

I.3.6. Practical potentiometric measurements

The electromotive force E_{MF} we measure accounts for two different features: the first is the various phase boundary potentials in the cell, and the second is the Ohmic drop. The Ohmic drop is the potential difference between two ends of an ionic conductor characterized by the resistance R of the layer and the current i that flows. However, iR is usually negligibly small, because the measurements are performed under no current circumstances. Taking **Fig 6** as an example, the phase boundary potentials can be illustrated as follows:

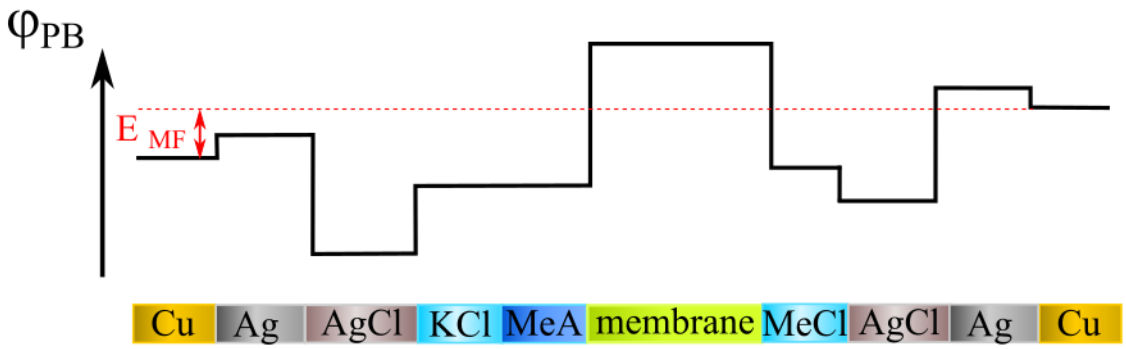

Fig 8. Phase boundary potentials in the potentiometric cell depicted in **Fig 6**, when no diffusion potential is assumed. MeA is the analyte containing Me^+ and A^- anions, whereas MeCl is the dissolved chloride salt of the cation of interest, the internal solution of the ISE.

There were approaches to coat the electric wire contact with the ion selective membrane, however the membrane/metal interface does not have a well-defined phase boundary potential [50]. In the 90‘s a great step forward occurred when conducting polymers were applied as the interface between the membrane and the metal [51].

I.3.7. Factors affecting the potentiometric response versus time measurements

When it comes to the experimental investigation of the dynamic response of the ISE’s, usually the methods involve a perturbation signal intended to bring the system out of the equilibrium, then the relaxing transient signal is studied. The perturbion signal is usually a small amplitude voltage change, or a sudden jump in the activity of the sample solution. However, the dynamic response is often affected by the experimental circumstances and no quantitative information can be obtained from them. The first problem is that in the reality, the sudden activity jump in the solution is hardly a stair-like function at the sensor surface, but it has a finite slope. The time-dependent Nernst equation is used to express the activity-based transient signal:

$$E(t) = E^0 + \frac{RT}{zF}\ln\left(\frac{a_t}{a_0}\right) \quad (23)$$

where a_t is the time dependent activity at the sensing surface, and a_0 is the initial activity from which the jump was undertaken. The activity at the membrane surface can be given as follows:

$$a_t = a_0 + (a_\infty - a_0) \cdot f(t) \quad (24)$$

where a_∞ is the final activity and *f(t)* is a time dependent function [52].

On the other hand, the electric circuit also affects the transient recorded with the potentiometric measuring apparatus containing ion selective electrode. In the case of silicon rubber based ISE's, the response curves were more sluggish than those of the PVC based membrane electrodes. Changing the rate of the activity step had no effect on the transient curve, thus meaning that there was another contribution which can be regarded as the determining factor in silicon based membrane electrodes. In fact, the higher resistance due to the silicon rubber based membrane played a crucial role in those experiments [52]. The potentiometric cell can be modeled with an RC circuit, where the ISE has *R* resistance and the measuring device has *C* capacitance. Then the potential change to an ideal activity perturbation at a certain *t* time is:

$$E_t = E_0 + (E_\infty - E_0)e^{-t/RC} \quad (25)$$

In Eq (25) E_0 and E_∞ are the potentials before and after the perturbation is in equilibrium. It can be concluded that the bigger RC is, the response gets slower. It must be mentioned however that the unrealistic high response time values reported before were due to an inappropriate activity step procedure. This is why a Zn ISME with 4.6 s [53] and a Mg ISME with 2.9 s [54] of total response time could not apparently be applied in SECM measurements without making the scanning time too long or using data treatment [55].

I.3.8. Application of ion selective microelectrodes in corrosion research

The anodic dissolution of corroding metals is accompanied by the formation of dissolved metal cations that can undergo hydrolysis producing H^+ ions in the close proximity of the location of the dissolution:

$$Me \rightarrow Me^{n+}_{(aq)} + ne^- \quad (26)$$

$$Me^{n+}_{(aq)} + H_2O \rightarrow Me(OH)^{(n-1)+}_{(aq)} + H^+_{(aq)} \quad (27)$$

The rate of hydrolysis depends on the stability of the hydroxo-complex that is characterized by its K_{st} stability constant and K_{hyd} hydrolysis constant.

$$Me^{n+}_{(aq)} + OH^- \rightarrow Me(OH)^{(n-1)+}_{(aq)} \quad (28)$$

$$K_{hyd} = \frac{[Me(OH)^{(n-1)+}][H^+]}{[Me^{n+}]} \cdot \frac{[OH^-]}{[OH^-]} = K_w \cdot K_{st} \quad (29)$$

where K_w is the water ion product. The expected local acidification caused by the hydrolysis can be expressed from:

$$pH = -log\sqrt{K_{hyd} \cdot [Me^{n+}]} \quad (30)$$

Local metal dissolution accompanied by hydrolysis can be detected using pH sensitive liquid membrane microelectrodes [56] or metal/metal oxide type microelectrodes, such as the antimony microelectrode [57], as SECM probes.

Alternately, metal dissolution can be followed by measuring the concentration of the metal ions in the proximity of the metal surface. Although this method was merely used to Zn and Mg corrosion research [58,25].

I.3.9. Multi-barrel microelectrodes in life sciences

Multi-barrel micropipettes were developed in the early eighties to monitor simultaneously different ion levels in clinical research, and they are employed in iontophoresis as well [59-62]. In some cases, they are effectively single ion selective electrodes whereas the other barrels are employed to deliver chemicals via iontophoresis [63]. These devices are built placing the electrode in the inner core surrounded by the other capillaries. Alternately, McCarthy et al. employed titanium-based multi-channel electrodes for recording neural signals [64], whereas Piironen and co-workers developed carbon microtetrodes for neuroanalytical applications [65]. As the neurons vary in size and morphology, this electrode assembly with multiple recording sites was a powerful tool for the detection of extracellular voltage signals. On the other hand, Walker et al. fabricated and applied triple-barrel electrodes, including a reference electrode, to measure K^+ ions and pH in barley root cells [66].

I.3.10. Multi-barrel electrodes in SECM studies

Potentiometric microsensors are also often employed in SECM [67,68,57]. In this case, the sensing probe is an ion selective microelectrode (ISME), and its potential is measured against a reference electrode using an operational amplifier-based voltage follower. For Mg^{2+} measurements, many different ionophores have been developed, thus the supreme advantage of the potentiometric SECM is the possibility of direct measurement of Mg^{2+} distributions [69,70]. Likewise in amperometric mode, potentiometric SECM also faces challenges, but some of them could be successfully overcome. The use of solid contacts reduced the response time of ISME's, which resulted in less distorted images [71].

However, some uncertainties have arisen during the quantitative evaluation of magnesium dissolution above galvanically corroding magnesium [72]. Unexpectedly low

local pH values were measured above defects of Mg-galvanized steel that were justified by metal hydrolysis [73]. Recently, these unrealistically big changes were attributed to the electric field being formed during the galvanic coupling [74]. As the consequence of the electric field associated to galvanic coupling, the measured potentials will be shifted with regards to those from the calibration carried out under unbiased circumstances leadingto exaggerated metal ion activities for the adjacent solution. In this case, e.g. pMg<0 values could be calculated using the calibration curve, which is physically impossible.

In that previous work, besides demonstrating the aforementioned symptoms of electric field biased signals, we proposed a possible solution, namely bringing the measuring and reference electrodes as close to each other as possible reducing the potential difference originating from the different locations of the electrodes in the electric field. This would be feasible using multi-barrel arrangements. These combined sensors are long term used in physiological measurements [75-79] and the effect of neural activity could be successfully eliminated [80]. Recently, we applied multi-barrel electrodes in SECM measurements [81,82], therefore the advantage of applying them in magnesium corrosion utilizing the possibility of the microreference electrode placed only a few micrometers far from the measuring electrode seemed obvious.

Another advantage of the multi-barrel electrode is the possibility of simultaneous monitoring of different species, which can provide deeper insight into localized phenomena. Simultaneous measurements in corrosion science have been attempted, firstly by Karavai et al. [54] followed by others [83,84,85]. However, the unwanted contribution of the electric field could not be eliminated, and local acidification around anodic spots seems to be overestimated in some cases. In these works, single-barrel electrodes were positioned close together employing dual stands. Although, for some purposes it is an elegant and convenient way, the use of multi-barrel electrodes would bring more benefits. Firstly, incorporating multiple pipettes can be done nearly without limits, whereas the size of the individual stages does not allow that. In some applications 9-barreled micropipettes were used for the injection of different chemicals [86]. However, such a multi-channel monitoring in SECM experiments requires dedicated instrumentation. The most important advantage is the possibility of a more precise setting of the tip-sample distance than before. The usual way to position the probe to the desired distance from the specimen is the "gentle approach" method. In these experiments, we follow a step-by-step approach of the tip to the sample surface assisted with a microscope, and as the ISME abuts the surface the desired tip-sample distance can be set in the controller and then the ISME is lifted up. In many cases, however, this procedure leads to the crash of the tip, as they are more fragile than the amperometric probes. But instead of using liquid membrane pH sensitive microelectrodes, one can employ the dual functioning antimony microelectrodes [17], which can be used for amperometric O_2 sensing in addition to potentiometric pH measurements [87]. That is, prior to the actual measurements, recording amperometric *Z* approaching curves can help to establish the proper tip-sample distance without breaking the probe, then the potentiometric mapping can be done as it was proposed in [18]. However, the feedback mode requires the electrode surface to be parallel to the sample surface, which is not the case in the previously published works on multiprobe SECM imaging. Therefore in the author's opinion, the use of such multi-barrel assemblies can be one step forward.

I.4. Fundamentals of magnesium corrosion

As they are the lightest metallic structural materials, widening the industrial application area of magnesium and its alloys is of great importance [88]. Moreover, the biocompatibility of magnesium makes it attractive to apply as biodegradable bone implant. However its rapid trend to corrosion severely limits its use.

Magnesium in its metallic form was first isolated by Sir Humphry Davy in 1808. The first corrosion experiment on magnesium was done by Bussy who described the hydroxyde layer on Mg that protects it in dry air [89]. The first mention of the anomalous hydrogen evolution on anodically polarized magnesium was made by Beetz [90].

The counter-intuitive increase in the rate of hydrogen evolution in Mg subjected to anodic polarization is an important feature to be satisfactorily explained. Unlike the Butler-Volmer theory, which suggests that the rate of the H_2 evolution should decrease exponentially as the applied potential becomes more anodic, a linear increase was observed [91-97]. This "anomalous" behavior is often referred to as the negative difference effect (NDE) [98], and it has been frequently justified by postulating the formation of univalent Mg^+ ions as intermediate of the anodic reaction [91,98,99], followed by the reduction of water to produce hydrogen through a chemical reaction due to the high reactivity of this species [99]. However, the existence of Mg^+ in aqueous environment is not verified, and previous indirect detection by Petty et al. [100] has been systematically refuted by Frankel and coworkers [101]. Moreover, they proposed an alternate explanation of the "anomalous" current density increase – increased H_2 evolution rate - invoking the catalytic character of the metal surface during dissolution [102,103]. Williams et al. demonstrated the existence of local cathodes on the anodically polarized magnesium surface using the scanning vibrating electrode technique (SVET) [94], which combines with reports of increased hydrogen evolution rates in areas of dark corroded magnesium [96,104-106]. Comprehensive reviews covering the various models proposed to justify the NDE have recently been published [107,108].

I.4.1. Magnesium corrosion

As it was mentioned before, the corrosion resistance of magnesium is very low, due to the negative standard electrode potential that also allows magnesium to corrode under anaerobic circumstances. In the case of aqueous corrosion, the surface film consisting of magnesium-oxide and hydroxide provides only minor protection. On air, a few nm thick layer of MgO is formed instantaneously in exothermic reaction resulting in the pyrophoric property of Mg powder. This MgO layer protects Mg effectively from atmospheric corrosion. MgO and $Mg(OH)_2$ are slightly soluble in water, the K_{sp} values are ~10^{-6} and ~10^{-11}, respectively, that implies it is only a quasi-passive layer in aqueous solutions [109]. The dissolution of magnesium takes place on the anodic sites producing two electrons:

$$Mg \rightarrow Mg^{2+} + 2e^- \quad (31)$$

The electrons liberated in the anodic half-cell reaction are consumed in the cathodic half-cell reaction, mainly in the reduction of water producing hydrogen gas on the cathodic sites:

$$2\,H_2O + 2e^- \rightarrow H_2 + 2OH^- \tag{32}$$

The overall corrosion reaction is

$$Mg + 2\,H_2O \rightarrow Mg(OH)_2 + H_2 \tag{33}$$

Pure magnesium exhibits filiform corrosion progression, however the alloys show disc shape dissolution pattern.

I.4.2. Anomalous hydrogen evolution on anodically polarized magnesium

According to Eq (32), the hydrogen evolution reaction is the primary cathodic reaction on non-polarized magnesium. Nevertheless, significant amount of hydrogen is being produced on the surface of anodically polarized magnesium as well. In fact, not only higher dissolution occurs as one increases the anodic overpotential on magnesium, but the rate of the hydrogen evolution reaction (HER) is increased. This observation contradicts what it would be expected based on the Buttler-Volmer equation:

$$i_{HER} = i_{0,H,Mg}\left[exp\left(\frac{\alpha_a zF}{RT}(E - E_{rev,H})\right) - exp\left(-\frac{\alpha_c zF}{RT}\left(E - E_{rev,H}\right)\right)\right] \tag{34}$$

where i_{HER} is the current density of the hydrogen evolution reaction (A/cm^2), $i_{0,H,Mg}$ is the exchange current density, E and $E_{rev,H}$ are the electrode potential and reversible potential for the HER in V, respectively, $\alpha_a$and $\alpha_c$are the anodic and cathodic charge transfer coefficients, the other symbols have their usual meaning. As the consequence of Eq (34), if E is raised, the second exponential term becomes smaller. That is, the rate of the cathodic half cell reaction should decrease exponentially. This counter-intuitive perception is often referred as Negative Difference Effect (NDE) which originates from the following equation:

$$\Delta = V_1 - V_2 \tag{35}$$

where Δ is the so called difference effect, the difference between the hydrogen evolution rate from an electrode at OCP (V_1), and HER from the same electrode when it is polarized (V_2). V_1 and V_2 are usually obtained from volumetric measurements of hydrogen evolution and have a unit of mm^3/cm^2 min. In the early 60's, Straumanis et al. proposed an empirical formula including the total rate of HER (V_T) and a constant [110]:

$$\Delta = V_1 - (V_T - 6.7) \tag{36}$$

From Eq (36) it can be clearly seen, that the higher HER at anodic overpotential will result in a negative value for Δ, hence the name NDE.

The "univalent Mg" theory is based on the assumption that an intermediate of the anodic dissolution, Mg^+, is responsible for the anomalous hydrogen evolution.

$$Mg \rightarrow Mg^+ + e^- \tag{37}$$

$$Mg^+ + H_2O \rightarrow Mg^{2+} + \frac{1}{2}H_2 + OH^- \tag{38}$$

Although it is a relatively old idea, Song and Atrens revivied the univalent Mg theory in the last 10-20 years [111-114]. Unfortunately, Mg^+ could not be detected with the modern analytical tools. If it exists, one can assume a very short lifetime and high reactivity. On the other hand, the original experiment of Petty implies that it has to be relatively stable in the water [100]. Besides, Kirkland et al. showed that the average number of electrons exchanged for Mg dissolution under anodic polarization is very close to 2 [115], disproving the observation of Atrens [114].

In 1961, a new mechanism was proposed by Nagy and coworkers [116]. As opposed to Petty's theory, this model took into account the role of the surface processes, such as adsorption, the oxyde-hydroxyde containing corrosion product layer, and the hydrogen on the surface:

$$Mg + H_2O \rightarrow MgOH_{2\,ads}\ \ (fast) \tag{39}$$

$$MgOH_{2\,ads} + H^+_{ads} \rightarrow MgOH_{\,ads} + H^+_{2\,ads}(fast) \tag{40}$$

$$MgOH_{\,ads} + H^+_{ads} \rightarrow MgOH^+ + \frac{1}{2}H_2(fast) \tag{41}$$

$$2H^+_{2\,ads} \rightarrow H_2 + 2H^+_{ads} \tag{42}$$

Recently, Taylor proposed a modified version of this mechanism [117]. Based on quantumchemical calculations, he proposes that the initial dissociation of water adsorbed on the metal surface is followed by a hydrogen molecule formation on the Mg*H site without any charge transfer reaction, only the recombination of the atomic hydrogen. The remaining Mg*OH will consume two electrons and release two hydroxide ions. Then, the total reaction equation is:

$$2H_2O + 2e^{-\cdot} + \ 4\,Mg^*[\rightarrow 2Mg^*H + 2Mg^*OH + 2e^{-\cdot}] \rightarrow H_2 + 2OH^- + 4\,Mg^* \tag{43}$$

The removal of the hydroxide ions can be done alternatively by the anodic dissolution of magnesium.

It was also supposed by others, that magnesium hydride forms in the anodic dissolution process, a species very unstable in aqueous solution, hence the hydrogen evolution [118].

In 2011, another mechanism for the anomalous HER was proposed [119]. It goes back to the two-step oxidation of Mg and assumes that the bivalent Mg ions go into the electrolyte whereas the electrons remain in the metal phase. The negatively charged metal surface will

then hinder the diffusion of the positively charged Mg^{2+} ions. Eventually, the hydrogen ions in the solution will consume the electrons, while magnesium ions will react with the hydroxide ions in the solution forming $Mg(OH)_2$ precipitate. Under anodic polarization, water self-ionization will be disturbed by the increased amount of Mg^{2+} production (as it consumes the OH^-) that will shift the equilibrium providing more H^+ for the hydrogen evolution. The schematic mechanism is depicted in **Fig 9**. In this model, the role of the monovalent magnesium ion is not clear; probably, it is only a tribute given to Petty's work.

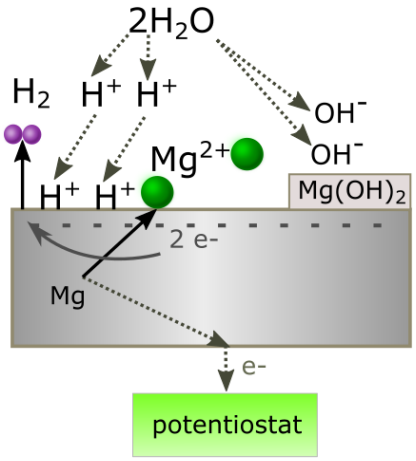

Fig 9. Hypothetic mechanism of the hydrogen evolution and explanation of the NDE

Another weighty theory is based on the catalytic effect of the dark layer of the corrosion products left behind by the filiform progression of magnesium dissolution. The layer consists of a MgO rich inner and a mixed $MgO/Mg(OH)_2$ outer layers. There are several observations confirming the increased HE either on or at the very close proximity of the dark layer covered regions compared to pristine surfaces. Marco and van der Biest used the rotating disc electrode technique to investigate the corrosion of magnesium when the rotation removes the corrosion products from the surface reducing their influence on the degradation of the material [120]. Their findings were in great accordance with the assumptions of the catalytic surface theory.

Birbilis et al. observed that after the application of an increased sequence of anodic current densities to magnesium, followed by polarization of the sample to sufficiently negative potential and measurement of the cathodic current, that the cathodic current increased after increasing anodic polarization [96].

Salleh et al. demonstrated the 4-6 times greater H_2 evolution rate above $Mg(OH)_2$ coated magnesium surface than on untreated surface using SECM [105]. On the other hand, during anodic polarization, the rate of the HER increases by several orders of magnitude, despite only 2-3 times thickening of the dark layer.

The increased rate of hydrogen evolution on the corroded areas is a very straightforward explanation of the NDE: if anodic polarization is applied, the formation of the dark layer is faster, therefore the HER becomes faster. SVET studies seem to confirm this assumption. It has been shown, that the filiform pattern of the corrosion product deposition progression is

coupled with the occurrence of anodically active areas at the front of the filiform track [121]. The cathodic and anodic net current increases in parallel.

Summarizing these findings and assumptions, **Fig 10** shows schemes of the magnesium corrosion at OCP and under anodic polarization.

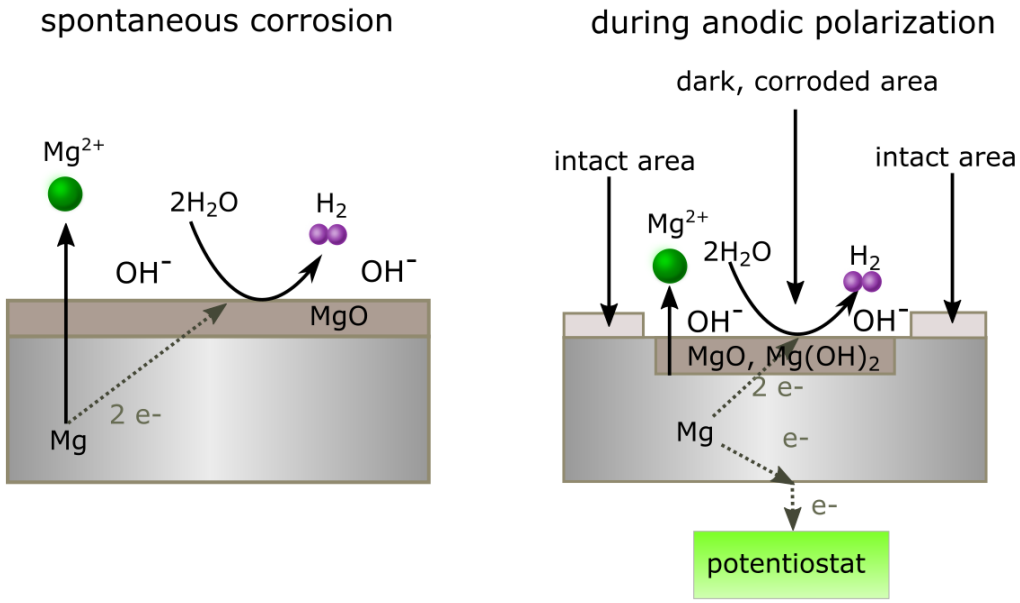

Fig 10. Scheme of the spontaneous magnesium corrosion (left) and the corrosion during anodic polarization (right) according to the enhanced catalytic surface theory.

On the other hand, continuing investigation with the SVET, a particularly interesting phenomenon was observed by Williams et al. [122]. When high concentration NaCl was employed in the experiments, the iron containing magnesium alloy displayed disc-shape corrosion spots as it was expected for alloys, but as they decreased the concentration of the electrolyte, the filiform track appeared on the magnesium surface. They explained this phenomenon by the galvanic coupling between magnesium and iron. In the case of high conductivity, the coupling between the anodic areas and the iron particles is possible, however, at low NaCl concentration the ohmic effect hinders the galvanic coupling, hence the corrosion pattern reminds more the filiform track on the pure Mg.

Another experimental fact that did not meet the expectations of the enhanced catalytic surface theory is that the rate of the HER does not always increase with the layer thickness, but it remains constant or even it is diminished. These findings led to the consideration of the role of the alloying materials. For the most part, the alloying metals are nobler than magnesium, thus they can act as local cathodes on the surface. The noble impurities can accumulate in the dark corrosion layer and even under potentials that are anodic for magnesium the HE can take place at increased rates. The effect of the surface enrichment is depicted in **Fig 11**. The surface enrichment of iron was detected using scanning electron microscopy based energy dispersive spectroscopy (EDS) [123]. Thus it was proposed that as

the corrosion product front proceeds, the nobler iron particles or clusters can come into direct contact with the electrolyte promoting the formation of local cathodes.

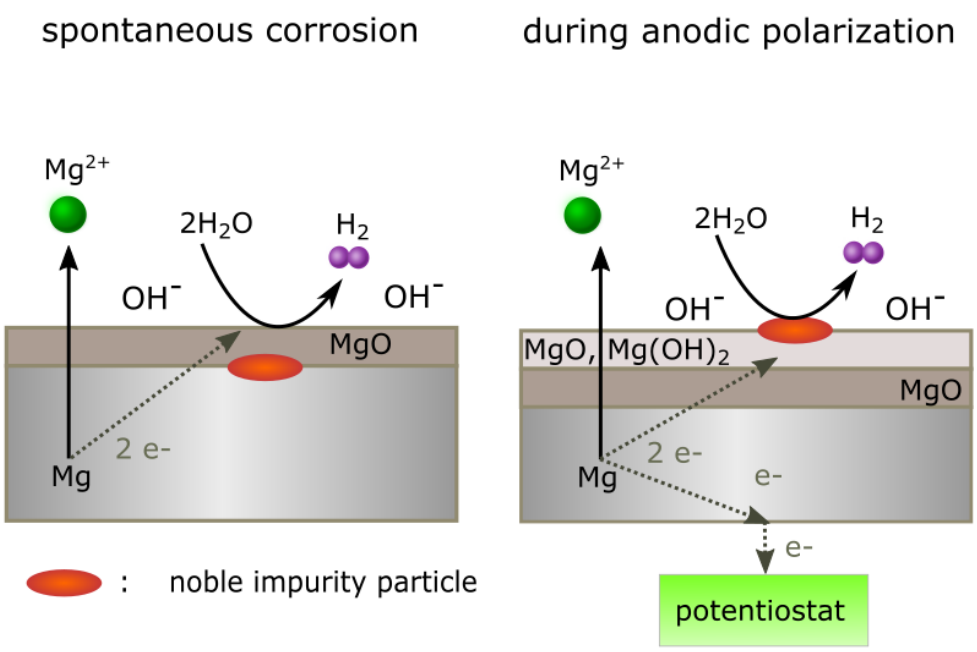

Fig 11. Schematic drawings of the explanation of the NDE invoking the surface enrichment od the noble impurities

Other authors showed that enrichment of iron on the surface of the anodic polarized magnesium is a low efficiency process. A model was proposed by Birbilis and coworkers, where the enrichment efficiency could be expressed with regards to the surface concentration of iron [124]:

$$\text{Fe enrichment efficiency} = \frac{\text{actual [Fe]} - \text{initial [Fe]}}{\text{theoretical[Fe]} - \text{initial [Fe]}} \tag{44}$$

where, the theoretical iron surface concentration is calculated from the charge passed through the sample. The results showed that the enrichment efficiency after 500 s at 10 mA/cm^2 was less than 1%. It has been also shown that the enrichment increases with time (i.e. the above mentioned enrichment efficiency at 10 mA/cm^2, after 200 s was ~0.1%). This raises the similar question as in the ECS theory: why the rate of the HER does not increase in time if the impurity accumulation progresses? Besides, experiments were carried out with ultrapure magnesium to exclude or at least minimize the accumulation of the impurities and the rate of the hydrogen evolution increased with the applied anodic polarization [96]. In those studies showed that the increased hydrogen evolution rate is occurring even under super poor circumstances.

Fajardo et al. carried out gravimetric measurements and found that the volume of the evolved hydrogen does not change accordingly to the cathodic current densities that were measured using SVET [94]. The calculated current densities from the cathodic polarization curves and the integrated SVET measurement fit only after a relatively long time. The total amount of the evolved hydrogen was significantly higher than that was calculated from the

current density contribution of the impurities and the dark film. In their subsequent work, they showed that the anomalous increase of hydrogen evolution is still significant in acidic media where the dark corrosion film is not stable and the effect of the impurities is also negligible because of the ultrahigh purity magnesium [125]. This is a rather interesting finding, because it implies that the hydrogen evolution is independent from the corrosion products, although others reported that a low passivating $Mg(HPO_4)_2$ layer could decrease the hydrogen evolution rate under anodic polarization [126].

Due to the numerous controversial results in the literature, there is an endeavor to separate the source of the total HE into 3 terms [127]:

$$HE_{total}=HE_{anodic}+HE_{film}+HE_{impurities} \quad (14)$$

where HE_{anodic} comprises the hydrogen evolved on the anodically active sites, and the hydrogen evolution occurring on the impurities ($HE_{impurities}$) and the surface film (HE_{film}) is also separated. HE_{anodic} cannot be determined; it can be only calculated by knowing the other terms and the HE_{total}.

After proving and disproving the main role of the impurities, in a recent publication, Birbilis found experimental evidence that surface layer stability is an important factor in the NDE [128].

Zheludkevich and coworkers published an interesting contribution in which they showed that the mechanical removal of the impurities during the anodic dissolution followed by redeposition can be responsible for the local cathodic activities [129]. It is also stated that the dark film becomes active after the full coverage of the surface and the contribution of the impurities diminishes.

The proposed scenario is the following: first the iron particles detach because of the hydrogen bubbling followed by the chemical dissolution of the iron clusters. These dissolved clusters can adsorb hydrogen on their surface and the chemical reduction of the iron(II), iron(III) species can occur. The redeposited metallic iron film enhances the HER due to the increased reactivity of the pure metal. The three pathways of the hydrogen evolution on the iron surface were given as:

$$Fe + H_2O + e^- \rightarrow Fe - H_{ad} + OH^- \quad (45)$$

electrochemical adsorption of hydrogen,

$$2H_{ad} \rightarrow H_2 \quad (46)$$

chemical desorption of hydrogen, and

$$H_{ad} + H_2O + e^- \rightarrow H_2 + OH^- \quad (47)$$

electrochemical desorption of hydrogen.

Eq (45) is referred as the Volmer step, Eq (46) and (47) are the Tafel and Heyrovsky HER, respectively [130]. The three elementary steps will result eventually in Eq (32). Höche

et al. surmises the Heyrovsky route as the favored mechanism [135]. The presumed mechanism for the HER on Mg is depicted in **Fig 12**.

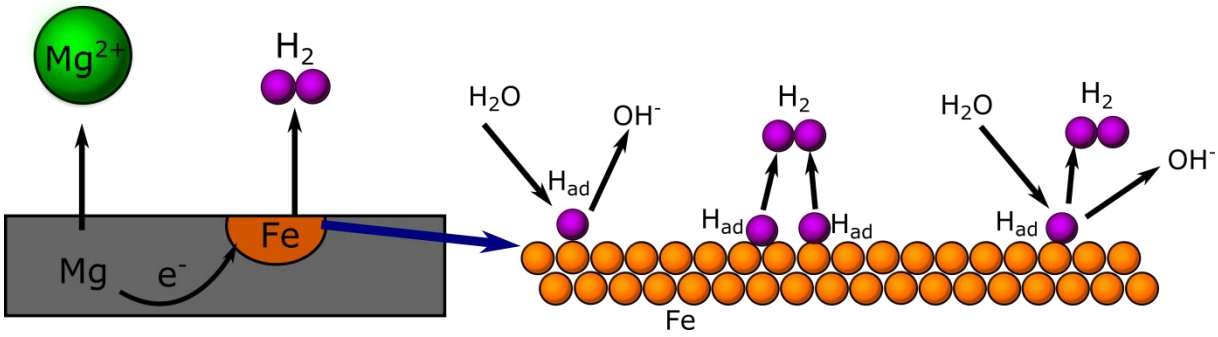

Fig 13. Mechanism of H_2 evolution on anodically polarized magnesium according to [129].

Another controversial fact can be the change of pH that plays a role in the anomalous hydrogen evolution. Even at high pH, the NDE occurs, which contradicts the previous theory, because the releasing ions i.e. Fe^{2+} will precipitate, hence the redeposition mechanism cannot take place [131].

I.4.3. Electrochemical testing of magnesium corrosion

Since corrosion is an electrochemical process, the electrochemical techniques are very popular in corrosion testing. It merits the comment that the HER does not obey the Faraday's law, thus solely using electrochemical methods is not sufficient to assess the amount of the dissolved magnesium. That is, some fraction of the electrons produced under anodic polarization will not pass through the potentiostat but will be consumed by the HER.

In potentiodynamic polarization measurements, the potential of the sample is swept with respect to a reference electrode at a constant scanning rate and the current is measured. The result is usually plotted in overpotential-logarithmic current (or reversed in Europe) diagrams. The current response is determined by the relative rates of anodic and cathodic reactions. In the case of the Mg electrode, the potential increase comes with steep anodic current increase, that is, magnesium is non-polarizable. It merits the comment, that reliable analysis is interfered by the potential drop caused by hydrogen bubble formation. The hydrogen evolution at high anodic potentials cannot be adequately described using the standard electrochemical kinetics of the activation-controlled reactions. Hence, galvanostatic and galvanodynamic polarization is more often used in magnesium research [132,133]. The galvanostatic test allows charge control. It facilitates comparison of hydrogen evolution rates when different current densities pass through the sample. Birbilis et. al carried out a series of experiments including alternating galvanostatic and potentiostatic treatments, where constant current density ensured anodic dissolution followed by biasing the sample at sufficiently

negative potential and measuring the cathodic current. Interestingly, the cathodic current increased after increasing anodic polarization [134].

Other popular procedures to assess magnesium corrosion are weight loss and hydrogen collection measurements. In the weight loss measurement, the mass of the sample is measured before and after the experiment, and the corrosion rate can be easily calculated from the mass loss and the time of the exposure to corrosive impacts. It is also possible to determine the corrosion rate by measuring the hydrogen evolved in the cathodic reaction. The charge neutrality principle implies that the anodic and cathodic currents should be equal in spontaneous corrosion, thus the amount of the H_2 evolved is an indicator of the dissolved Mg^{2+}. The practical difficulties of collecting the hydrogen gas effectively was successfully overcome using a gravimetric method instead of the volumetric one [108]

The reduction potential of magnesium is beyond the reduction potential of the water. Therefore the monitoring of the evolved H_2 is the regarded the most accurate method for the measurement of the corrosion rate using the amperometric mode of the SECM [134]. Despite the growing use of ion selective microelectrodes [57], amperometric detection remains the prevailing mode of SECM applied in the study of Mg corrosion [135].

3.5. Remarks on the magnesium corrosion

In the Results and discussion part, the magnesium corrosion plays an important role. Hence, in this Section a bit more specific description on the topic was provided than it would be expected from the introduction of a PhD thesis. The author felt this very important, because the literature of the anomalous hydrogen evolution on anodically polarized magnesium is incredibly broad. I sincerely hope that the readers feel that the experimental results on this issue are very chaotic and further studies needed to have a better picture of the NDE. Up to now, no scientific consensus has been raised, and even the leader scientists publish contradictory results from year to year. My goal was primarily not to resolve the whole issue; that goes beyond the limits of a PhD work. Neither revealing the mechanism was among my aims. On the other hand, I sincerely believed before I started the experimental work that SECM might provide some new and interesting insights into the NDE process, and eventually confirmfirm or contradict the prevailing ideas.

Part II. Experimental

II.1. Materials

All the ion selective membrane components were supplied by Sigma Aldrich (St. Louis, MO, USA). Ammonium chloride, potassium chloride, sodium chloride, zinc-sulfate heptahydrate, copper-sulfate pentahydrate were purchased from Reanal (Budapest, Hungary). Magnesium-chloride hexahydrate and disodium salt of ethylenediammin-tetraacetic acid (EDTA) were supplied by Merck (Darmstadt, Germany). The solutions were filled up with ultrapure water (Millipore water system, specific conductivity $\kappa = 5.6 \times 10^{-6}$ S/cm; Merck Millipore, Billerica, MS, USA).

Borosilicate capillaries (outer dia. Ø = 1.5 mm, inner dia. Ø = 1.0 mm) were obtained from Hilgenberg GmbH (Germany). The silanization solution was dichlorodimethylsilane purchased from Sigma-Aldrich (Taufkirchen, Germany). The 33 μm diameter carbon fiber used for the solid contact microelectrodes were obtained as generous gift (Specialty Materials, Lowell, MA, USA). The PEDOT coating on the carbon fibers was prepared using 3,4-ethylenedioxythiophene (EDOT, HC Starck GmbH, Goslar, Germany) dissolved in 1-butyl-3-methylimidazolium hexafluorophosphate ($BMIM^+$ PF_6^-) ionic liquid.

Pt microelectrodes (ME) were fabricated from 25 μm diameter wire (Goodfellow, Cambridge, UK). For the Mg- Fe galvanic couple amples, 99.99% purity iron foils (Goodfellow, Cambridge,UK) and AZ63 alloy sacrificial boiler anode were employed. The epoxy resin EpofixKit used for sample sleeving was purchased from Struers (Denmark). The metal wires (Ø = 0.125 mm) of the pure metals, namely copper aluminum, iron, zinc and magnesium were Goodfellow products (Cambridge, UK). The antimony powder used for the preparation of pH sensitive antimony microelectrodes was purchased from Aldrich (Saint Louis, MO, USA).

II.2. Equipments

The single barreled micropipettes were prepared using a P-30 type capillary puller (Sutter Instruments Co., CA, USA). For multi-barrel capillary preparation, a Narishige PE-2 pipette puller (Tokyo, Japan) provided with a rotary chuck was employed. The potentiometric response time measurements were performed with a homemade, battery powered voltage follower based on TL071 operational amplifier. The output of the voltage follower was connected to e-Corder 410 type data acquisition device (eDAQ, Australia) providing 1000 Hz sampling frequency.

II.2.2. Applied potentiostats

The potentiostats connected to the SECM equipments will be described in the next section. Other electrochemical experiments were performed using the AutoLab Electrochemical Workstation Autolab POTSTAT 12 (Echochemie, The Netherlands). It was employed for the preparation and testing of the PEDOT coated solid contacts. The equipment is controlled by GEPES 4.9.005 software. The polarization experiments were performed with a CHI 700C electrochemical workstation (CH Instruments Inc., USA).

II.3. Scanning electrochemical microscopy

In this work, three different SECM instruments were used: one commercial and two homemade apparatus. The commercial one was built by Sensolytics (Bochum, Germany), equipped with a high quality stepper motor-controlled *XYZ*-positioning system with 25 mm range and 20 nm resolution in each axis. An Autolab bipotentiostat (Metrohm Autolab BV, Utrecht, The Netherlands) was used for the local electrochemical measurements. The components of the SECM were controlled with a personal computer.

Another SECM used in this work was built in our laboratory. In brief, the main component were three (UE166PP) stepper motor-driven linear, and the 3D positioning stage (Newport, Irvine, CA, TypeMMFN25PP). The controller and the drivers were homemade. The smallest step attainable with the stepper motors is 75 nm. The measuring unit was an EF437 bipotentiostat (Elektroflex Ltd., Szeged, Hungary). The instrument was connected to the PC through a PCLab-812PG measuring and controlling interface card (Advantech, USA). The inputs of the fine positioning step motor driven stages were connected to the power interface. The potentiostat was directly connected to the parallel port of the PC and to the A/D card. The D/A converters of the interface card facilitated the control of the movement of the positioner stages. The operating software was written by Balázs Csóka.

Domiline 15 linear stages were built in the third SECM. Three Nema 17 type stepper motors were used. The motors were controlled by a SD4DX USB Controller (Peter Norberg Consulting, Inc. 117 South Clay Ave. Ferguson, MO, USA), and driven by a Gecko step-and-direction driver board (Geckodrive, Inc. 14662 Franklin Ave, Santa Ana, CA.). The control software was written in Java by András Kiss.

In the case of potentiometric measurements, a homemade voltage follower based on a 10^{12} Ω input impedance operational amplifier (mod. TL071, Texas Instruments, Dallas, TX, USA) was interconnected between the cell and the potentiometric input of the system.

Two scanning algorithms were used for recording the 2D SECM maps. The so-called meander algorithm is sketched in **Fig 14A**. In brief, starting from the red dot, the scanning direction along the *X* axis alternated from line to line, so as the probe reached the last raster point of the line, for instance in the *X*+ direction, and when the measurement for that certain point was finished, it moved one step in the *Y* direction and continued the scan in the opposite (*X*-) direction. The green points represent the local measurement points composing the 2D raster map. The blue spot is the last measurement point of the scan.

For circularly symmetric targets – that is the case in many applications, such as the scan above the cross section of wires – the circularly symmetric algorithm depicted in **Fig 14B** seems to be more advantageous. The algorithm was built in the homemade software of the third SECM and described by its creators in [136]. The tip is firstly positioned to the center of the sample with the aid of a microscope. The scan starts at the red spot and the tip travels along circular trajectory with increasing radius. The images will be presented in square based maps in Quikgrid software that is done by extrapolating the values measured in the outermost circle to the edges of the triangle. It is advantageous if the circular sample surface is in the center and the the sides passive embedding matrial faces the tip. Since usually it is above the insulating resin or far from the open micropipette sample, only the values in the bulk are extrapolated, hence a good estimation can be made on the background values.

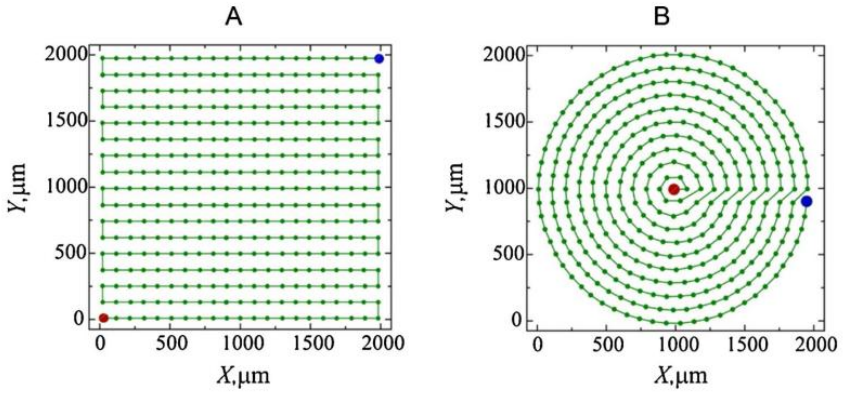

Fig 14. Sketches of the two algorithms used in SECM measurements. (**A**) typical meander algorithm employed in SECM set-ups, (**B**) circular, polar-coordinate based scanning algorithm.

II.4. Scanning vibrating electrode technique

SVET equipment was manufactured by Applicable Electronics Inc. (Forestdale, MA, USA). It contains a preamplifier, PSDA-2, a Phase Sensitive Detector Amplifier, capable to operate as Lock-In Amplifier, the motor controllers, the piezo unit that vibrates the tip parallel and perpendicular to the sample, and an oscilloscope. All units are controlled with a personal

computer using ASET 2.00 software. The sensing probe was a 2-3 cm long Pt/Ir wire insulated with parylene C except on its extreme where the tip was of 10 μm diameter. A platinum black deposit was grown electrochemically on this end to obtain the appropriate capacitance. The capacitance was checked from time to time and if it reached a critical value, the deposit was occasionally renewed following the description in the manufacturer's instructions. The platinization solution contained 0.25 ml lead acetate (1 w/w%) and 0.4 ml hexachloroplatinic acid (4 w/w%) filled up to 15 ml final volume with double ion exchanged water. Another platinum wire was used as counter electrode. I applied a negative polarization between -1.5 and -2 V for 30 seconds, producing ca. -300 nA current. Subsequently I increased the potential to -5 between 6 V, so that the current increased to -1050 nA. At last, I applied maximum negative polarity six times for half seconds. The capacitance was checked in the same solution and the platinization was accepted to be successful when the capacity was at least 2 nF. Once the adequate deposition was obtained, the vibration on the *Y* and *Z* axis should be calibrated. It is done when the tip is not immersed into any solution. The vibration along the *X* axis was checked with a camera. If the frequency deviated from the certified value (the normal and the parallel directions to the surface, with 78 and 185 Hz respective vibration frequencies), it could be adjusted using a dial. The vibration along the Z axis could be adjusted with the help of a 45º inclined mirror. The recommended value of the vibration along the *Z* axis is 78 Hz.

A video camera connected to an optical microscope was introduced in the system both to establish the probe to sample distance, and to follow the movement of the vibrating electrode over the sample during operation. The tip positioning was performed avoiding the tip from touching the sample by first focusing on the sample using the precision motors. Next, the focus was raised vertically 100 μm and the probe was moved stepwise so that the very end of the tip could be seen on the screen perfectly focused.

II.5. Samples

In most SECM experiments described in this dissertation, the samples were metal pieces embedded in an epoxy resin sleeve. The metals were mounted in a homemade mold and then the recipient was filled with the 1:8 mass-to-mass ratio mixture of the Epofix hardener and resin. The curing time is 12 hours at room temperature. The samples were gradually abraded and polished using wet abrasive paper (down to 4000 grit) and polishing cloth with alumina slur (in 1, 0.3, 0.05 μm grain sizes).

In the experiments, the polished surface faced up and sellotape was wrapped around the sample creating a small container for the test electrolyte, with the polished specimens at the bottom of this "vessel" (see in **Fig 15 A**).

The "cut edge" system used in Chapter 1 of the Results and Discussion part was made from a painted galvanized steel sheet. The thickness of the steel foil was 400 μm, while the galvanized layer was 25 ± 5 μm electrodeposited zinc. A 5 μm thick polyester primer was applied to both sides of the galvanized steel foil, whereas a single 20 μm thick polyester topcoat containing TiO_2 was applied only to one side. A 3 mm × 4 cm strip was cut from the

coil-coated metal sheet, and then the painted layers were removed using acetone. This procedure retains the zinc layers, that is, the resulting specimen was the embedded steel coated with only the galvanized Zn layers in a "sandwich" configuration. After polishing, only the cross section of the metal sheet was exposed (that will be indicated as Zn/Fe/Zn in the Figures in Chapter 1).

In Chapter 1 a sample containing 1-1 mm diameter Zn and Fe wires was employed too (see **Fig 15A**). The electric connections were soldered to the wires protruding at the rear of the epoxy body, thus ensuring electric connection between the two metals could be established. The separation between the metals was about 1 mm. Similar assemblies were used in Chapter 2 where square based magnesium (AZ63 alloy) and iron rods were embedded in the epoxy resin sleeve. In Chapter 2, 0.125 mm diameter Mg, Zn, Al, Fe, Cu wires were used in the construction of different galvanic pairs. In Chapters 3 and 4 either 1 mm × 1mm square based rods or strips (0.3 mm × 1.5 mm) of magnesium and AZ63 alloy were used.

The sample containing Zn^{2+} and Cu^{2+} sources was prepared as follows. Micropipettes were prepared with relatively large orifice (~0.3 mm) and filled with hot, 5 % agar-agar solution saturated with $ZnSO_4$ or $CuSO_4$. Then a hole was drilled in a cap of a centrifuge tube. The micropipette was fixed in the hole, so that the orifice was located in the inner chamber of the cap. This assembly was placed in the sample holder of the SECM upside down, as it can be seen in **Fig 15B**. The measuring tip was positioned above the orifice of the micropipette source with the aid of a digital microscope. In this case the tip-sample distance can only be estimated by visual observation to avoid probe-sample collision. Using the microscope, this can be done within a few micrometer precision.

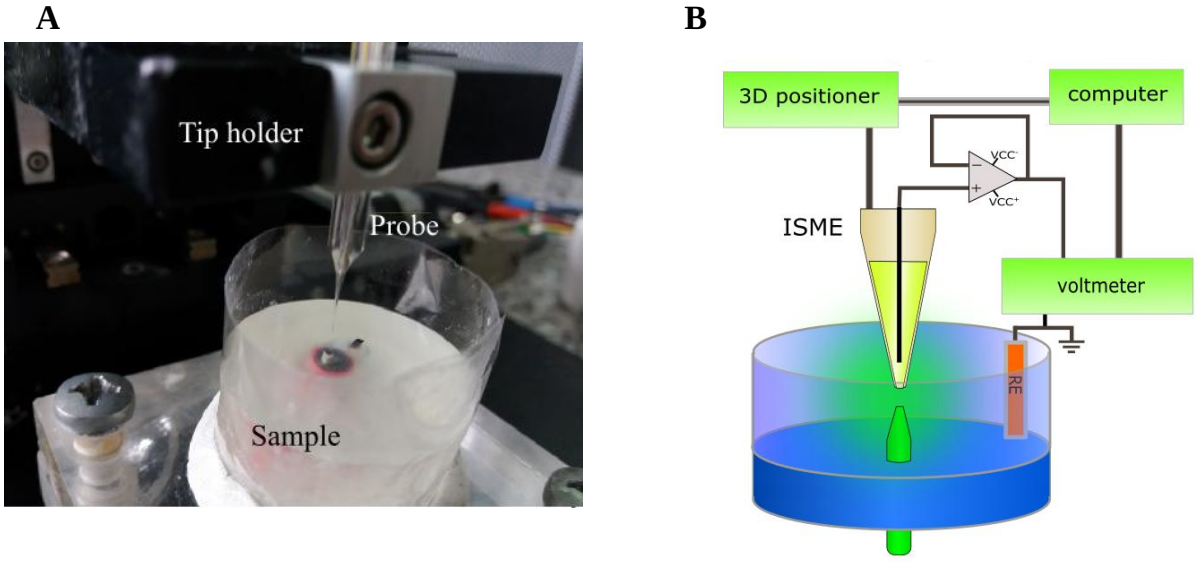

Fig 15. A: Photograph of the SECM probe above an Mg-Fe galvanic pair containing sample. During the measurements the cell was completed with the reference and – in amperometric operation- the counter electrodes, and the small container was filled with the testelectrolyte. B: Sketch of the micropipette-type metal ion-source sample producing a spherical concentration distribution.

II.6. Electrodes

II.6.1. Preparation of the Pt microelectrodes

The preparation protocol is described in details in [137]. Shortly, borosilicate capillaries were first soaked in "Piranha" solution, then subsequently rinsed with ultrapure water. Then, one end of the capillaries was closed using the oxidizing flame of the micro gas torch. Afterwards, the Pt microfiber of 25 μm diameter was introduced into the capillaries and sealed an approximately 1-2 cm long section into the glass to fix the wire. This was done using a device providing fine movement. The capillary was fixed vertically in this device with the closed end facing down and moved slowly up and down into a heated, glowing kanthal coil. In order to avoid bubble formation in the softened glass, the other end of the capillaries were connected to vacuum. The electric connection was performed by soldering. The sealed ends were polished using abrasive papers, until the RG<10 was achieved. The surface of the microelectrode was wet-polished on polishing microcloth using aqueous alumina slurries of 1.0, 0.3, 0.05 μm grain size.

II.6.2. Preparation of the pH sensitive antimony microelectrodes

The antimony microelectrodes were prepared by melting antimony powder in a crucible using glass flame. The molten metal was then sucked into a thick wall capillary by applying vacuum on the other end of the tube using a 50 ml syringe attached to the capillary with rubber tube. After the metal cooled down, thinner antimony wires were prepared by manual pulling. This can be done because the melting point of the antimony and the borosilicate glass are close to each other. The pulling step can be repeated until the desired diameter range of the glass coated antimony is achieved. Then the microfibers were checked under the microscope and segments without discontinuity were selected to prepare the microelectrodes.

In **Fig 16** a micrograph of an antimony microfiber and the sketch of the antimony electrode can be seen. It has to be noted that the contour of the glass shield was redrawn using Inkscape software. The reason is that focusing at this magnification was not satisfactory with the Leica microscope. The diameter of the antimony fiber can be estimated by comparing the number of pixels of a line with the length of the scale bar with a line that is as long as the diameter of the Sb. Based on this rough estimation, the diameter of the antimony fiber is about 3 μm, and in can be decreased to the submicrometer range in the capillary puller, however in our experiments such high resolution was not necessary to obtain so the microelectrodes prepared were always in the few micrometer up to 20 μm range. The selected antimony microfibers were glued into capillaries. The electric contact was implemented by using either mercury or silver epoxy glue. In the first case, the copper wire was simply introduced into the mercury in the capillary (see in **Fig 16. B**). In the latter case, the antimony fiber and the copper wire were glued with silver epoxy before they were introduced in the

capillary. The two-component glue was mixed in 1:1 ratio and the glued wires were placed into the oven at 80 °C for 45 min.

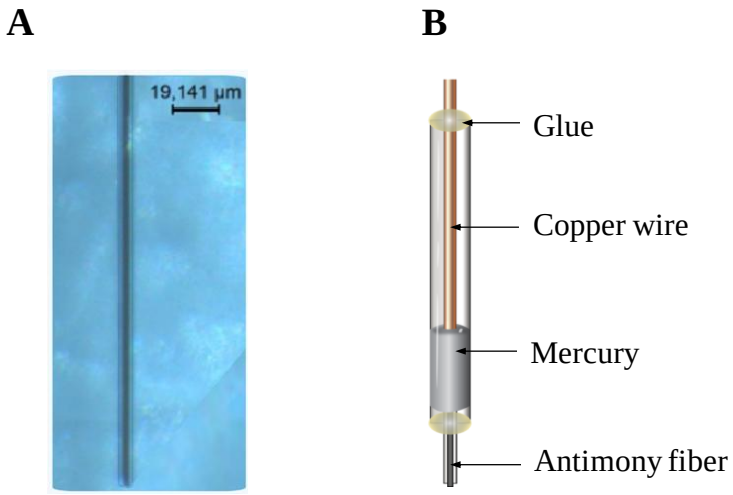

Fig 16. (**A**) Micrograph of the antimony microfiber, and (**B**) sketch of the antimony microelectrode.

II.6.3. Preparation of the ion selective microelectrodes

In this work, 4 different kinds of liquid membrane ion selective microelectrode were used, for detecting ammonium, zinc(II), copper(II)- and magnesium(II) ions. The compositions of the membranes are listed in tables below. The main components were the ionophore, poly-vinyl-chloride (PVC), 2-nitrophenyl-octyl-ether emollient and potassium tetrakis(4-chlorophenyl)borate lipophilic ion exchanger. The components were mixed with small amount of tetrahydro-furan that was allowed to evaporate before the ionselective electrodes were used. The percentages differed slightly from the nominal compositions in Tables 1-4. The recipes were adapted from previous works in our laboratory, except for the Cu ISME which was firstly prepared by me. The chemical structures of the ionophores are depicted in **Fig 17**.

In the first step of fabricating micropipette ISE-s, borosilicate glass capillaries were pulled and silanized using 5 % dichloro-dimethyl silane in heptane. The micropipettes were placed into Petri dish with 500 µl silanizing solution in a watch glass it was closed with a watch glass. The closed Petri dish was put in the oven for 30 min at 120 °C. The preparation of the solid contact consisted in the electrochemical polymerization of PEDOT on a 33 µm diameter carbon fiber. About 1–2 cm long carbon fiber was employed, and attached to a copper wire with silver epoxy adhesive. The wire was used as working electrode in 0.1 M EDOT-containing $BMIM^+$ PF_6^- ionic liquid solution, with silver reference and platinum auxiliary electrodes. In the polymerization step, 10 consecutive cyclic voltammetry cycles were applied in $-0.9 \leq E \leq 1.3$ V range. The PEDOT coated carbon fiber was doped in 0.1 M KCl aqueous solution through the application of 15 consecutive potential cycles in the $-0.9 \leq$

E ≤ 0.8 V range. In the same solution, the performance of the obtained coating was tested by cyclic voltammetry, in the -0.4 ≤ E ≤ 0.5 range; 5 consecutive scans were taken (not shown). All the cyclic voltammetric treatments were performed at 0.05 V/s scan rate.

Table 1.

NH_4^+ selective microelectrode	
ionophore	3.1 %
PVC	3.1%
potassium tetrakis(4-chlorophenyl)borate (PTCB)	0.9%
2-nitrophenyl-octyl-ether	92.9%

Table 2.

Zn^{2+} selective microelectrode	
ionophore	2.2 %
PVC	4.0 %
potassium tetrakis(4-chlorophenyl)borate (PTCB)	0.5%
2-nitrophenyl-octyl-ether	93.3 %

Table 3.

Cu^{2+} selective microelectrode	
ionophore	2.2 %
PVC	4.0 %
potassium tetrakis(4-chlorophenyl)borate (PTCB)	0.5%
2-nitrophenyl-octyl-ether	93.3 %

Table 4.

Mg^{2+} selective microelectrode	
ionophore	1.5%
PVC	2.6 %
potassium tetrakis(4-chlorophenyl)borate (PTCB)	1.4 %
2-nitrophenyl-octyl-ether	94.5 %

The hydrofobized capillaries were either backfilled or frontfilled with about 2-3 μl ion selective cocktail, and the solid contact was introduced into the capillary, so that the end of the PEDOT coated carbon fiber could be as close to the orifice of the tip as possible. Usually, this meant 1-2 mm liquid column between the membrane surface and the solid contact. Then, the electrodes were left at the air for 36 hours to evaporate the THF.

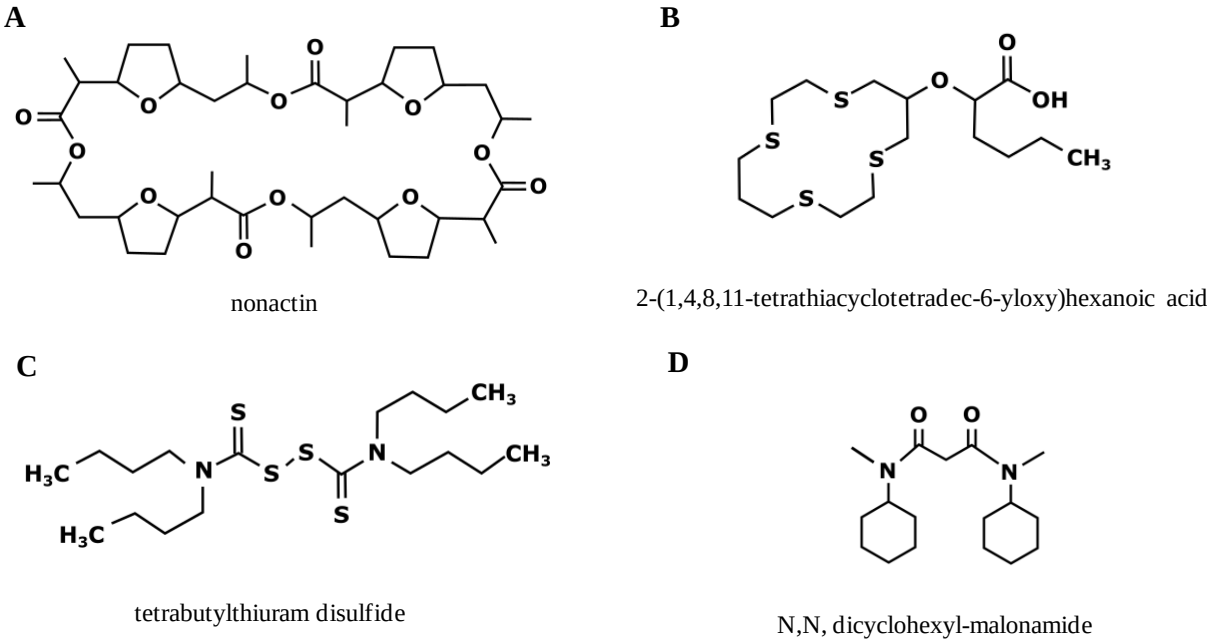

Fig 17 Chemical structure of the ionophores employed: (**A**) ammonium-, (**B**) copper(II)-, (**C**) zinc(II), (**D**) magnesium(II) selective ionophores.

II.6.4. Preparation of multi-barrel electrodes

Three types of double- and triple-barrel electrodes were prepared, depending oh the contents of the electrode body, namely:

1. only liquid membrane ion selective microelectrodes;
2. liquid membrane ion selective electrodes and microreference electrodes;
3. antimony microelectrodes (apart from the ISME and the microreference).

The three types required slightly different preparation procedures. A general description is provided below with remarks to any eventual divergence.

First, borosilicate capillaries were attached together in odd number, and then they were placed into chucks of the vertical puller (See step 1 in **Fig 18**). The lower, rotary chuck was splayed, allowing the capillaries to be twirled after the area in the coil softened without applying pulling force. This first heating step served to merge the capillaries together. Originally, I rotated the lower chuck by 180°, but later I decreased the angle when I prepared multi-barrel capillaries with the intention to have an antimony microelectrode in the body, because the curvatures in the capillaries made difficult the placement of the antimony microfiber to the tip. It has to be noted that the antimony microfibers with diameter < 20 μm are flexible and no fracture was caused when they were positioned close to the opening of the tip. After rotation, the capillaries were let to cool down, then another heating step followed, but this time the splay was removed and the capillaries were pulled to be multi-barreld

micropipettes (cf. **Fig 18**, step 2). The silanization was performed using the same procedure as in the case of single-barrel capillaries, except for the multi-barreal electrodes containing a microreference electrode. In that case, the capillaries had to be selectively silanized, leaving one barrel to be hydrophilic in order to contain the Ag/AgCl/(0.1 M) KCl microreference electrode. To this end, a simple device was made from a glass vial (see step 3 in **Fig 18**). An orifice of 1.0 mm was drilled on the plastic cap of the vial and a capillary of 1.0 mm outer diameter was glued into it. The capillary protrudes so the ISME barrel of the multichannel electrode body can be placed on it and fixed. The orifice of the reference barrel was closed with water, to avoid the silanizing agent to get in that barrel from the tip side. Then the silanizing agent was pipetted into the vial and the whole assembly was placed inside the oven and left there at 50 °C for 2 hours. As the silanizing agent evaporates from the vial, it passes through the glued capillary and gets into the barrel intended to be ISME and hydrophobizes it. The reference barrel is not connected to the chamber, so it remains hydrophilic, ideal for the aqueous filling solution of the microreference electrode. The remaining steps are very similar to the preparation of the single-barrel microelectrodes. The ISME barrels were filled with the chosen cocktail and the carbon fiber was placed in it. The reference barrels were filled with 0.1 M KCl solution and a chlorinated silver wire was introduced into the solution. The antimony barrels were made by positioning the antimony microfiber to the end of the tip. The microfibers protruding from the aperture of the tip were pulled out so that the microfiber was stucked into the orifice (in the area where it has the same outer diameter as the orifice diameter). This protruding part was cut to have the antimony barrel at the same vertical position. The electric contact was established using mercury and copper wires.

The first double-barrel microelectrode I have made is depicted in **Fig 19**. The sketch and the photograph show that the micropipette was prepared with 180° rotation angle. The left barrel contains the Zn ISME, the right one is antimony microelectrode. **Fig 20.** shows the Mg ISME with the microreference electrode. In that case, selective silanization was applied, so that only the Mg ISME containing barrel was silanized. In **Fig 21** the triple-barrel electrode containing an Mg ISME, a Sb microelectrode and a Ag/AgCl microreference electrode containing can be seen.

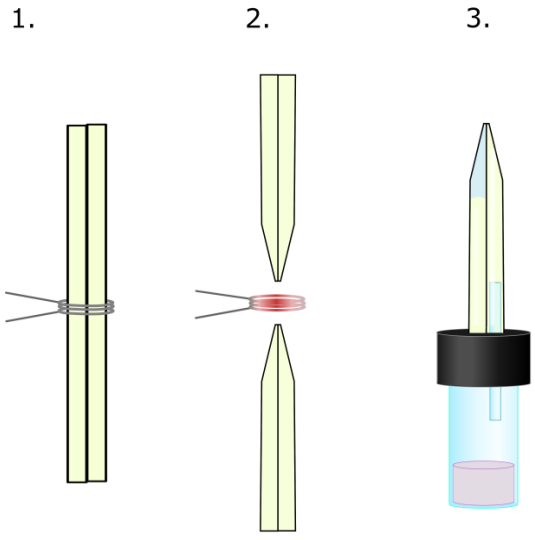

Fig 18. Scheme of the preparation of the double barreled capillaries (steps 1 and 2), and the selective silanization for the assembly with incorporated microreference electrodes. The vial is filled with the silanizing agent and its vapours can only pass through the barrel connected to the chamber. In this way, the inner inner surface of the other barrel remains hydrophilic.

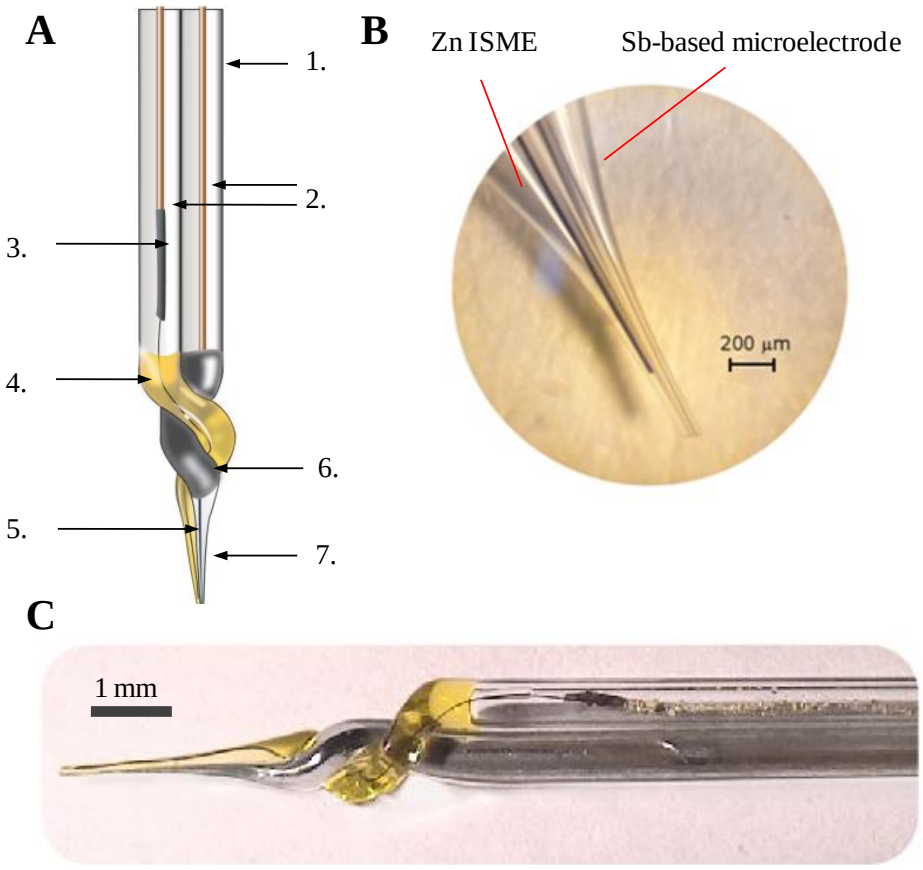

Fig 19. (**A**) Structure of the double-barrel ion-selective microelectrode. 1: double-barreleborosilicate capillary, 2: copper wires, 3: Ag-epoxy, 4: ion selective cocktail, 5: PEDOT coated carbon fiber (∅ = 30 µm), *6*: Mercury, 7: Antimony fiber. (**B**) and (**C**) are mcrophotographs of the electrode assembly.

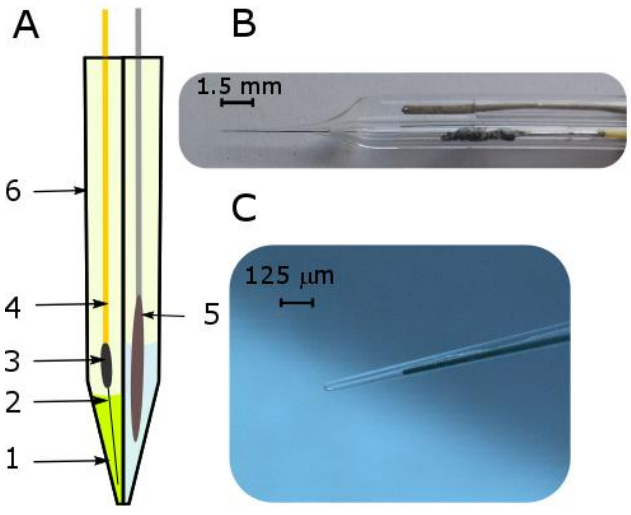

Fig 20. New-double barrel electrode assembly for potentiometric SECM: (**A**) Sketch, and photographs of the (**B**) double-barrel electrode and (C) of its tip. 1: Mg^{2+} ion selective cocktail, 2: PEDOT coated carbon fiber (∅ = 33 µm), 3: silver epoxy glue; 4: copper wire for electrical connection; 5: Ag/AgCl micro-reference electrode; 6: double barrel borosilicate capillary.

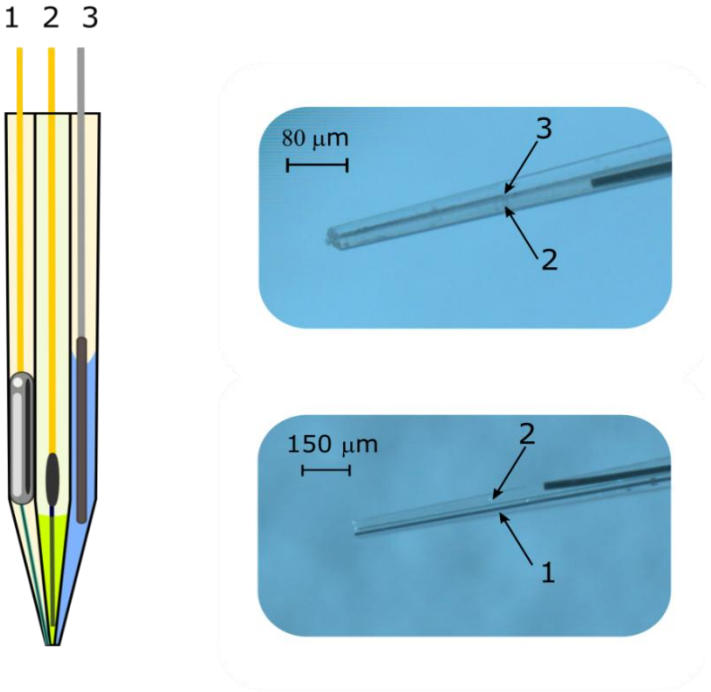

Fig 21. Sketch and photographs of the triple-barrel microelectrode assembly designed for potentiometric SECM imaging. 1, pH-sensitive antimony electrode; 2, Mg^{2+} selective microelectrode; 3, Ag/AgCl micro-reference electrode.

II.6.5. Calibration of the ion selective microelectrodes

The calibration of the liquid membrane microelectrodes was carried out in dilution series of the primary ions in 10^{-1} to 10^{-6} range with tenfold increments between consecutive solutions ($\Delta pMe=\Delta(-\log[\text{metal ion concentration}])=1$). An Ag/AgCl/KCl (3M) reference electrode was used, and the electrodes were connected to the operational amplifier and the voltmeter. The calibration was always initiated with the most diluted solution and continued stepwise to the more concentrated ones. In the case of the antimony microelectrode the calibration was done in the $4 \leq pH \leq 11$ range using 1 pH unit increments. To this end, Britton-Robinson buffers were prepared and their pH was check with a "conventional" pH meter and combined glass pH electrode. The calibration was started by introducing the antimony microelectrode and the Ag/AgCl/KCl (3M) reference electrode in the calibrating solution. In **Fig 22**, the calibration plots of the double-barrel Zn ISME/Sb microelectrode can be seen. The slope of the antimony microelectrode was slightly less than the Nernstian slope (50.5 mV/pH unit vs. 59.2 mV/pH unit), a feature that is not unusual in the literature for the single-barrel electrodes [138,139]. For the Zn ISME calibration plot, the concentration values were converted to activities, using the following equation for the mean activity coefficient:

$$\lg \gamma_{\pm} = -A \cdot \left| z_{+} \cdot z_{-} \right| \cdot I^{1/2} \tag{48}$$

where A is a constant, z_+ and z_- are the charges of the cation and the anion respectively, and I is the ionic strength, given by the following:

$$I = \frac{1}{2} \sum_{i} m_i z_i^2 \tag{49}$$

where m_i and z_i are the molality and the charge of the primary ion. The slope of the calibration curve is nearly Nernstian for almost 4 orders of magnitude activity range between pZn=1.6 and pZn=5. This is in good agreement with the previous reports of the single barrel Zn ISME's used in our group [140].

The slopes for the Mg ISME and ammonium ISME were also very close to the corresponding theoretical values (cf. **Fig 23A** and **23B**). The calibration of the Cu ISME will be presented later together with other characteristics.

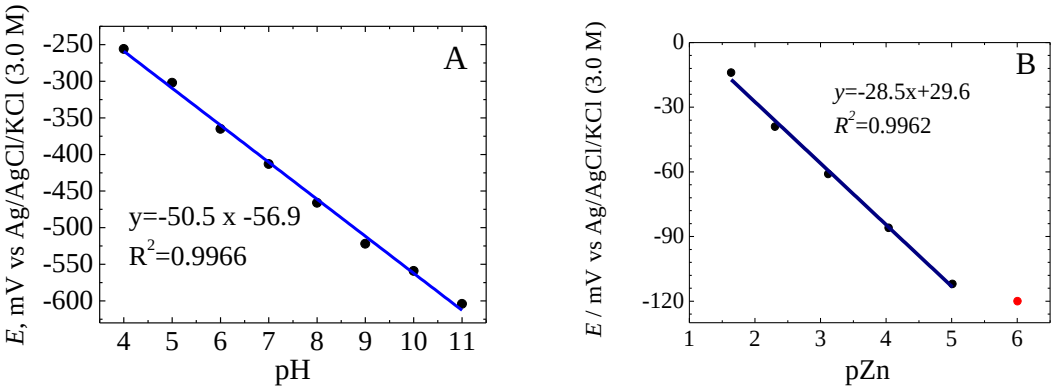

Fig 22. Calibration plots of a double-barrel microelectrode composed of a Zn ISME and an Sb microelectrode. (A) Calibration of the antimony microelectrode in a series of Britton Robinson buffers; (B) calibration of the Zn ISME calibration in $ZnSO_4$ solutions.

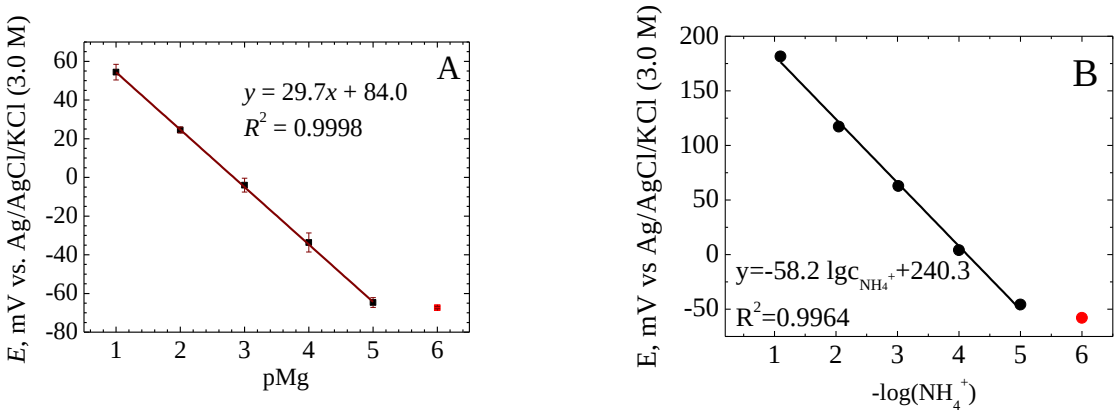

Fig 23. (A) Calibration plot of the Mg ISME in $MgSO_4$ solutions and **(B)** the ammonium ISME measured in NH_4Cl.

In the saline environment applied in this work, the selectivity of the ion selective electrodes might have a crucial role on the correct assessment of the corrosion reactions.

For the Zn ISME, the log (K_{ij}^{pot}) values for Na^+, Fe^{2+} and Fe^{3+} have been determined with the separate solution method (SSM). The same calibration method was carried out in series of solutions of the interfering ions, as it was in case the primary ion (Zn^{2+}). As it is well known, log (K_{ij}^{pot}) can be defined as:

$$\log (K_{ij}^{pot}) = \left(E_j^0 - E_i^0\right) \frac{z_i F}{2.303RT}, \tag{50}$$

where E_j^0 and E_i^0 are the individual potentials of the interfering (j) and the primary (i) ions extrapolated to 1 M activity, z_i is the charge of the primary ion, F, R and T have their usual meanings. The potential – logarithmic metal ion activity plot was used for the calculation of

the selectivity coefficients, and the calculated log (K_{ij}^{pot}) values for all the electrodes used in this work are listed in **Table 5**. As example, a set of curves for the Zn ISME can be seen in **Fig 24**.

Table 5.

log ($K_{Zn^{2+},Fe^{2+}}^{pot}$)	-2.02
log ($K_{Zn^{2+},Fe^{3+}}^{pot}$)	-2.13
log ($K_{Zn^{2+},Na^{+}}^{pot}$)	-3.24
log ($K_{Zn^{2+},Cu^{2+}}^{pot}$)	-0.78
log ($K_{Mg^{2+},Na^{+}}^{pot}$)	-2.50
log ($K_{NH_4^{+},K^{+}}^{pot}$)	-0.71

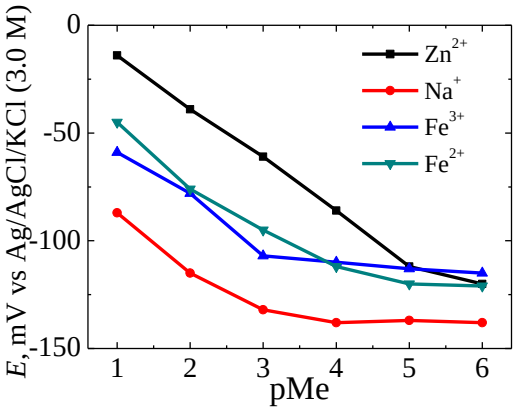

Fig 24. Experimental curves used for calculating selectivity coefficients of the Zn ISME with the separate solution method.

II.6.6. Measurement of the dynamic response of the microelectrodes

The response time of an ion selective microelectrode was measured doing activity step experiments. This is implemented by a fast increase of the activity of the primary ions done by the addition of a more concentrated solution. The decrease of the activity of the primary ions is also possible by rapid dilution. If a high precision solution jet system providing fast solution flow is not available, the so called dual drop method can be applied [141]. However, in this arrangement, there is a short, but not negligible time when the electrodes are not immersed in solution and this biases the accurate reading of the response curve. Also the response time has two components: an electronic part and a mixing term and usually the exchange of the solution 1 to solution 2 is sluggish compared to the electronic term. That is, one only measures the rate of the exchange of the solution or the slope of the activity step, which has nothing to do with the ISME's response characteristics. The addition of a portion of the stock solution into a vigorously stirred solution, while the electrodes are immersed and the potential is recorded, also did not seem to be suitable. In fact, the activity step should be as

steep as possible to measure the real response time originating from the electrode resistance and the capacitance of the measuring system. To this end, a small volume homemade equipment was designed and prepared together with a fellow PhD student, Abdelilah Asserghine (see the sketch in **Fig 25**). In the experiment, the solution of activity a_1 can be rapidly exchanged to a_2 by a fast and excessive injection of the second solution. The equipment consists of flexible tubes (with a total volume of ca. 200 μl) in which the microelectrode and the reference electrode can be placed tightly, so the solution will not leak through the orifices for the electrodes. The reference electrode was placed downstream so that the potassium ions will not perturb the signal of the ion selective microelectrode. First, a portion of the first solution was introduced in the tube with a syringe. Once a stable potential reading was obtained the syringe was replaced by another one containing the second solution, and it was injected rapidly while the potential was recorded with 1000 data point/second frequency.

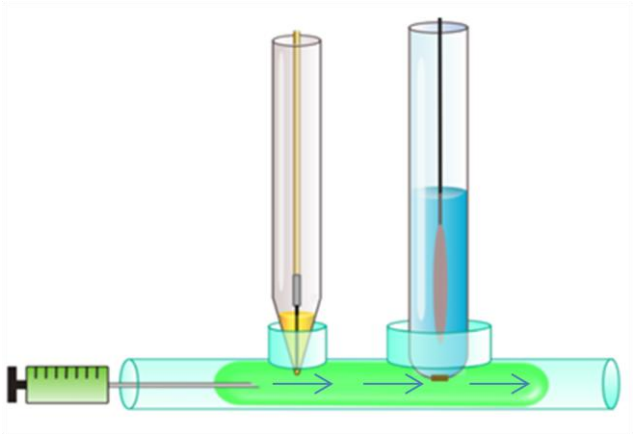

Fig 25. Sketch of the activity step experiments. The blue arrows indicate the direction of the solution flow.

II.6.7. Characterization of the Cu ISME

As it was mentioned earlier, a liquid membrane Cu^{2+} selective microelectrode was prepared by me for the first time.

The internal resistance of the ion selective microelectrodes was measured using the voltage divider method. For this studies sufficiently high resistors were selected (R_k=100-150 MΩ). The potential of the cell was measured against an Ag/AgCl (3.5 M KCl) reference electrode using a high input impedance voltmeter. After attaining steady open circuit potential, R_k was switched in the circuit for the measurement of the voltage (U_k) established after R_k was inserted, and ΔU was determined as $\Delta U = U_{OCP} - U_k$. The resistance of the ISME could then be determined using the following equation:

$$R_{ISME} = \frac{\Delta U \cdot R_k}{U_k} \tag{51}$$

It is generally known about this method, that more precise value can be calculated when the measured U_k is close to ½ U_{OCP} [141]. The resistance value was obtained by averaging 3 $\Delta U/U_k$ values, and it was found 373 MΩ.

The calibration curve along with that recorded in 1 M $ZnSO_4$ electrolyte are shown in **Fig 26**. The red points were excluded from the fitting and as it can be seen, the copper selective electrode shows nearly Nernstian response in a wide 5-orders of magnitude range. From the results measured in the mixed solution, the selectivity coefficient could be calculated. The intersection (Q) of the line fitted on the blue points and the linear fit on the last three points (pCu=4-6) is at $(pCu)_Q$=3.07. The selectivity coefficient can be calculated from the following equation knowing the mean activity coefficient of 1 M $ZnSO_4$ [142]:

$$K_{Cu,Zn}^{pot} = \frac{(a_{Cu})_Q^2}{(a_{Zn})^2} \tag{52}$$

From this equation $logK_{Cu,Zn}^{pot}$=-4.5. This value is in good agreement with the value reported by the manufacturer in the datasheet of the ionophore ($logK_{Cu,Zn}^{pot}$=-4.7.). The evaluation of the separate solution method faced some difficulties, since the calibration of interfering ions (Zn^{2+}) did not show Nernstian behavior, although the value is not significantly different from the latter two ($logK_{Cu,Zn}^{pot}$=-4.4). The selectivity coefficients determined using the mixed solution method are listed in **Table 6**:

Table 6.

log ($K_{Cu^{2+},Na^{+}}^{pot}$)	-4.52
log ($K_{Cu^{2+},K^{+}}^{pot}$)	-2.7
log ($K_{Cu^{2+},Mg^{2+}}^{pot}$)	-6.03*
log ($K_{Cu^{2+},Fe^{2+}}^{pot}$)	-3.01
log ($K_{Cu^{2+},Zn^{2+}}^{pot}$)	-4.50

The limit of detection was found to be larger than it was expected from the datasheet, namely pCu_{LD}=5.02 although Sigma claimed pCu_{LD}=6.09. On the other hand the linearity range is wider, namely 10^{-5}-10^{-1} M, whereas the reported value is 10^{-6}-10^{-3} M. These differences can be explained by the fact that the manufacturer tested the ionophore in conventional ion selective electrodes and the cocktail composition of the ion selective microelectrode is different, and this can affect the linearity range and the limit of detection. Nevertheless, the wider linearity range is very advantageous in SECM applications, because in the proximity of the samples, very rapid activity changes can be expected sometimes, even in the range of several orders of magnitude.

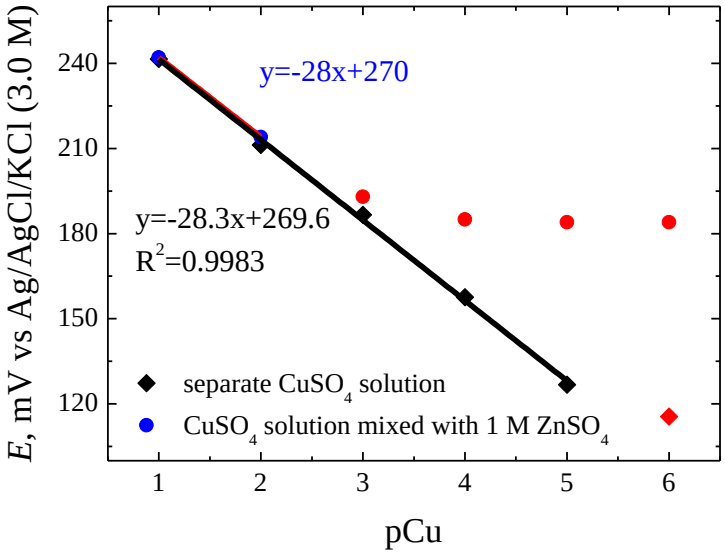

Fig 26. Experimental plots used for the determination of the selectivity coefficient of the Cu ISME towards Zn^{2+} ions.

The response time of the Cu ISME was measured in the activity step experiment in the same manner as described in the previous section. First, when the electrodes were placed into the vessel, it was filled with 10^{-3} M $CuSO_4$ solution. Then the recording of potential of the microelectrode was started with 1000 Hz sampling frequency. The solution was replaced several times increasing the concentration to 10^{-2} M and back to 10^{-3} M. In **Fig 27**, a typical response curve can be seen. The dotted lines are included to assist visual evaluation. The $\tau_{100\%}$ means the time needed to reach the total potential change. It has to be mentioned that the response time is unusually small, about 0.15-0.2 s. The experiment was repeated with antimony microelectrodes that have orders of magnitude less resistance, hence it was expected that their fast response is limited rather by the activity change (pH=4 and pH=10 buffers were used). Interestingly, the results (not shown) are very similar to the ones obtained here. Apparently, the activity step can be achieved in 0.15-0.2 s with this system. Although, the real response time could not be determined with this method, these experiments certified, that the response time of the Cu ISME is less than 0.15 s, a feature that is very advantageous in SECM experiments.

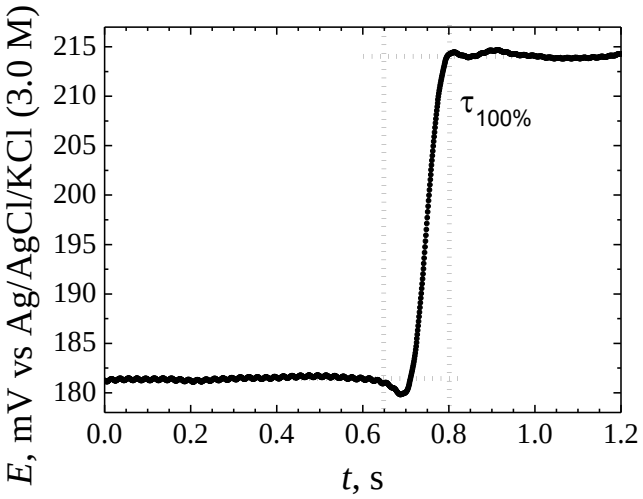

Fig 27. Dynamic response of the Cu ISME in the activity step experiment when 10^{-3} M $CuSO_4$ solution is replaced by 10^{-2} M $CuSO_4$.

Next, the applicability of the microelectrode in SECM measurements was tested. Two model experiments have been carried out after the calibration (see in **Fig 28**). In the first experiment, a 2 mm diameter corroding copper disc was used as Cu^{2+} ion source. In the **Fig 28A**, the Cu^{2+} ISME was used to image Cu^{2+} release as a consequence of the polarization of copper sample in 0.1 M KCl. A fix current of 1mA/cm^2 was applied for 1 minute. Immediately following the polarization, the micropipette was positioned over center of the sample at 50 μm height and scan along the circularly symmetric pattern was initiated from the center of the target. The figure nicely depicts the approximately three orders of magnitude change in the close vicinity of the polarized copper disc. The potentiostat remained switched off throughout the scan to avoid the occurrence of the electric field effect.

In the second experiment (see in **Fig 28B**) an iron disc (d=1 mm, similarly prepared as the copper sample) specimen was employed as Cu^{2+} sink in 10^{-2} M $CuSO_4$ solution. In the close proximity of the iron sample the local Cu^{2+} is reduced and its concentration is smaller than in the bulk solution.Therefore, while the probe passes over the iron disc, a potential decrease must occur. Indeed, after positioning the Cu^{2+} ISME over the iron disc specimen at 50 μm, 3 ml/s of 10^{-2} M $CuSO_4$ solution was added to the sample and after ten seconds of waiting time, significant decreases of the local Cu^{2+} concentration was observed above the iron specimen. These model experiments confirm the applicability of the Cu ISME in SECM studies of real samples and processes.

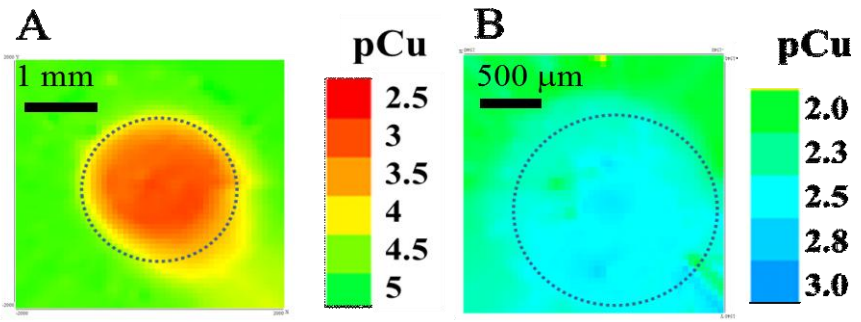

Fig 28. Potentiometric SECM experiments using the novel Cu(II) ion-selective microelectrode. A: Cu(II) concentration distribution above a copper wire immersed in 0.1 M KCl immediately after completing 1 min anodic polarization at 1 mA/cm^2. (B) Cu(II) concentration distribution above a Fe wire immersed in 0.01 M $CuSO_4$ solution. Spontaneous deposition of copper occurred over the iron wire resulting in the local depletion of Cu(II) concentration.

II.6.8. Examination of the "cross-talk" effect of the double-barrel electrodes

The first type of double-barrel electrode containing the Zn ISME and the antimony microelectrodes showed very similar behavior to the single microelectrodes in calibration, a fact considered promising regarding simultaneous detection might be possible in SECM experiments. In order to ascertain any eventual cross-talk effect between the individual barrels, line scans were carried above the Fe-Zn galvanic pair model under both individual and simultaneous operation. When the scan was made above the Zn anode, the dissolution of zinc was detected using the Zn ISME barrel of the assembly:

$$Zn \rightarrow Zn^{2+} + 2e^- \tag{53}$$

Fig 29A shows a direct comparison between the scan line recorded while only the Zn ISME was connected to the measurement equipment with that acquired by the Zn ISME while the antimony electrode was also connected to the voltmeter and recording an electrochemical signal. The lines were made above the Zn anode exposed to 0.001 M NaCl solution applying 25 μm/s scanning rate at 25 μm vertical distance between the tip and the sample. As it can be observed in **Fig 29A**, there is no significant difference between the two lines, which suggests the absence of the cross-talk effect.

On the other hand, the cathodic half-cell reaction taking place on the surface of the iron sample, causes a local pH increase in the adjacent solution:

$$O_2 + 2H_2 + 4e^- \rightarrow 4OH^- \tag{54}$$

The same experiment but with the antimony microelectrode can be seen in **Fig 29B**. In this case, the tip traveled throughout the center of the Fe sample. Analogously, the operation

of the Zn ISME does not seem to influence the measurements done with the Sb microelectrode.

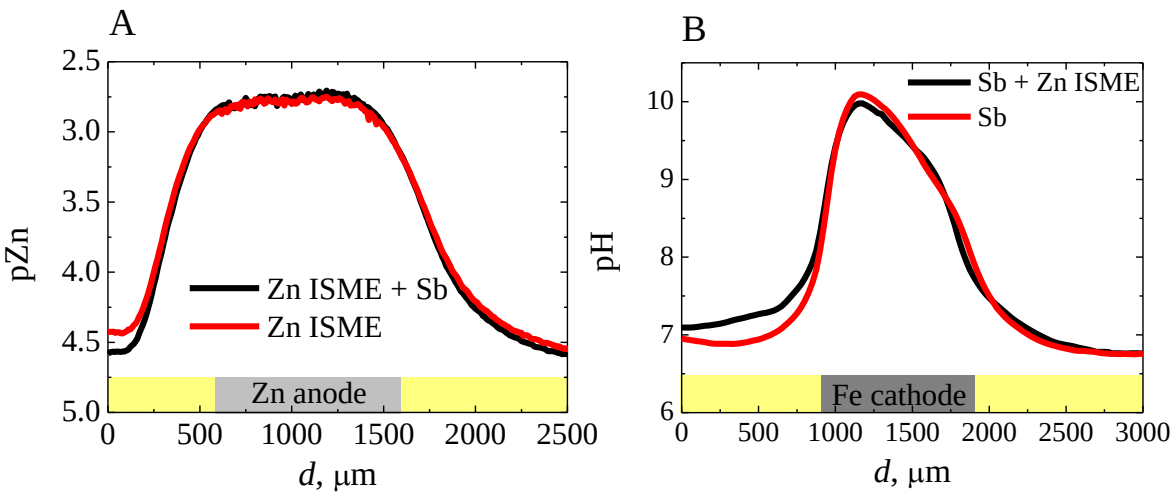

Fig 29. Comparison between the simultaneous and individual operation of the Zn ISME and the Sb electrode. **(A)** pZn line scans recorded over the Zn and **(B)** pH line scans above the Fe wires. The experiments were carried out in aqueous 0.001 M NaCl solution.

II.6.9.The possibility of enhanced selectivity obtained in simultaneous measurements

In certain cases, the corrosion of more than one metallic species proceeds; e.g. the parallel dissolution of copper and zinc. This is the case when it comes to brass corrosion. In alloy corrosion, the preferential dissolution of the more active metal is a well known effect. Hence the ratios of the Cu(II) and Zn(II) activities in the adjacent solution are different from the Zn/Cu ratio in the metal phase. This can be characterized by the so-called dezincification factor (*Z*) that is the quotient of the Zn/Cu concentration ratios in the solution and in the metal phase:

$$Z = \frac{[c_{Zn}/c_{Cu}]_{solution}}{[c_{Zn}/c_{Cu}]_{alloy}} \tag{55}$$

Dezincification can be an excellent application field for potentiometric SECM, hence it could be investigated locally instead of monitoring only an average value as it is the case using atomic absorption measurements of bulk concentrations, for instance. However, in such system, the selectivity of the microelectrodes has to be taken in to consideration. In a mixed solution containing Cu^{2+} and Zn^{2+} ions the potentials measured by the Zn ISME and the Cu ISME can be expressed using the Nicolsky-Eisenman equation, as follows:

$$E_{Zn} = E_{0,Zn} + S_{Zn}\log\left(a_{Zn} + k^{pot}_{Zn,Cu}a_{Cu}\right) \tag{56}$$

$$E_{Cu} = E_{0,Cu} + S_{Cu}\log\left(a_{Cu} + k_{Cu,Zn}^{pot} a_{Zn}\right) \tag{57}$$

where E_{Zn} and E_{Cu} are the corresponding measured potentials; $E_{0,Zn}$, $E_{0,Cu}$ include all the constant potential contributions measured; S_{Zn} and S_{Cu} are the slopes of the calibration plots for the Zn^{2+} and Cu^{2+} ISME's; a_{Zn}, a_{Cu} are the activities of Zn^{2+} and Cu^{2+}; and $k_{Zn,Cu}^{pot}, k_{Cu,Zn}^{pot}$ are the selectivity coefficients of the Zn^{2+} and Cu^{2+} ISME's, respectively. Assuming simultaneous measurements, all the variables are known in these two equations except for the activities. That is, we have two equations for two variables, thus two measured potential values are sufficient to determine the actual activities. Therefore the logarithmic activity of zinc(II)-ions can be written as:

$$a_{Zn} = 10^{(E_{Zn}-E_{0,Zn})/S_{Zn}} - k_{Zn,Cu}^{pot} a_{Cu} \tag{58}$$

Finally, expressing the Cu(II) activity:

$$a_{Cu} = \frac{10^{(E_{Cu}-E_{0,Cu})/S_{Cu}} - k_{Cu,Zn}^{pot} \cdot 10^{(E_{Zn}-E_{0,Zn})/S_{Zn}}}{1 - k_{Cu,Zn}^{pot} \cdot k_{Zn,Cu}^{pot}} \tag{59}$$

Fig 30 shows a set of simulated curves to illustrate the above mentioned calculations. The black curve is a Cu^{2+} distribution recorded above a Cu^{2+} ion source (although it is based on a real experiment, the peak was smoothed to obtain a symmetric shape for the sake of better illustration). Assuming the lack of any disturbance, the pCu curve is treated as the actual pCu distribution. The red curve shows the hypothetic measurement carried out with the Zn ISME above at the same point above the same Cu^{2+} source at a given time. The difference between the baselines is due to the different limit of detections for each microelectrode. The increase in the measured potential implies an apparent increase of the Zn^{2+} activity. In our theoretical example, the source only releases Cu^{2+} ions, hence the red curve can be seriously misinterpreted. Knowing the actual Cu^{2+} activities from the theoretical distribution and the selectivity coefficient of the Zn ISME for Cu(II) ions, the real Zn^{2+} distribution can be calculated (green curve), thus effectively reproducing the real situation where no increased Zn^{2+} activity can be observed above the Cu^{2+} source. It has to be mentioned that, this model is very simplified and more complex systems may require more measurement data to determine the exact activities of the species that are present. However this method can be utilized in the case of the SECM measurements of the dissolution of binary alloys using double-barrel microelectrodes.

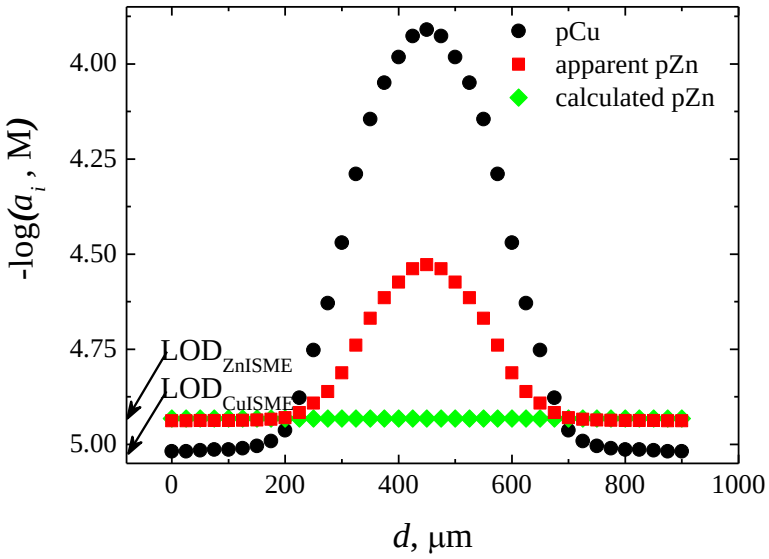

Fig 30. Simulated curves of a scan line measured above a Cu^{2+} ion source. (Black) the actual Cu(II) ion distribution, (red) incorrect pZn measurement due to the Cu^{2+} ion's contribution to the Zn ISME's signal. Calculated (green) correct Zn^{2+} distribution.

II.6.10. Establishment of the probe-sample distance in potentiometric SECM

In SECM measurements, the exact knowledge of the tip-sample distance is of major importance. Unless it is known, no quantitative information can be obtained from the measurements. In addition, accidental tip-sample crash can break the probe. When it comes to ion selective microelectrodes, tip positioning faces difficulties, since the feedback effect does not occur in the potentiometric mode and ISME's cannot be polarized. Hence, often the gentle approach method is used, which means a step by step approach of the tip towards the surface while the tip-sample distance is being observed with the aid of an optical microscope. Once the tip touches the sample one can set the desired tip sample distance in the computer and lift the tip up to that value. However, the fragile micropipette type electrodes can be easily broken while touching the surface.

An alternate procedure was proposed by Wei et al. in 1995 [143]. In that case, a double-barrel tip containing the ISME and an open micropipette containing a silve wire electric contact was applied. The open barrel actually looks and can act as a microreference electrode. When a constant, small dc voltage is applied between the open pipette and a conventional size reference electrode, a current can be observed. When the orifice of the micropipette is small, then the current determined by the ionic flux through the orifice of the micropipette. As the the tip approaches the surface the mass transport becomes eventually blocked and the resistance increases. Plotting the theoretical curves on experimental resistance vs. tip-sample distance curves, the exact distance can be calculated. However, the authors pointed out that

the sensitivity of this method is not sufficient in certain cases, because the tip resistance/solution resitance ratio should be kept very small.

The situation is far more easier, when the tip is the pH sensitive antimony electrode. Antimony microelectrodes can be operated in the amperometric mode, although they are seldomly used for conventional voltammetric purposes due to their very narrow electrochemical window. Nevertheless, in SECM only a narrow potential window may be sufficient, if there is a reaction of interest taking place in that potential range.

Wei et al. employed gallium microelectrodes to record *Z* approach curves exploiting the reduction of ruthenium hexammin chloride mediator [18]. In the early years of potentiometric SECM it was known that antimony microelectrodes could be used for O_2 detection [17]. **Fig 31A** depicts a DC voltammogram (negative direction) taken with 0.05 V/s scan rate in 0.1 M KCl solution using an Sb disc microelectrode. A well-defined peak can be observed at ca. -0.6 V vs Ag/AgCl/KCl (3.0 M) corresponding to the oxygen reduction.

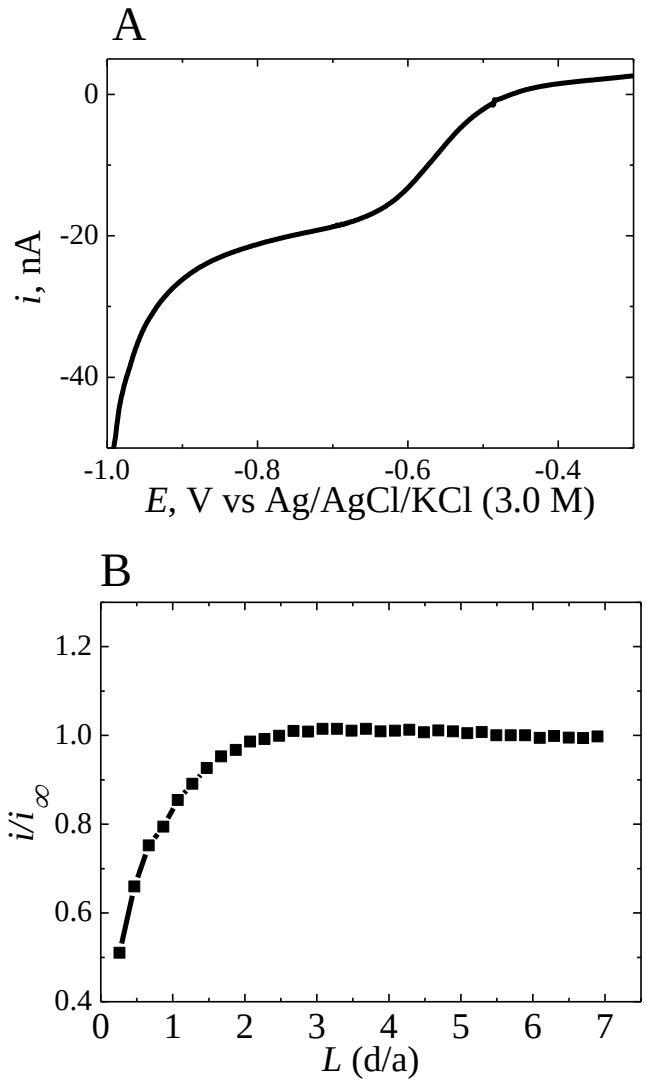

Fig 31. (A) Cathodic linear sweep voltammogram of the antimony microelectrode in 0.1 M KCl solution, and (B) *Z*-approach curve with E_{tip} = -0.7 V vs. REF.

This reaction was utilized to set the tip-sample distance in amperometric mode prior to the potentiometric pH mapping. In **Fig 31B** an approach curve is shown that was recorded with a 25 μm diameter antimony microelectrode biased at -0.7 V vs. Ag/AgCl/KCl (3.0 M) in 0.1 M KCl solution. The occurence of a feedback effect can be employed for tip positioning.

Therefore if the multibarrel tip contains a barrel with antimony microdisc electrode, then the sample-tip distance setting can be done easily. In my experiments, this feedback effect of amperometric oxygen reducig current measured with antimony microelectrode was used for tip setting, when it was needed e.g. in pH detecting SECM studies.

Part III. Results and Discussion

Chapter 1 - Double-barrel electrodes for SECM imaging of the corrosion of Zn- and Cu-based materials

III.1.1. Resume

Zinc is the 4th most commonly used metal, and it has been used for about 5000 years as the alloying component of brass. Nowadays it is employed in corrosion protection, but the application of Zn as anode material in batteries is also very important. Because of its practical importance, the investigation of zinc corrosion attracted high attention and research activity [144].

In the Experimental part, the advantage of the multi-barrel electrodes in precise tip positioning in potentiometric SECM experiments has been demonstrated. This chapter aims to present two additional benefits of these devices. First, the possibility of simultaneous detection of different ionic species can offer supplementary information on the system under study. The example of galvanized steel corrosion will plainly show how the additional information of the local pH can assist explaining the differences in Zn dissolution at different locations. Then, I will focus on the issue of insufficient selectivity. In fact, the reason of using fragile and slowly-responding potentiometric probes is their superior selectivity compared to amperometric tips. Employing multi-barrel electrodes, even better results can be obtained, especially in media containing interfering ions. Prior to this, a short section will be introduced on the transient potentiometric signals produced in the presence of interfering ions and the possible effects on SECM imaging. That will be shown using the well known nonactin-based NH_4^+ ISME. Afterwards, I will turn back to the Zn ISME and the consequences of the poor selectivity against Cu^{2+} that will be mitigated by using double- barrel electrodes containing Zn and Cu ISME's. Since the preparation and the application of the ionophore based Cu ISME is a novelty, first reported in this Dissertation, therefore some model experiments will be presented to demonstrate its performance in SECM measurements.

III.1.2. Simultaneous measurement of Zn^{2+} dissolution and pH distribution above the Zn-Fe galvanic pair

As it was demonstrated in the Experimental part, the double-barrel electrode containing the Zn ISME and the pH sensitive antimony microelectrode exhibits similar analytical performance as the corresponding single barrel ones. The first test of this dual probe in an SECM experiment was carried out above the Zn-Fe galvanic pair composed by 1 mm diameter Zn and Fe wires, separated ca. 5 mm from each other. The physical separation of this model sample allows the anodic and cathodic reactions to be investigated separately,

whereas chemical interactions of the corrosion products formed in the half-cell reactions can be neglected.

The anodic half-cell reaction is the dissolution of Zn^0:

$$Zn \rightarrow Zn^{2+} + 2e^- \tag{60}$$

whereas the cathodic half-cell reaction is the oxygen reduction from the electrolyte that takes place on the iron sample:

$$O_2 + 2H_2 + 4e^- \rightarrow 4OH^- \tag{61}$$

In the solution adjacent to the anode, the hydrolysis of Zn^{2+} also occurs accompanied by weak local acidification

$$Zn^{2+} + H_2O \rightleftarrows Zn(OH)^+ + H^+ \tag{62}$$

Obviously, the formation of insoluble $Zn(OH)_2$, ZnO or the complex anions $[Zn(OH)_3]^-$, $[Zn(OH)_4]^{2-}$ may occur, as well, depending on the pH of the solution.

As it can be seen, a few simple reactions are expected to occur, hence the galvanic pair seems an excellent choice to test the analytical performance of the new multi-electrode arrangement. In addition, galvanic connection accelerates the reactions at each electrode. On the other hand, some interfering effect of the electric field formed in the galvanic coupling emerges as it will be discussed in details in the next chapter. For this reason, the galvanic coupling was maintained for 30 min, and then it was ceased while the scans were actually recorded. 30 min seemed to be long enough to produce significant changes in the vicinity of the samples. Of course, diffusion had to be taken into account, thus a relatively high scanning rate was applied, namely 100 μm/s. To minimize the distortion caused by the high scanning rate, a polar scanning algorithm was applied, that was developed by our coworker András Kiss [136]. The scan was started from the center of the metal disk.

In **Fig 32** the images resulted by the simultaneous scans can be seen. The circular map was extrapolated to square shape by the displaying software. As it can be seen, the shape of the sample was nicely outlined by both the Zn^{2+} dissolution map (**Fig 32A**) and the accompanying pH change (**Fig 32B**). In **Fig 33A** no significant Zn^{2+} concentration variation was observed above the iron sample. It has to be noted, that when the scan was carried out during the galvanic coupling, an about 2 orders of magnitude change was observed. In **Fig 33A** only a negligible variation of potential can be detected above the sample, which can be attributed to pa otential shift of the microelectrode or the variation of Na^+ concentration and the pH above the iron sample. On the other hand, an about 1.5-2 pH change was observed using the antimony microelectrode barrel.

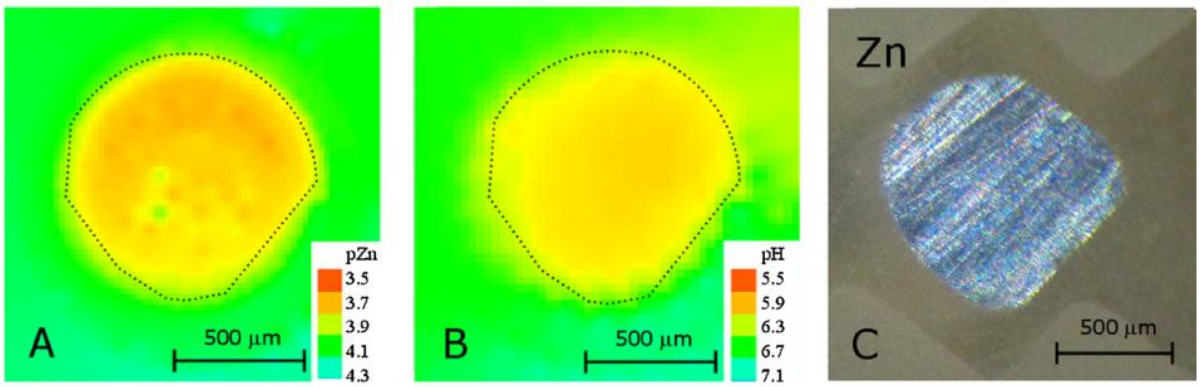

Fig 32. 2D simultaneous Zn^{2+} and pH imaging over the sacrificial anode of the Fe-Zn galvanic couple immersed in 1 mM NaCl. (**A**) Zn^{2+}distribution obtained with the Zn^{2+} ISME of the double-barrel probe; (**B**) pH distribution obtained with the Sb/Sb_2O_3 microelectrode of the double-barrel probe; (**C**) photograph of the Zn wire during the measurements.

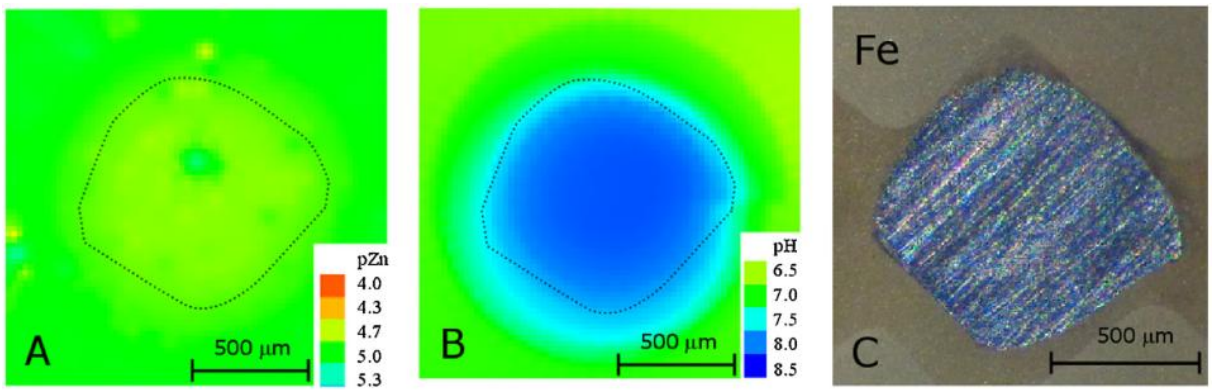

Fig 33. 2D simultaneous Zn^{2+} and pH imaging over the Fe cathode of the Fe-Zn galvanic couple immersed in 1 mM NaCl. (**A**) Zn^{2+}distribution obtained with the Zn^{2+} ISME of the double-barrel probe; (**B**) pH distribution obtained with the Sb/Sb_2O_3 microelectrode of the double-barrel probe; (**C**) photograph of the Fe wire end disc during the measurements.

III.1.3. Imaging the cut edge of galvanized steel

In the previous section, the applicability of the dual sensor in SECM investigation was tested. Here, an advantage of these arrangements is pointed out on the example of galvanized steel. Coil coated or painted-galvanized steel is widely used in automotive and building industries (i.e. as the structural material of green houses) due to their excellent corrosion resistance. However, scratches and cut edges expose steel to the corrosive environment and the low zinc-iron surface ratio in cut edges is not sufficient for satisfactory corrosion protection [56]. On the other hand, apart from sacrificial anodic protection, the corrosion products insulate the steel surface providing another protective mechanism [145]. The issue is complex and draws more attention in corrosion research.

In **Fig 34** a few line scans are depicted that were recorded simultaneously as the double-barrel probe travelled above the cross section of the galvanized steel sample. The step size was 50 µm, the vertical tip-substrate distance was 50 µm and the overall traveled length was 2000 µm at a scan rate of 50 µm/s. The lines were taken 100 µm apart as it is approximately shown in **Fig 34C,** and the colored lines in **A** and **B** correspond to the colored arrows in the micrograph. This means that the black lines in the pZn and pH curves were recorded simultaneously, likewise the red curves, etc. The black curve in Fig 34A shows that Zn^{2+} dissolution occurs on both sides of the specimen, yet the anodic activity on right side is decreasing from curve 1 (black with rectangles) to curve 6 (olive with triangles. This observation can be explained on the basis of the information provided by the corresponding pH scans. A small acidification is observed above the zinc layer located at the left side of the cut edge, whereas pH increases above the mild steel foil as result of the oxygen reduction reaction. This alkaline area is located closer to the right side of the cut edge, therefore the pH in the neighborhood of the right anodic area is increasing from pH = 7.3 to 8.1. The cyan, magenta and olive pZn lines on the right side also reveal some anodic activity, however the reaction product forms insoluble hydroxide that precipitates in the vicinity of the cathodic area.

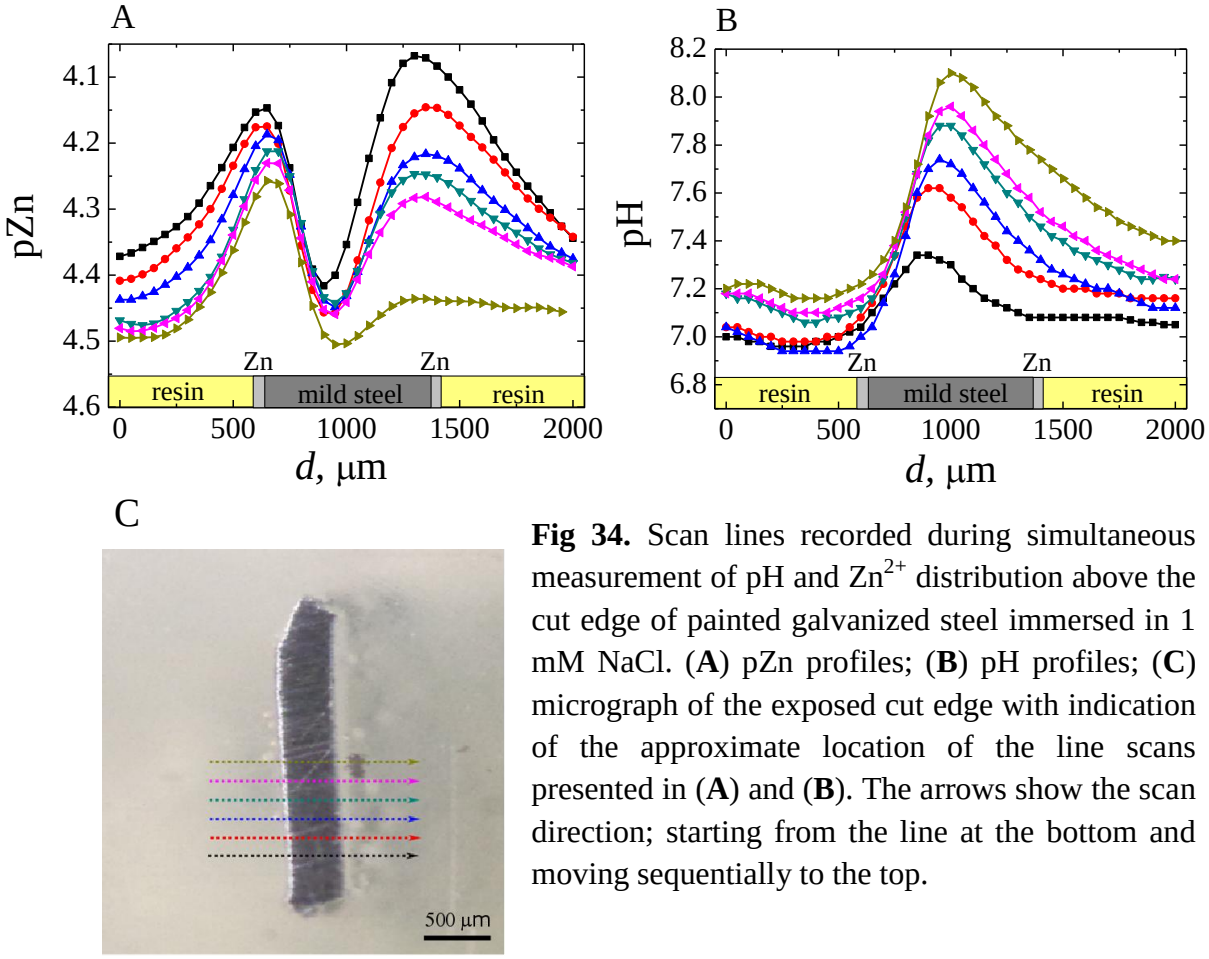

Fig 34. Scan lines recorded during simultaneous measurement of pH and Zn^{2+} distribution above the cut edge of painted galvanized steel immersed in 1 mM NaCl. (**A**) pZn profiles; (**B**) pH profiles; (**C**) micrograph of the exposed cut edge with indication of the approximate location of the line scans presented in (**A**) and (**B**). The arrows show the scan direction; starting from the line at the bottom and moving sequentially to the top.

Since the zinc ISME only detects dissolved Zn^{2+}, the observed decrease of the signal compared to the other side of the cut edge, where apparently constant anodic activity is

observed, can be attributed to the precipitation of corrosion products. This perception does not depend on the scanning direction. This is an interesting example of the complementary information supplied by the simultaneous measurement.

III.1.4. Transient signal of the ISME's

The prevailing endeavor in potentiometric SECM is the reduction of the measurement time. This is advantageous especially in corrosion research, since there is always a concern that the dynamically corroding systems may change during the scan time. Several approaches have been made to obtain reliable results in a relatively short time. However, an interesting feature of the potentiometric response in the presence of low levels of interfering ions was discovered and investigated in details in the late 70's and in the 80's [1]. Namely, that after an instantaneous activity step of the interfering ions, a rapid potential overshoot followed by a slow relaxation can be observed in the response curve. Such transient signal was also observed at concentrations at which the steady signal was hardly affected by the presence of interfering ions.

This effect has been investigated in the case of liquid membrane ion selective microelectrodes. To test the phenomenon, the well-known nonactin-based ammonium ISME was first used. Because of its notoriously poor selectivity towards K^+ ions, the ammonium ISME seems to be a good model for dynamic response measurements in the presence and the absence of interfering ions. The same activity step method was used as described in the experimental part. First, the microelectrode and the reference electrode were placed in the measurement vessel and it was filled with 1 mM NH_4Cl solution. After the stable potential reading was reached, a new volume of solution, with the same ammonium ion activity, but with 1 mM KCl was added and the signal was recorded with 1000 Hz sampling frequency. A initial sharp potential increase of ca. 20 mV can be seen in **Fig 35** followed by a slower relaxation decay. According to the potential values calculated using the Nikolsky equation, a 4.4 mV potential step should be observed. This could not be seen, however, the transient peak can be readily perceived. The peak „disappears" after ca. 0.4 s, that means, the equilibrating time in the local SECM measurements should be longer than that.

Afterwards, the vessel was washed with the solution containing only the primary ions, and the measurement was repeated except that the very same solution was added twice. In principle, the addition of the same solution should not cause any potential deviation, thus this was implemented only to detect any eventual discrepancies originating from the experimental system. Indeed, it was observed that the new injection did not cause the transient peak to appear, and only a very small potential change could be observed. Next, a potential fluctutation experienced before the addition of the fresh portion of solution was observed too. The concentration dependence of the transient peaks is demonstrated in **Fig 36.** The inset shows the linear relationship between the transient peak height and the logarithmic activity of the interfering ions.

The model experiments with ammonium selective microelectrodes in the presence of potassium interfering ions verified the original assumption of negative effect of transient

signals on potentiometric SECM measurements at fast scanning rate and low equilibration time. The duration of the transient signal is comparable to the usual equilibration time in SECM. In order to avoid the introduction of uncertainties in the interpretation of SECM experiments, these remarks need to be taken into account. Hence the thread sleep of homemade SECM equipment or the equilibrating time in the case of the Sensolytics equipment was fixed at 1 s.

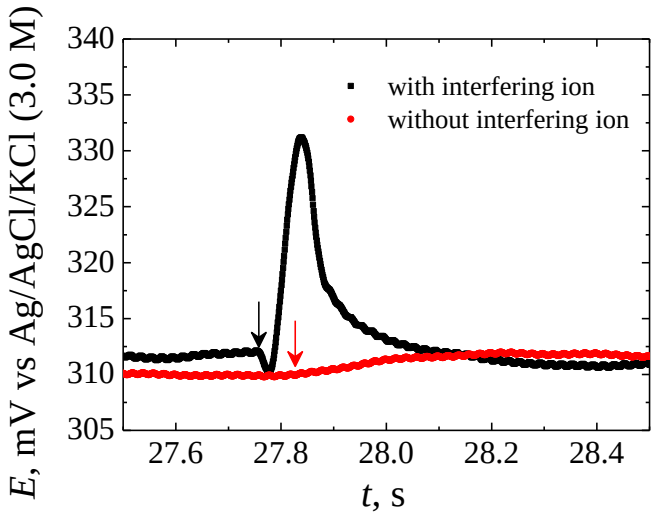

Fig 35. Dynamic response curves obtained after injection of a solution of plain 10^{-3} M NH_4Cl and a solution containing 10^{-3} M NH_4Cl + 10^{-3} M KCl. The arrows indicate the approximate time of the injection. The tube was filled with 10^{-3} M NH_4Cl solution prior to the injection.

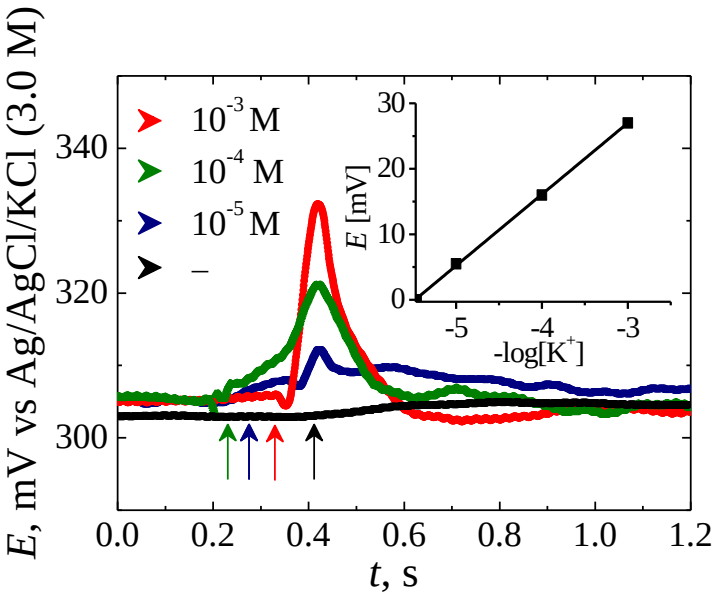

Fig 36. Response curves to changes in K^+ activity while the activity of NH_4^+ was kept constant at 10^{-3} M). The arrows indicate the approximate times of injections. The resulting concentrations of K^+ are labeled in the graph. The inset shows the dependence of the height of the transient signal height with log [K^+].

III.1.5. Simultaneous operation of the Zn and Cu ISME containing double barrel above Cu^{2+} and Zn^{2+} point sources

Ion selective microelectrodes have been proved as excellent SECM probes for about 2 decades. Evaluation of electrode potential data measured in SECM the investigation of corrosion of alloys however, where more ionic species of the base materials are formed and released, can be hard if the ISME has low selectivity for the other component of the alloy. It is known that dezincification is a characteristic phenomenon in the corrosion of brass. Since the Zn ISME is not entirely selective for zinc, the potential change caused by copper dissolution presumably contributes to the potential signal of the Zn ISME. Analogously, zinc dissolution will be also overestimated using a Cu ISME because of the interfering effect of copper dissolution. To overcome this limitation, a new method is proposed here that takes advantage of measuring with double-barrel ISME's. Evidently, the electrode potential of each ISME will be biased by the others analyte ion. To demonstrate this, model experiments were implemented using a sample containing copper(II) and zinc(II) ion point sources. Micropipettes were filled with 5% agar-agar gel saturated with the sulfate salt of the ion of interest. The scheme can be seen in **Fig 37**. The Zn ISME and Cu ISME containing double-barrel assembly was first scanned above the Cu^{2+} point source and the responses of the Zn ISME and Cu ISME were recorded simultaneously, and next, simultaneous measurements were conducted over the Zn^{2+} point source.

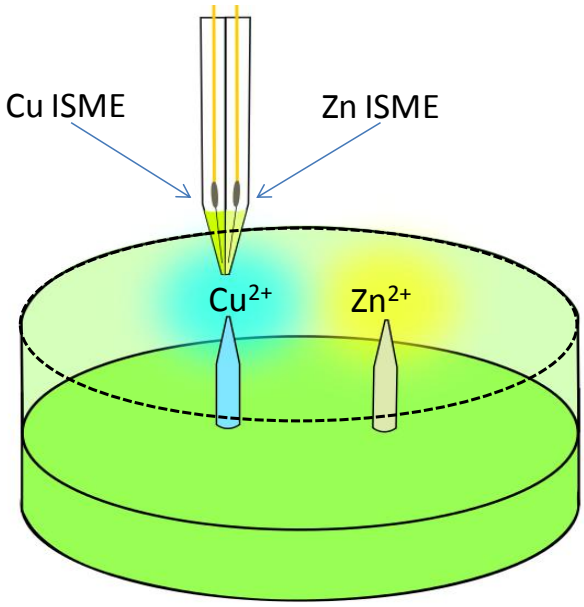

Fig 37. Schematic drawing of the simultaneous measurements performed over Cu^{2+} and Zn^{2+} point sources placed in ion exchanged water.

The results can be seen in **Fig 38.** In particular, maps (**A**) and (**B**) depict the measurement of the corresponding ion, that is, the response recorded above the Zn^{2+} source when it was scanned with the Zn ISME (**A**), and the response of the Cu ISME above the Cu^{2+} source (**B**).

It must be noted that during the recording of the maps (**A**) and (**B**) the other barrel in the double probe was also operating, that is, the potential of the Cu ISME was recorded during the scan performed above the Zn^{2+} ion source and viceversa. Actually, the results of those recordings can be seen in (**C**) and (**D**), respectively. In the case of the scan recorded with the Cu ISME above the Zn^{2+} ion source, only a small potential fluctuation of about ±1.5 mV versus the bulk level was observed. Since the measurement with the Zn ISME was performed above a Cu^{2+} source, there should not be any measurable potential deviance, so this can be assigned to noise in the measurement. In addition, about 7 mV potential change should be expected above the Cu^{2+} source using the Zn ISME according to the theoretical estimation. Indeed, in practice ca. 6.7 mV potential difference was measured compared to the bulk level.

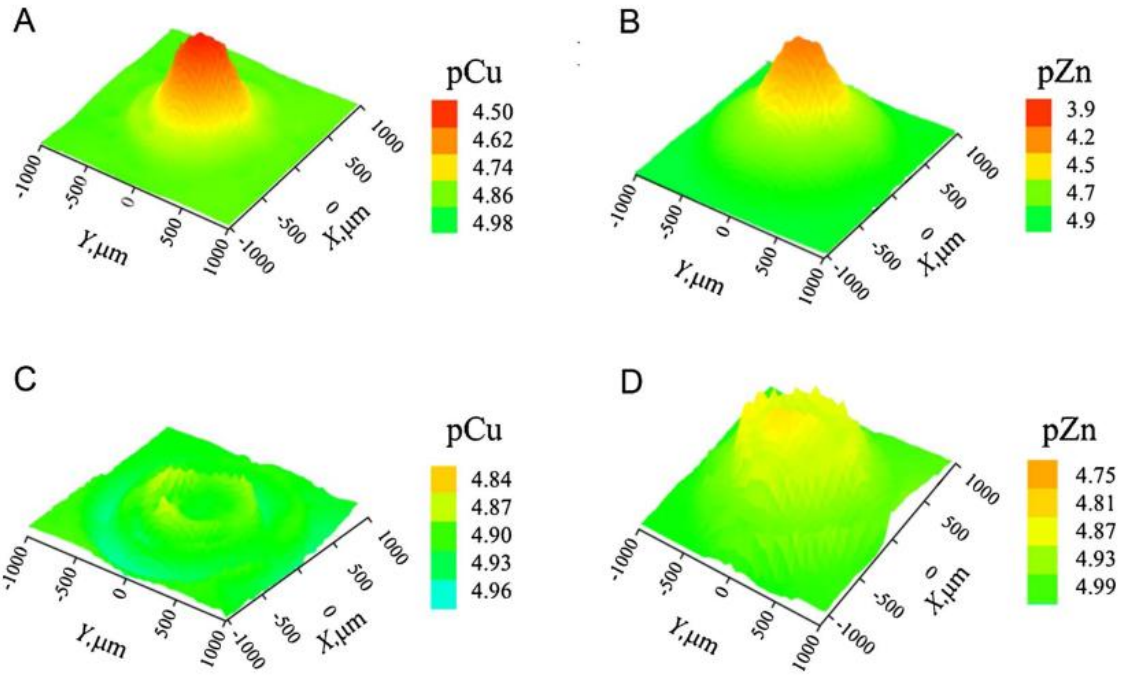

Fig 38. Simultaneous measurements over Cu^{2+} and Zn^{2+} ion sources obtained using the Zn/Cu ISME double-barrel assembly: (**A**) Cu ISME response over the Cu^{2+} ion source; (**B**) Zn ISME response over the Zn^{2+} ion source; (**C**) Zn ISME response over the Cu^{2+} ion source; (**D**) Zn ISME response over the Zn^{2+} ion source. The diameter of the source was 400 µm and the tip source distance was 100 µm.

Evaluation of **Fig 38** needs further consideration. In the case of measurements recorded using single-barrel electrodes above a complex sample such as a corroding brass specimen instead of the simple model Zn^{2+} and Cu^{2+} releasing sources considered here, , the above mentioned feature can lead to misinterpretations. Nevertheless, in the case of simultaneous measurements, we have two measured values for every location and two unknown concentrations.

It was shown, in the Experimental part, that knowing the selectivity coefficients of the ISME-s the electrode potential values measured with the electrodes of poor selectivity can be transformed to realistic Zn^{2+} and Cu^{2+} concentration values using Eq (56)-(59). Using this

evaluation method an attempt was made to improve the quality of Fig **38C** and **38D**. Accordingly, **Fig 39** shows both the experimental and the calculated Zn(II) distributions recorded above the Cu(II) source. Image A is obtained with using straight the *E*- log(a_{Zn}) calibration curve, without considering interfeering contribution of the Cu^{2+} ions, while image B is the corrected one. It can be seen that the peak in the center disappeared completely, and the Zn(II) values remain close to the bulk level over the copper source. However, in the edges of the sample the measured 0.25 orders of magnitude change in Zn (II) activity only decreased to 0.13 after data processing. The remaining difference arises from pattern differences in the simultaneously recorded pZn and pCu images. The "ring" around the sample seems to be some measurement error in the original figure which remains although to a lesser extent in the treated pZn map. Then, the central peak was reduced to the bulk level implying that a similar „geometry" of the pZn and pCu map would have resulted in a perfectly plain potential map.

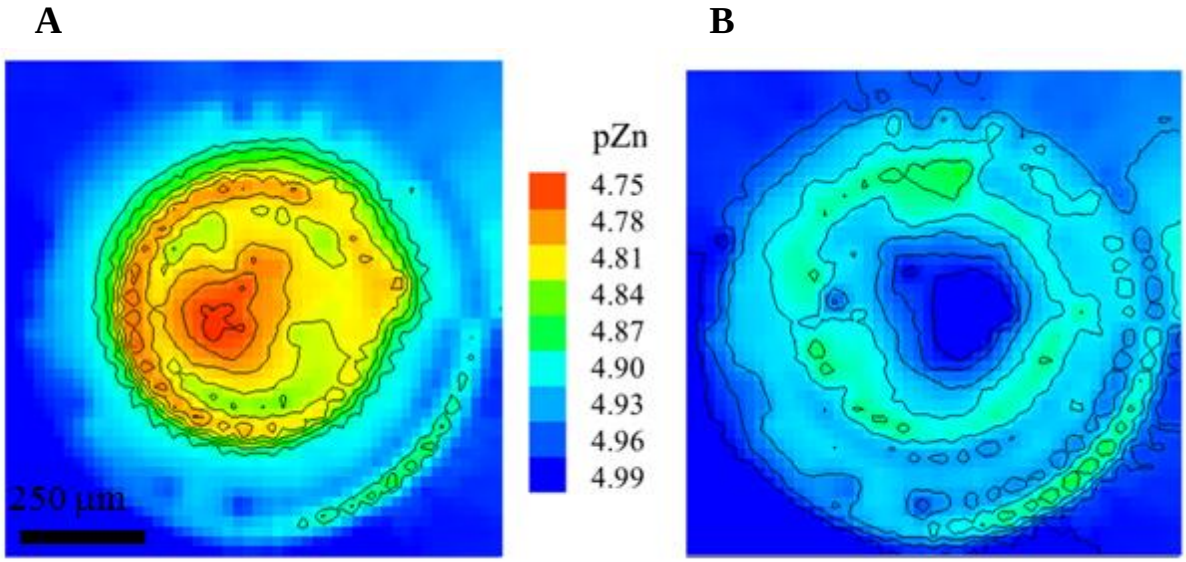

Fig 39. (A) Raw pZn map measured above the Cu^{2+} ion source with the Zn ISME in the double-barrel assembly; (B) calculated pZn map using correctionthe pCu data simultaneously obtained with the double-barrel assembly

Chapter 2 - Potentiometric SECM imaging of the galvanic corrosion of Mg

III.2.1. Resume

In the previous chapter, three advantages of the application of multi-barrel electrodes have been demonstrated. Firstly, safe and precise tip positioning of ion selective microelectrodes due to the dual function of the antimony electrode barrel. Secondly, the distributions of different ionic species can be recorded simultaneously. Then, it was shown that in the case of corroding alloys where simultaneous metal dissolution occurs, the interference of the different ionic species can be minimized using multi-barrel assembly. In experiments when the Zn ISME/Sb double-barrel electrode was scanned on a Zn-Fe galvanic couple sample, the scan was actually performed immediatly after the galvanic coupling was ceased to avoid the the contribution of electric field effects on the measured potentiometric signal. Indeed, when the couple was connected, unrealistically high Zn^{2+} dissolution rates were measured using the calibration curve. Similarly, over the Fe the electrodepotential would indicate Zn^{2+} depletion. Such decrease falled below the limit of detection of the ISME. In order to eliminate these undesirable features of the electric field associated to galvanic corrosion, the first procedure consisted in letting the galvanic corrosion to proceed for 30 min in order to develop the concentration distributions in solutions characteristic to galvanic corrosion, and then measuring with the ion selective tips above the disconnected metals, assuming that the concentration distribution will remain almost unchanged during the measurement. However, this is not completely true. Minimizing the measurement time by increasing the scanning rate does not solve the problem either. The fast probe movement stirs the solution causing distortion in the map. The circularly symmetric algorithm results in a circularly symmetric distortion in the image, implying an apparent uniformity in the anodic activity over the complete zinc surface. However, in a previous work of Ferreira and coworkers, it was demonstrated that although the whole iron surface is cathodically active in a Zn-Fe galvanic couple, the zinc surface does not present a homogeneous distribution of the anodic activity [146].

Obviously, if reliable information is to be extracted from the potentiometric imaging of galvanic corrosion reactions, *in situ* concentration measurements have to be carried out and the effect of electric field has to be eliminated. This chapter presents firstly the follow up of my collaborative work with András Kiss on the electric field problem [75]. Some factors that affect the magnitude of the electric field effects that are directly related to galvanic coupling will be demonstrated, and a new experimental arrangement for SECM able to avoid the unwanted contribution of the electric field will be presented. Secondly, the application of double- and triple-barrel electrodes will be presented for the characterization of galvanically corroding magnesium. In fact, this Dissertation turns toward magnesium corrosion from this chapter. For the characterization of the new multi-barrel assemblies, the Mg-Fe galvanic pair seemed to be an excellent model because the electric field effects are even bigger for this system.

III.2.2. Electric field effects on the potentiometric signal

Using amperometric probes, Mg^{2+} ions cannot be measured directly due to the high negative overvoltage of Mg^{2+} reduction. The supreme advantage of potentiometric SECM is the possibility of direct measurement of Mg^{2+} distribution [70,71].

However, some uncertainties have arisen in the quantitative evaluation of magnesium dissolution above galvanically corroding magnesium [72]. Unexpectedly low local pH values were monitored above defects of Mg-galvanized steel although they were justified invoking metal hydrolysis [73].

Fig 40A shows the scheme of the experiment aimed to investigate the uncertainties produced by the electric field on the potentiometric measurements. The sample contained 1 mm × 1 mm square shaped Mg (AZ63) and Fe specimens. Using the 3D positioning device of the SECM the microelectrode was positioned above the magnesium sample. The reference electrode was placed into the testing electrolyte (namely 1 mM NaCl) at a random position, as usual in almost all SECM measurements up to now. The iron and the magnesium samples could be connected electrically at the rear side of the mold. During the measurements, the potential of the microelectrode was measured against the randomly placed reference electrode and after a relatively stable potential value was achieved, the galvanic connection between the Mg alloy and Fe was established. A typical transient response is shown in **Fig 40B**. The arrows indicate the moments where the galvanic connection was established and ceased, respectively. As the result of the electric field, a rapid potential increase was observed after the galvanic cell was turned on, a change that cannot be explained in terms of the increased Mg dissolution rate, because it is impossible that the Mg^{2+} activity increases about 1.5 order of magnitude in less than a second and then produce a metal concentration that remains constant during the remaining time operating under galvanic coupling. That is, as it is drawn in **Fig 40A,** when the galvanic connection is established, not only magnesium dissolution occurs in the system but also an electric field develops as indicated by drawing some equipotential lines.

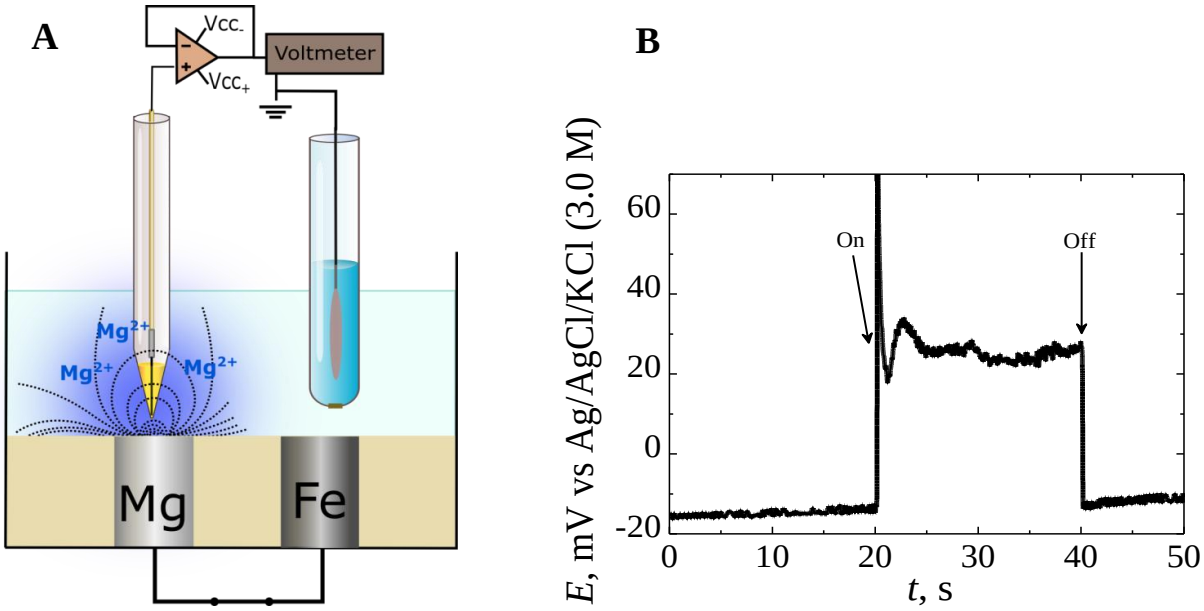

Fig 40. (**A)** Sketch of the experiment. The "blue cloud" represents the Mg^{2+} distribution over the corroding AZ63 sample. (**B)** Potential response of the Mg ISME. After 20 s, the AZ63 and the Fe samples were connected, and then disconnected again at time 40 s

In a subsequent experiment, the vertical distance dependence of this potential jump in the Mg ISME was studied. In **Fig 41**, the potential variation measured by the Mg ISME with time is shown for various tip-sample distances. Apparently, at 1000 μm distance, the electric field can still be sensed by the ISME, although at such high distances we lost almost all chemical information from the sample. It has to be mentioned that the apparent contradiction between **Fig 40** and **Fig 41** is the consequence of the randomly positioning of the reference electrode. Since the curves were recorded in independent experiments, there was no possibility to return the reference electrode to the same equipotential line. Hence the potential difference arising from the different location of the measuring and the reference electrode are almost the same, although the distance in in **Fig 40** was twice that in the black curve of **Fig 41.** Despite such limitation, it must be noted that the curves in each graph were recorded with the reference electrode at a fixed position of the bulk electrolyte, and therefore jumps measured in a given experiment could be directly compared, as in **Fig 41**. Another factor is the time and especially at small tip sample distances we can assume that the increased Mg dissolution changes the potential measured by the ISME. On the other hand, the potential difference between the galvanic couple varies in time, likewise in batteries. Based on all these, the extent of the bias caused by the electric field is hardly predictable.

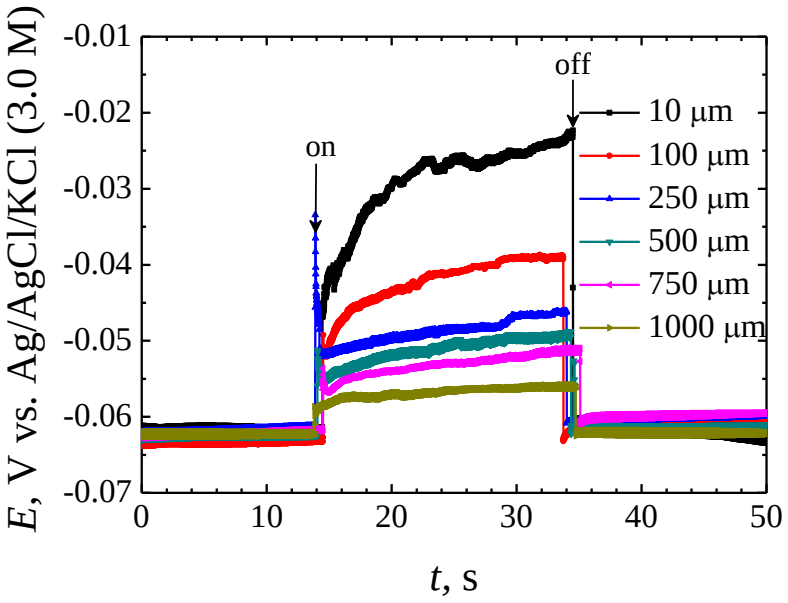

Fig 41. Effect of the distance between the ISME tip and the sample on the potential transients recorded by the Mg^{2+} ISME due to the galvanic coupling of the AZ63-Fe pair immersed in 0.001 M NaCl. The ISME was placed over the center of the AZ63 strip. Separation between AZ63 and Fe strips: 1.5 mm. The arrows indicate the times of electrical connection ("on") and disconnection ("off") of the two metals.

Another factor that affects the size of the "potential jump" is the electrolyte conductivity. Based on the Ohm's law, the higher is the electrolyte conductivity, the smaller the potential jump. This is demonstrated in **Fig 42** where the concentration of the electrolyte was varied between 10^{-4} and 10^{0} M in tenfold changes. For better comparison, the curves were shifted to the same starting point, thus the vertical axis shows the potential difference values with respect to the baseline. The inset shows the actual measurement data. As it can be seen, although the size of the potential jump decreases as the electrolyte concentration increases, the baseline is shifted towards the positive direction. This is the consequence of the insufficient selectivity of the ionophore towards sodium ions. If the baseline values were plotted against the logarithmic sodium ion concentration, the selectivity coefficient can be calculated, and it was found to be $\log K^{\mathrm{pot}}_{\mathrm{Mg,Na}} = -2.5$ in good agreement with the value reported in [147]. Again, the electrolyte conductivity is a factor we cannot make compromise with. As we minimize the electric field, the high interfering ion containing electrolyte overcomes the signal arising from magnesium corrosion. By contrast, in a dilute electrolyte, the electric field effect distorts our measurement.

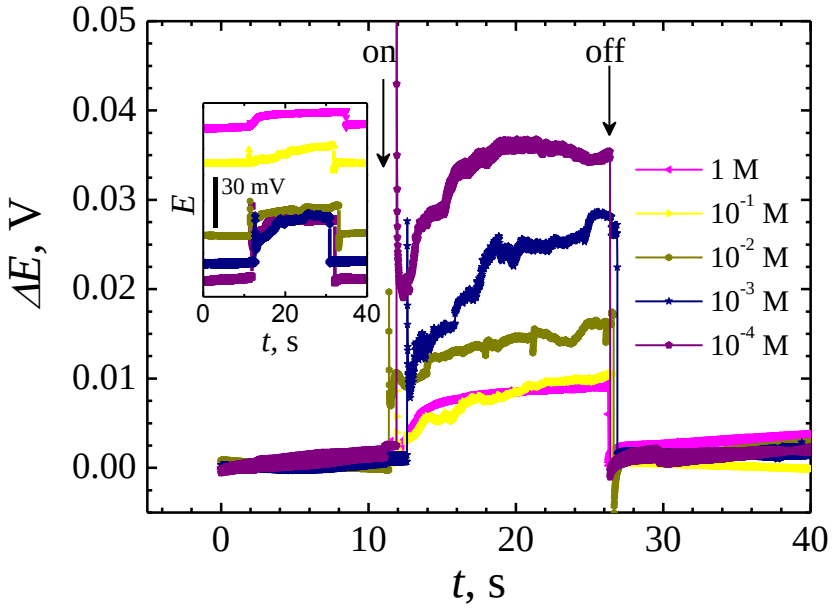

Fig 42. Effect of the electrolyte concentration on the potential transients recorded by the Mg^{2+} ISME due to the galvanic coupling of the AZ63-Fe pair immersed in NaCl. The ISME was placed over the center of the AZ63 strip. The curves were shifted along the potential axis for easier comparison, although the inset shows the original recordings. Separation between AZ63 and Fe strips: 1.5 mm; distance between the probe and the sample: 50 μm. The arrows indicate the times of electrical connection ("on") and disconnection ("off") of the two metals.

The distance between the anode and the cathode also have impact on the magnitude of the electric field effect. In principle, the closer the iron and the magnesium are, the smaller is the potential difference. Also differences in the potential jumps can be expected when magnesium is coupled with other metals. In order to demonstrate this, samples were prepared from 0.125 mm diameter metal wires (Al, Zn, Cu, Fe) and were separated approximately 6 mm from the Mg anode. **Table 8** summarizes the average potential jumps recorded after the galvanic coupling was established for each system. The magnitude of the electric field effect follows the expectations based on the electrochemical series of metals, namely the higher the difference of standard redox potentials between the two metals the higher is the potential jump. On the other hand, the reaction rate on the surface also has and impact on the field potential, that is why the passivated aluminum in the Mg-Al apparently contradicts the E_0 values.

Table 7. Potential jumps in case of different metals coupled with magnesium.

Galvanic pair	Potential jump caused by electric coupling (ΔE/mV)
Mg-Zn	2
Mg-Al	4
Mg-Fe	6.5
Mg-Cu	10

Yet, the most important factor influencing the electric field effect is the distance between the reference and the measuring electrode. The potential measured between the ISME and the reference electrode consists of the following terms:

$$\Delta E = \left(E_{\mathrm{M}} - E_{\mathrm{R}}\right) + \left(\varphi_{\mathrm{M}} - \varphi_{\mathrm{R}}\right) \tag{63}$$

where ΔE is the measured potential difference, E_{M} and E_{R} are the potential of the measuring and reference electrode, respectively, and φ_{M} and φ_{R} are the local potentials in the electrical field at the measuring and reference electrodes. The first term is the Nernstian response; the second term is the field potential difference, an unwanted component of the cell voltage originating from the different potentials detected by the electrodes in different places. For the sake of comparative purposes, a miniature Ag/AgCl reference electrode was prepared for controlled positioning in the small electrochemical cell. Fixing it to the SECM tip holder, the distance between the potentiometric electrode pairs accurately could be set. Experiments recording the cell voltage in time between the Mg and micro reference electrodes set by different distances were done while switching on and off the galvanic connection between the two embedded metals. As it is shown in **Fig 43**, the potential jump plateaus decrease with the decrease of the distance between the reference electrode and the Mg ISME because the electric field potential difference ($\Delta\varphi=\varphi_{\mathrm{M}}-\varphi_{\mathrm{R}}$) decreases. The inset shows the same curve (black line) already displayed in **Fig 40B**, where the reference electrode was located ca. 12 mm from the measuring electrode. On the other hand, the red curve was recorded when the miniature reference electrode was positioned as close as possible to the tip of the ISME. The potential jump did not occur this time, however the increase of the Mg^{2+} level in the adjacent solution could be measured well.

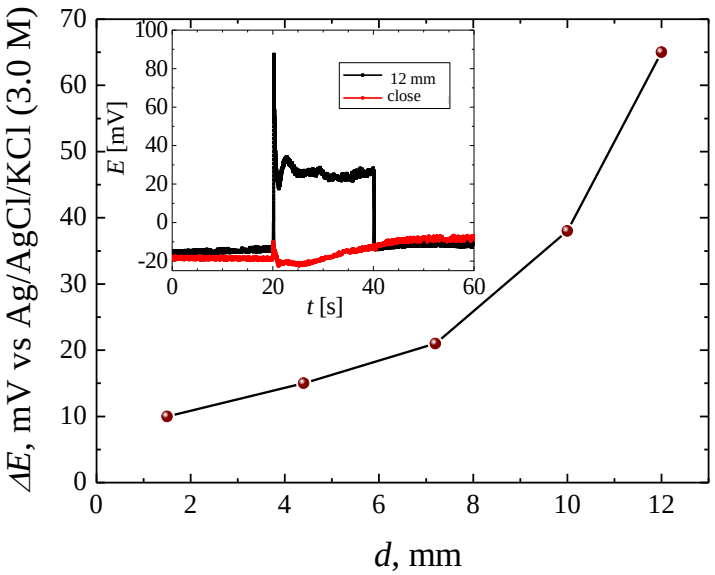

Fig 43. Effect of the separation between the ISME and the reference electrode on the potential transients recorded by the Mg^{2+} ISME due to the galvanic coupling of the AZ63-Fe pair immersed in 0.001 M NaCl. The ISME was placed over the center of the AZ63 strip.

Separation between AZ63 and Fe strips: 1.5 mm; distance between the probe and the sample: 50 µm. The inset shows the potential transients recorded for the distances between the two electrodes indicated in the graph.

III.2.3. Elimination of the electric field effects using double-barrel electrodes

After the successful preparation of double-barrel electrodes containing the Mg ISME and a microreference electrode (see the Experimental part for details), line scans were recorded 20 µm above the AZ63-Fe galvanic pair. **Fig 44A** shows the scheme of the experimental setup. For the sake of comparative purposes between the performances of the double-barrel arrangement and of the single-barrel electrodes, two consecutive line scans were recorded crossing above the connected galvanic couple, where firstly the potential of the Mg ISME barrel was measured against the internal microreference electrode (Ref 2), and then against the conventional reference electrode (Ref 1). In **Fig 44B**, typical line scans are presented. The black line in the figure indicates the limit of detection of the Mg ISME. The red curve jumped about 34 mV above the blue curve, yet it is transferred to the same starting point for an easier comparison. As it can be seen, the red curve shows an apparent non-zero Mg^{2+} concentration above the iron sample and the potential decreases well below the limit of detection. It is clearly the result of the negative polarization of the iron. This discrepancy with the calibration curve does not occur in the case of the blue line where the potential of the Mg ISME was measured against the internal microreference electrode.

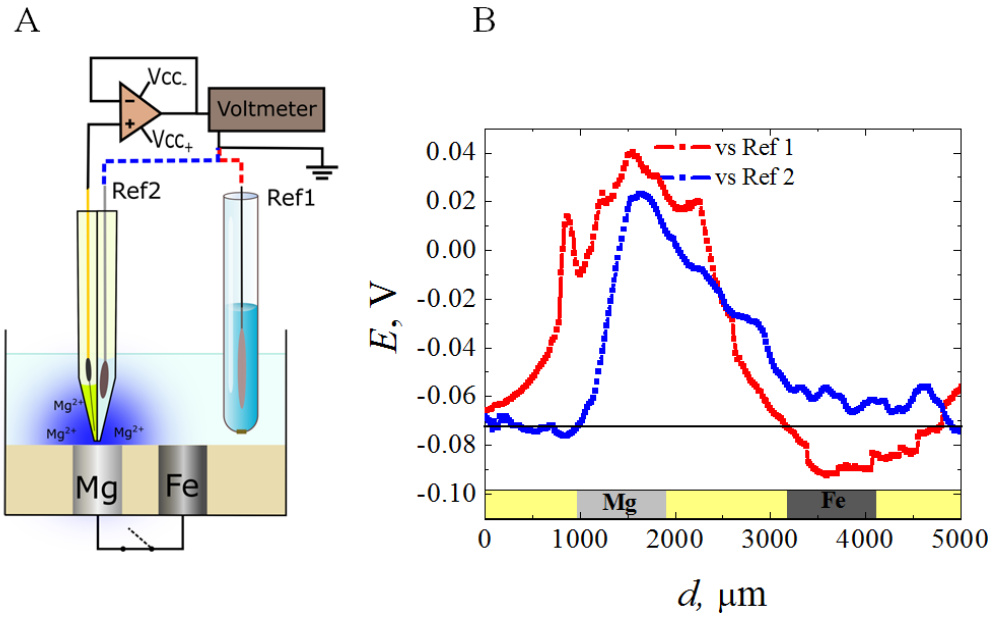

Fig 44. (**A**) Scheme of the experimental setup for the measurement of line scans s above the galvanic AZ63-Fe couple in 1 mM NaCl. (**B**) Line scans obtained using the doublebarrel microelectrode containing the Mg ISME. Potential data were recorded versus either the conventional reference electrode or that inside the doublebarrel assembly. The tip sample distance was 20 µm, scanning rate: 20 µm/s.

Another interesting feature was observed when this experiment was repeated using the pH sensitive Sb microelectrode/microreference electrode double-barrel assembly. In **Fig 45**, the two line scans show the opposite direction for the pH change above the galvanically connected magnesium. In the first case (black line), the potential was measured against the microreference electrode built in the double-barrel body, while in the second case (blue line), a conventional reference electrode was used separated about 1-1.5 cm from the tip. When the potential of the Sb microelectrode was measured against the microreference electrode (i.e., blue line), the bulk showed nearly neutral, slightly alkaline pH. This outcome may be regarded to be acceptable after about 1 hour exposure, due to solution agitation as result of hydrogen evolution, thus causing alkalization caused by the hydrogen reduction reaction to spread beyond the limits of the corroding metal sample itself. Above the magnesium, an about 1 pH unit change can be observed, with a slight decrease in the middle, which can be the consequence of the magnesium ion hydrolysis above a local anodic site. Afterwards, as the tip leaves the area of Mg, the pH goes nicely back to the background value. However, when the conventional reference electrode was used instead, very different changes were recorded. First, the bulk shows about pH=5.3 level, which might arise from the shifted potential due to the electric field developed in the system. Then, the pH goes down to 4.75, which does not seem physically reliable as shown next. The anodic dissolution of magnesium and the following hydrolysis can be written as in Eq (64) and (65):

$$Mg \rightarrow Mg^{2+} + 2e^{-} \tag{64}$$

$$Mg^{2+} + nH_2O = [Mg(OH)_n]^{(2-n)+} + nH^{+} \tag{65}$$

Then metal hydrolysis can be described by the following equation (if n=2):

$$pK_{HYD} = 2pH + \log [Mg^{2+}] \tag{66}$$

Regarding the hydrolysis constant of Eq (65), pK_{HYD}=11.4 [148], in the case of a 1 M concentration of Mg^{2+} in the adjacent solution to the galvanically corroding magnesium (which is a possible value, as it will be shown later), the pH cannot be lower than 5.7. After reaching the very unlikely value of pH 4.75, the pH measured by the antimony microelectrode returns to the values measured on the other side of sample, although an artifact still shows up around X = 2400 μm.

In summary, **Fig 44** and **45** show two different instances of the electric field effect. In the first case, the Nernstian response and the electric field have both positive contributions to the measured potential. On the other hand, the local alkalinization caused by the hydrogen evolution on Mg results in potential decrease, whereas the electric field above the Mg anode contributes positively to the measured potential. In **Fig 45**, the electric field contribution is so large that it suppresses the potential change cause by the actual chemical reaction, hence one would misinterpret the processes going on the surface of the magnesium anode. This demonstrates the superior applicability of the multi-barrel microelectrodes in the SECM imaging of the galvanic corrosion of magnesium.

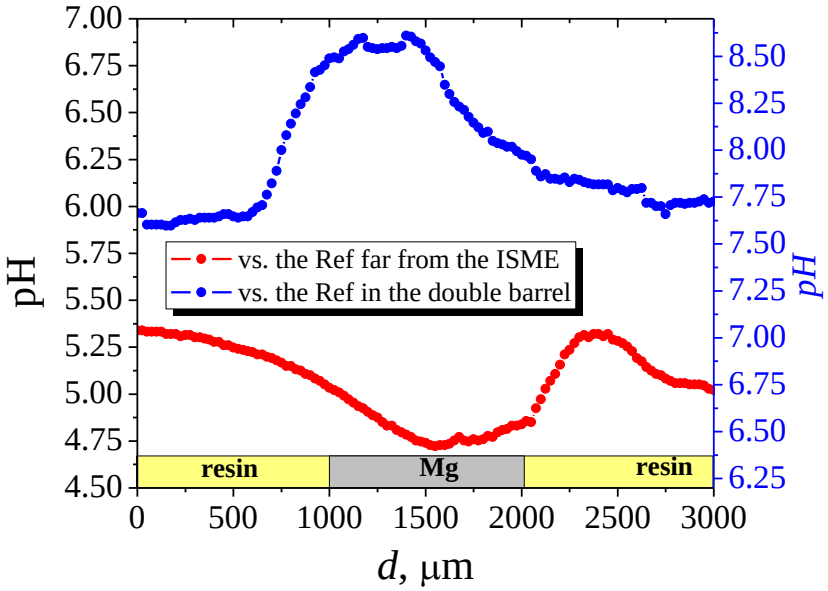

Fig 45. pH line scans recorded above the anode of the galvanically connected AZ63-Fe pair using an Sb microelectrode. Blue curve: using the conventional reference electrode. Black curve: using the microreference electrode in the double barreled electrode body.

III.2.4. SECM imaging of the corrosion reactions of magnesium

The above mentioned difficulties for SECM imaging of either galvanic corrosion or polarized samples appear to be minimized using the double-barrel assembly. In the next step, the pH and pMg distribution were recorded above magnesium samples (**Fig 46**). In spontaneous corrosion, the solution adjacent to the sample show local alkalization in a more or less balanced extent. Hence, using the usual display, the sample area appeares as a big blue spot. On the other hand, the magnesium dissolution could be detected to be of a localized type.

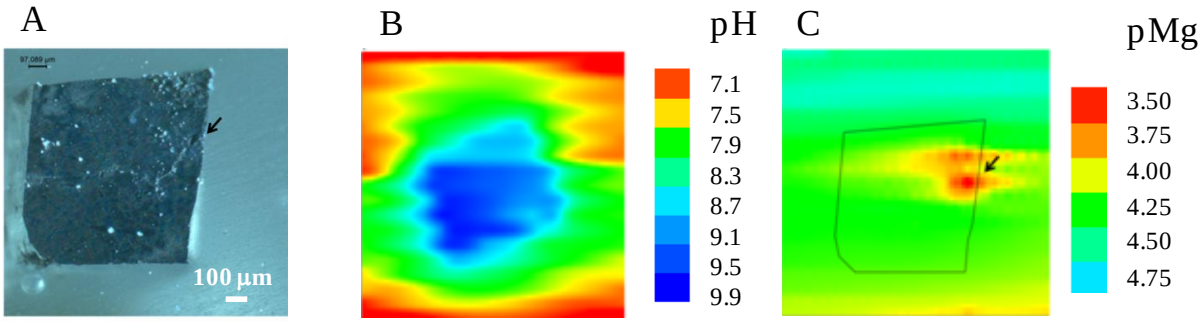

Fig 46. (**A**) Photograph, (**B**) pH and (**C**) pMg maps recorded over the spontaneously corroding magnesium alloy in 1 mM NaCl. Scanned areas are 2000 µm × 2000 µm, scanning rate 20 µm/s, tip sample distance 50 µm, resolution 100 µm.

In **Fig 47B**, a pH map recorded above the magnesium galvanically connected to an iron square sample is presented. For minimizing the previously described biases arising from the inadequate arrangement of the electrodes, a double-barrel antimony microelectrode containing the microreference electrode was used. In the proximity of the relatively large area of the sample, alkalization could be measured, with similar extent as in spontaneous corrosion. It has to be noted, that the magnesium dissolution is expected to be faster, as well, causing slight acidification, thus the measured values supposedly are the sum of the two opposite trends. On the other hand, the regions located at the bottom display an anodic character as it is confirmed by the micrograph in **Fig 47A**). That is, around the same area intense formation of corrosion products can be observed. This feature could not be distinguished in the case of spontaneous corrosion, because the cathodic reaction canceled the acidification from the anodic sites. Here, enhanced magnesium dissolution can be seen accompanied by local acidification, which apparently emerge from the generally alkaline pH map of the sample. It has to mentioned, that the acidification does not exceed pH=6.4, which is in agreement with the previously described considerations of the lowest possible pH.

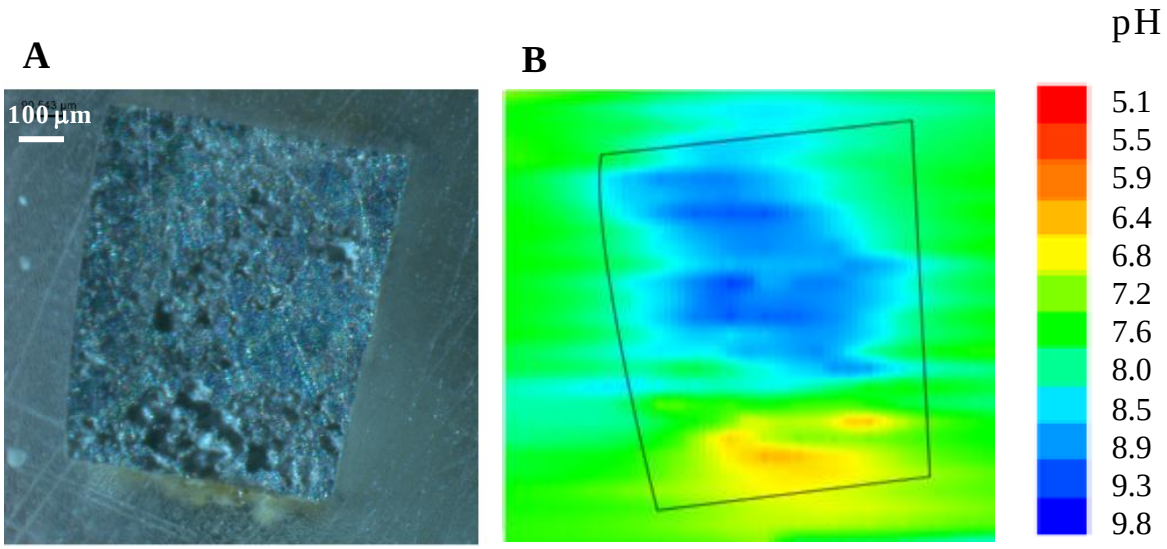

Fig 47. Localized pH measurements above a galvanically corroding AZ63 sample in 1 mM NaCl. **(A)**: micrograph, **(B)** pH map. Scanned areas are 2000 µm × 2000 µm, scanning rate 20 µm/s, tip sample distance 50 µm, resolution 100 µm.

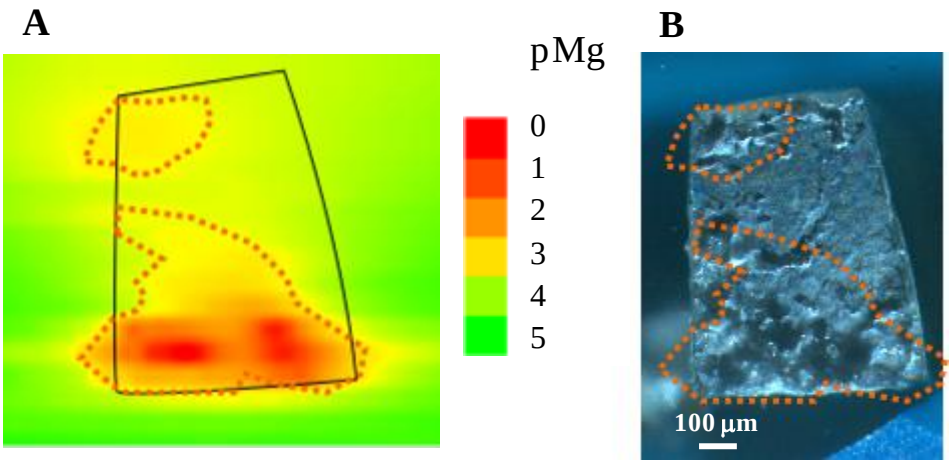

Fig 48. Localized pMg measurements above the galvanically corroding AZ63 in 1 mM NaCl. (**A)**: pMg map, (**B)**: micrograph. Scanned areas are 2000µm x2000µm, scanning rate 20 µm/s, tip sample distance 20 µm, resolution 100 µm.

The experiment was next repeated using the MgISME-microreference double-barrel electrode. The 2D scan was performed above a freshly prepared sample. The resulting pMg map with the corresponding micrograph are shown in **Fig 48**. The approximate position of the sample is depicted by drawing the contour of the sample. Above the resin pMg values close to the limit of detection could be measured. In the vicinity of the lower edge of the sample a huge, more than 4 orders of magnitude change of Mg^{2+} concentration, was detected, and the lowest pMg value measured above the sample is even lower than pMg=3. This increase of the local Mg^{2+} ion concentration is the consequence of enhanced magnesium dissolution due to the galvanic coupling. This accelerated dissolution is confirmed by the micrograph, where metal degradation shows very similar patterns to those found in the pMg map. The big triangle-shaped area at the bottom present various cavities on the photo, and high Mg^{2+} levels can be found in the lower part of the sample marked out with dashed orange line. In the top left area an additional region exhibiting enhanced anodic activity can be observed at the top left in both the micrograph and the pMg map. The only exception with an apparent contradiction can be found in the right top corner of the sample, where in the micrograph a relatively large cavity appears, whereas the pMg map does not show any significant electrochemical activity there. This can be explained by the low time resolution of the map. The scan was started from the left bottom corner of the image. The above-mentioned area formed possibly during the first stages of the scan time and eventually lost its anodic activity by the time the tip reached that area. Indeed, one has to make a compromise between fast scan rates and higher spatial resolution when it comes to potentiometric SECM. Nevertheless, this map represents a significant advance compared to those obtained using single-barrel electrodes, where only one big red spot well out of the linearity range of the ISME could be seen, as it has been reported in [74].

Finally, in **Fig 49** linear pH and pMg scans are presented that were measured using a triple-barrel measuring tip containing Mg ISME, antimony and microreference barrels. The

line scans were done by crossing the tip above the Mg surface in 1 mM NaCl solution. Galvanic connection between the AZ63 and iron was established throughout the measurements. For easier interpretation, pMg values are presented in a reversed scale, thus maxima and minima represent high and low Mg^{2+} activities, respectively.

In **Fig 49A** a relatively high peak can be observed above the magnesium surface on the right side of the sample. Above the resin, close to the surface, high pMg levels could be measured, as well. This is in agreement with the results shown in **Fig 48**. The increased rate of anodic dissolution facilitates corrosion sites to spread more widely compared to what happens during spontaneous corrosion. However, for the sake of better spatial resolution while keeping acceptably short measurement duration, the traveling distance along the *X* axis was not increased. We saw in **Fig 48**, that in situ detection of a significant anodic area was missed due to this fact. The pH decreases where the pMg value can be found, which corresponds to the hydrolysis reaction of Mg^{2+} accompanied by H^{+} generation. On the right side of the sample, a minor alkalization can be observed, and the Mg^{2+} activity decreases to the bulk level. The small minimum around 1200 μm corresponds to the locally more alkaline solution.

In **Fig 49B** the scan starts from pMg≈4, which is about 1 order of magnitude higher than the limit of detection. This can be explained by the increased rate of the magnesium dissolution and the diffusion of Mg^{2+} spreading into the surrounding resin areas. This is confirmed by the pH values, because for the enhanced hydrogen evolution, the pH above the resin is also higher than one would anticipate. Moreover, due to the solubility product of magnesium we cannot be sure about the actual magnesium activity, because the alkaline environment confines the amount of the dissolved Mg^{2+}. Therefore only a small increase could be observed (approximately 0.4-0.5 pMg value change) when the tip reached the magnesium surface, which decreased to the LOD value as the pH increased to 10 for $X \approx 1250$ μm. However, this pH value should not cause this large decrease of the dissolved Mg^{2+} activity, hence we can assume decreased activity in the anodic dissolution, whereas an increased activity of the H_2 evolution occurred. This demonstrates the findings by Williams et al. that previously anodic regions easily evolve into local cathodes [94]. The cathodic activation of former anodes occurs even under anodic polarization, which was usually invoked to explain the anomalous hydrogen evolution on anodically polarized magnesium surface [149]. Finally, above the resin both the pMg and pH values approaching their corresponding bulk values recorded above the resin at the opposite side.

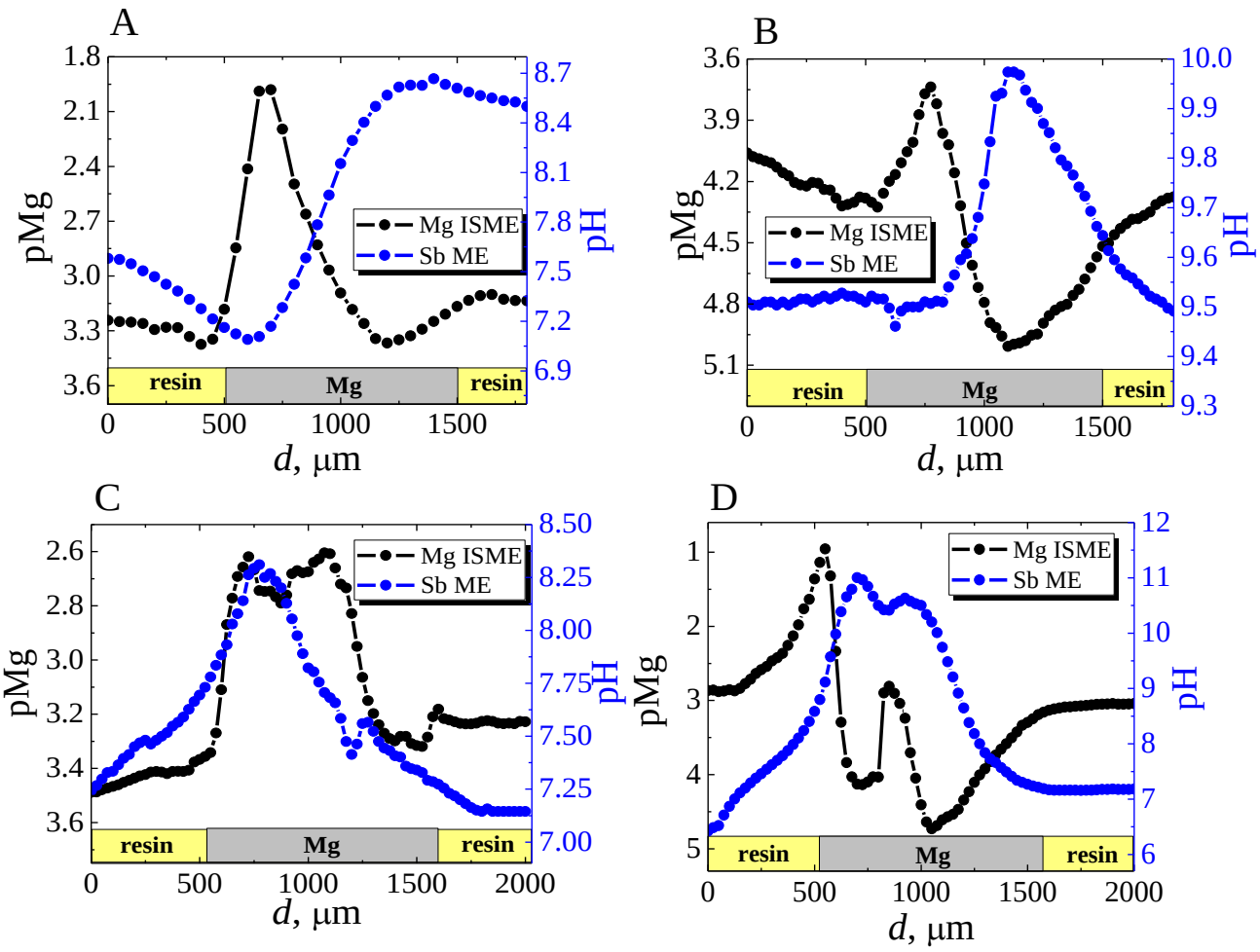

Fig 49. Four different pH-pMg line scan pairs measured using the triple-barrel electrode above the galvanically corroding Mg AZ63 alloy in 1 mM NaCl. Scanning rate 25 µm/s, tip sample distance 20 µm, resolution 50 µm.

Fig 49C represents another case where the pH and the Mg^{2+} activity increase together above the magnesium. This is an apparent contradiction to the behaviors displayed in Fig 49A and 49B, although there is no basis for comparison since this is the first experiment where pH and pMg are monitored simultaneously above galvanically corroding magnesium. However, the extent of the pH increase and its maximum values are not in contradiction with the pMg values. It seems that the anodic and cathodic sites are occasionally very close to each other. Besides, the local pMg minimum at the center of the Mg sample suggests that there are two anodic sites on the edges of the sample, whereas a site with increased hydrogen evolution activity was in the center. The maximum of the pH and the pMg minimum coincide well, which confirms the previous assumption. However, the hydrogen source in the center is not developed enough to change the pH above the resin significantly, although the vigorous magnesium dissolution results in relatively high pMg values extending even above the surrounding resin.

In **Fig 49D** another intriguing pair of pMg-pH profiles is shown. On the left edge of the magnesium sample, the highest increase of magnesium ion activity measured so far occurred with an abrupt decrease of 3 orders of magnitude around 600 μm. No wonder, since the pH reaches its own "record" in alkalization with a maximum around pH=11. In the case of such alkaline solution, the dissolved Mg^{2+} level does not exceed ~10^{-5} M. Indeed the pMg value rapidly falls back close to the limit of detection of the Mg ISME barrel. Then a local minimum in the pH line accompanied by a local maximum in the Mg^{2+} activity can be observed. It has to be noted that the pH value contradicts the measured amount of Mg^{2+}. A possible explanation is that the pH reaches a second maximum after this local minimum and the actual pH value in the minimum possibly could not be reached due to the short equilibration time. This was the case previously with the pMg minimum at 600 μm. Though the pH values suggest a pMg value around 5, the Mg ISME barrel traveled further, close to another local anode around 850 μm, which counteracted the decrease due to the alkaline environment. However, at the second pH maximum, the pMg value reached the LOD of the Mg ISME, since the second pMg maximum is only 3 and the change is less than in the first case, where the minimum should have been reached for pMg=1. After these second peaks observed by the Mg ISME barrel and antimony ME barrel, the pMg and pH levels off for relaxation of the two signals towards the bulk levels.

Chapter 3 - Investigation of hydrogen evolution on anodically polarized magnesium

III.3.1. Resume

A combination of beneficial properties makes magnesium and its alloys very attractive to the automotive industry. However, the rapid corrosion of magnesium severely limits its wide-spread application. The investigation of magnesium corrosion is of great interest to corrosion scientists in order to elucidate its mechanism and design methods of protection. One of the hottest topics nowadays is the explanation of the increased rate of hydrogen formation on anodically polarized magnesium (often referred as negative difference effect, NDE). The literature is extense on the topic, yet no consensus has been reached so far. The currently prevailing theories on the matter either invoke the catalytic properties of the $Mg(OH)_2$/MgO bilayer or emphasize the role of the noble impurities on the surface. If it were the first case, the following experimental findings should show up in fine studies of the process:

1. The rate of the hydrogen evolution reaction (HER) would be enhanced after the formation of the $Mg(OH)_2$ layer.
2. The rate of HER would be enhanced if the electrolyte contains Mg^{2+} ions so that the formation of the $Mg(OH)_2$ layer were favored.
3. Either removal or hindered formation of the $Mg(OH)_2$ layer will decrease the rate of HER.
4. Higher cathodic activity would occur from the $Mg(OH)_2$-covered surface as the potential of the metal were polarized to a more positive potential.

The experiments described below were designed to explore the validity of these assumptions.

The net equation of the anodic and cathodic half reactions taking place on the surface of corroding magnesium predicts that the rate of the magnesium dissolution is directly proportional to the amount of hydrogen evolved:

$$Mg + 2H_2O = Mg(OH)_2 + H_2. \quad (33)$$

Although this statement does not seem straightforward in the case of the anodized magnesium samples, to measure hydrogen above the sample in the sample generator – tip collector mode was regarded to be an adequate choice to characterize the corrosion of magnesium in these experiments. Therefore, amperometric SECM experiments were made by setting the tip potential at -0.05 V vs. Ag/AgCl/KCl (3M). Besides, SVET measurements will be presented which may contribute to a better understanding of the negative difference effect. The scanning rate was 25 μm/s throughout the experiments described in this chapter.

In addition, the effect of the noble impurities was investigated by comparing the behavior of pure magnesium and magnesium alloys. In these experiments, magnesium strips of 99.9% purity and strips and rods of AZ63 alloy (6% Al, 3% Zn, 91% Mg) were employed making the samples.

III.3.2. General comparison of the corrosion of pure Mg and AZ63 alloy

Fig 50 shows the Tafel plots of pure Mg (99.9%) and AZ63 alloy in 0.001 M NaCl electrolyte. Interestingly, in the case of higher anodic polarization, namely E > -1.3 V vs. Ag/AgCl/KCl (3 M), the alloy and pure magnesium show very similar behaviors. However, higher cathodic currents were obtained in the case of pure magnesium. The corrosion potential of pure magnesium is almost 0.2 V more positive, the corrosion current is slightly higher.

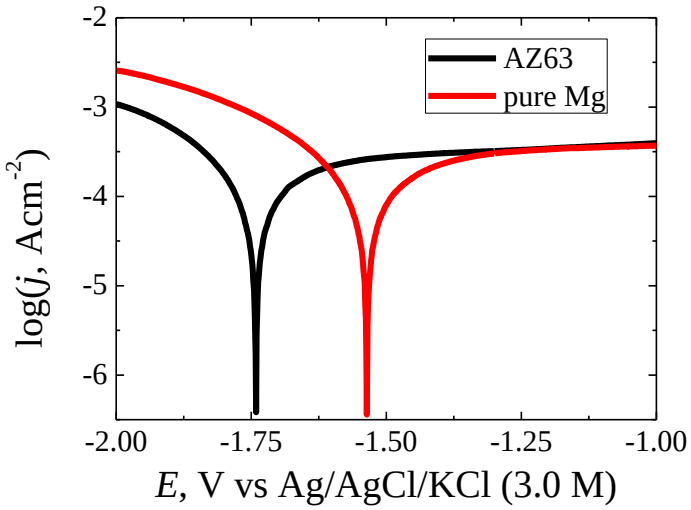

Fig 50. Tafel plots recorded of pure Mg (black) and AZ63 alloy (red) in 1 mM NaCl. Scan rate: 5 mV/s.

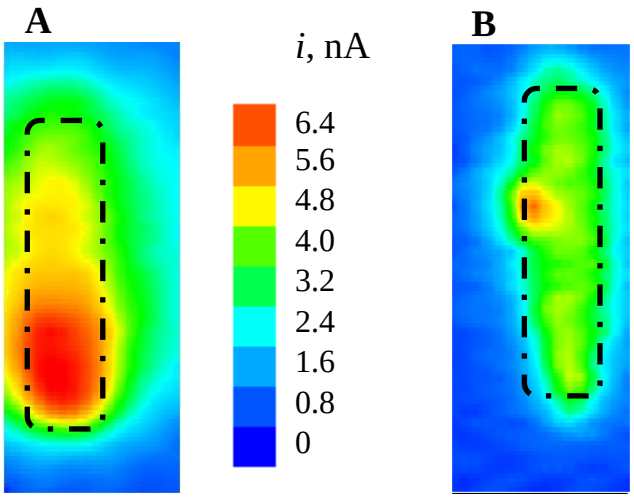

Fig 51. 2D maps (750 µm × 2500 µm) of H_2 evolution from corroding (**A**) Mg and (**B**) AZ63 alloy in 1 mM NaCl. Tip: 25 µm diameter platinum microelectrode. 20 µm vertical distance and 25 µm/s scanning rate.

In **Fig 51** the hydrogen distributions developed above pure magnesium (image A) and AZ63 alloy (image B) can be seen. As it was expected, pure magnesium exhibits higher hydrogen evolution rates than the alloy when no polarization was applied. Roughly, the hydrogen evolution is twice as fast on the pure magnesium as on the alloy. Although the corrosion rate is slower, if the alloying Zn and Al promoted hydrogen evolution, such difference could not be observed.

III.3.3. Effect of the anodic polarization on hydrogen evolution

In order to confirm the first assumption, the following 3-stage experiment has been carried out. After 30 min of immersion in 1 mM NaCl electrolyte, -1.0 V was applied to the sample for 30 min whereas line scans were taken along an arbitrary selected line crossing the sample every 5 min. The tip potential of the Pt micro-disc electrode was held at -0.05 V vs. Ag/AgCl/KCl (3 M) to detect the evolved hydrogen. As it could be seen in the Tafel plot, this potential is well in the anodic range of the metal, hence fast formation of the $Mg(OH)_2$ layer was expected. Then, the potential applied was ceased and the electrolyte was stirred after the polarization stage to remove the adherent hydrogen bubbles on the sample. Subsequently, another set of line scans were recorded in the next 30 min. These hydrogen profiles were taken along the same line as in the first section of this experiment, thus the rate of the hydrogen evolution before and after polarization can be compared. First, the results for the alloy are presented. **Fig 52A** shows the lines recorded over the alloy sample before the polarization, whereas **52B** gives those recorded after the polarization stage. From the comparison of the line scans depicted in **Fig 52A** and **52B**, a progressive decay of H_2 evolution rates with the elapse of time was observed in both cases. However, the decay of hydrogen evolution occurred at a slower pace on the metal after it was subjected to anodic polarization for 30 min. This fact can be observed in **Fig 53** where the average current values corresponding to the plateaus are plotted against the time. Interestingly, an exponential decay was observed along this line, hence the logarithmic values are presented. The slope of the curve originating from the measurements prior to the polarization is more than twice higher than the curve taken after the polarization. This implies that the formed oxide layer enhances the hydrogen evolution rate. Although the difference between the slopes seems to be a convincing evidence for assumption (1), the question arises on the role of the alloying metals, namely, aluminum and zinc. Sanghi and Fleishmann assumed that ZnO produces a catalytic effect on hydrogen evolution [150], however, this has not been proven for aluminum. Another apparent contradiction results from the observed decay after polarization if Mg oxide layer formation is the responsible for the NDE. One would expect that as time progresses more corrosion product should deposit on the surface thus enhancing the HER above it. The experiment carried out on the pure magnesium sample (see **Fig 54**) and the comparison of the results for the magnesium and the alloy may help to find an answer for these questions.

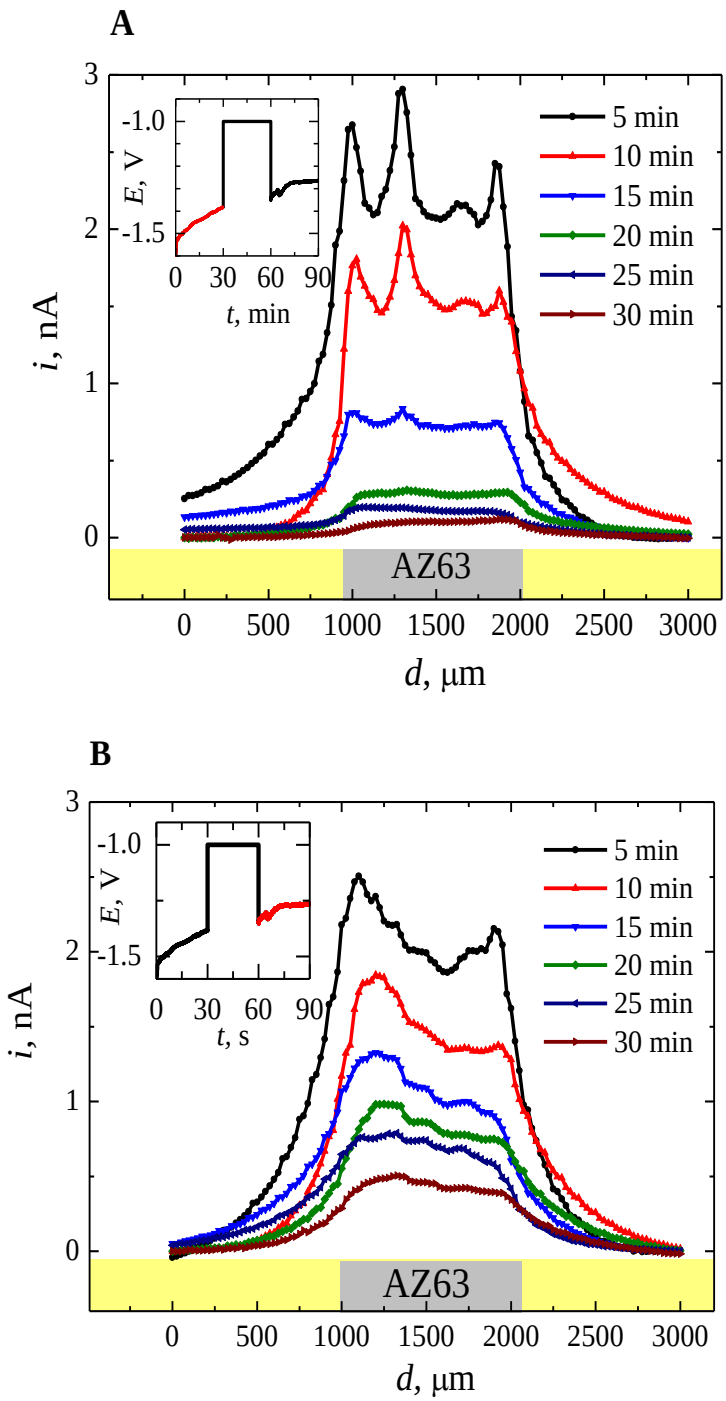

Fig 52. H_2 profiles on AZ63 alloy immersed in 1 mM NaCl solution while a three-step potential program was applied to the sample. A: line scans before polarization, B: line scans after polarization. The insets show the potential of the sample: for 30 minutes, it was let to corrode at its OCP, then it was polarized for 30 minutes and eventually, it was let to corrode at its OCP again. The red sections of the curves in the insets show at which step were the line scans recorded.

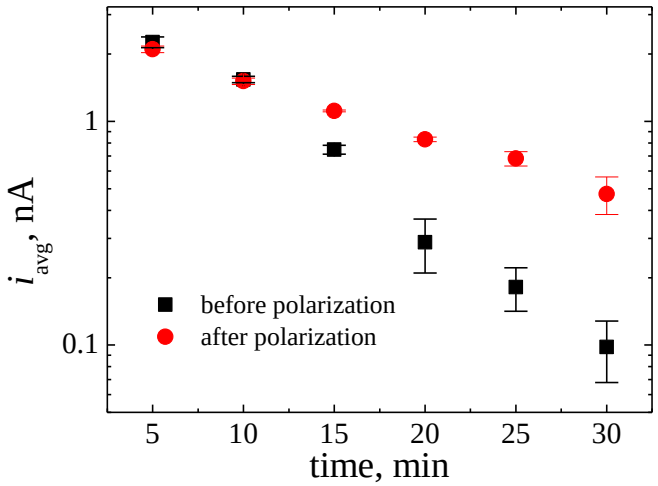

Fig 53. Time evolution of the average H_2 evolution from the line scans of **Fig 52** that were recorded from an AZ63 alloy immersed in 1 mM NaCl solution (**A**) before and (**B**) after the application of an anodic polarization pulse to the sample (30 min at E_{sample} = -1.0 V vs. Ag/AgCl/KCl (3.0 M)).

The same experiments were carried out for the pure Mg sample. The line scans taken at different times of exposig the sample to corroding electrolyte (curves in A and B) and the time function of the current indicating the extent of H_2 (plots in C) are shown in figure **Fig 54.**

The trend of hydrogen evolution on pure magnesium is similar to what has been described for the AZ63 alloy from inspection of the previous figures. At 5 min, the current values (**Fig 54C**) are very close to each other. This means that removal of the adhering hydrogen bubbles formed in the polarization stage was successful and only the H_2 formed during spontaneous corrosion conditions is measured. However, after 5 min there was a large increase in the H_2 evolution rate followed by a slow decay, analogously to the alloy. This pronounced change occurring between 5 and 10 min was observed both before and after the polarization, as well, yet the step was bigger after the polarization stage. The decay after 10 min is slower after the polarization, just as in the case of the alloy. However, an exponential decay was not observed as in the case of the alloy, hence the current values are displayed not the logarithmic values.

From these results, the $Mg(OH)_2$ layer formed in both experiments seems to play a dual role, namely it is a catalyst for H_2 evolution, but it also passivates Mg to some extent, thus explaining the decrease of the H_2 evolution rate. That is, the catalytic effect and passivation are competitive processes for the HER. In the case of the alloy, the decrease of the current is faster, which is consistent with the assumption that Mg (and Al, Zn) oxides cover the magnesium surface, slowing hydrogen evolution. It also means that $Al(OH)_3$ and $Zn(OH)_2$ have stronger passivating action, and these “noble” impurities will not increase the rate of H_2 evolution significantly, conversely to $Mg(OH)_2$. Otherwise, we would observe a slower decay in the case of the alloy.

Besides, the difference between before and after polarization stages is more pronounced for pure Mg than in the case of the alloy. By observing the scales used in the figures it is possible to observe that the highest currents are almost twice as big after the polarization stage. When it comes to the alloy, it is higher only by ca. 10 %.

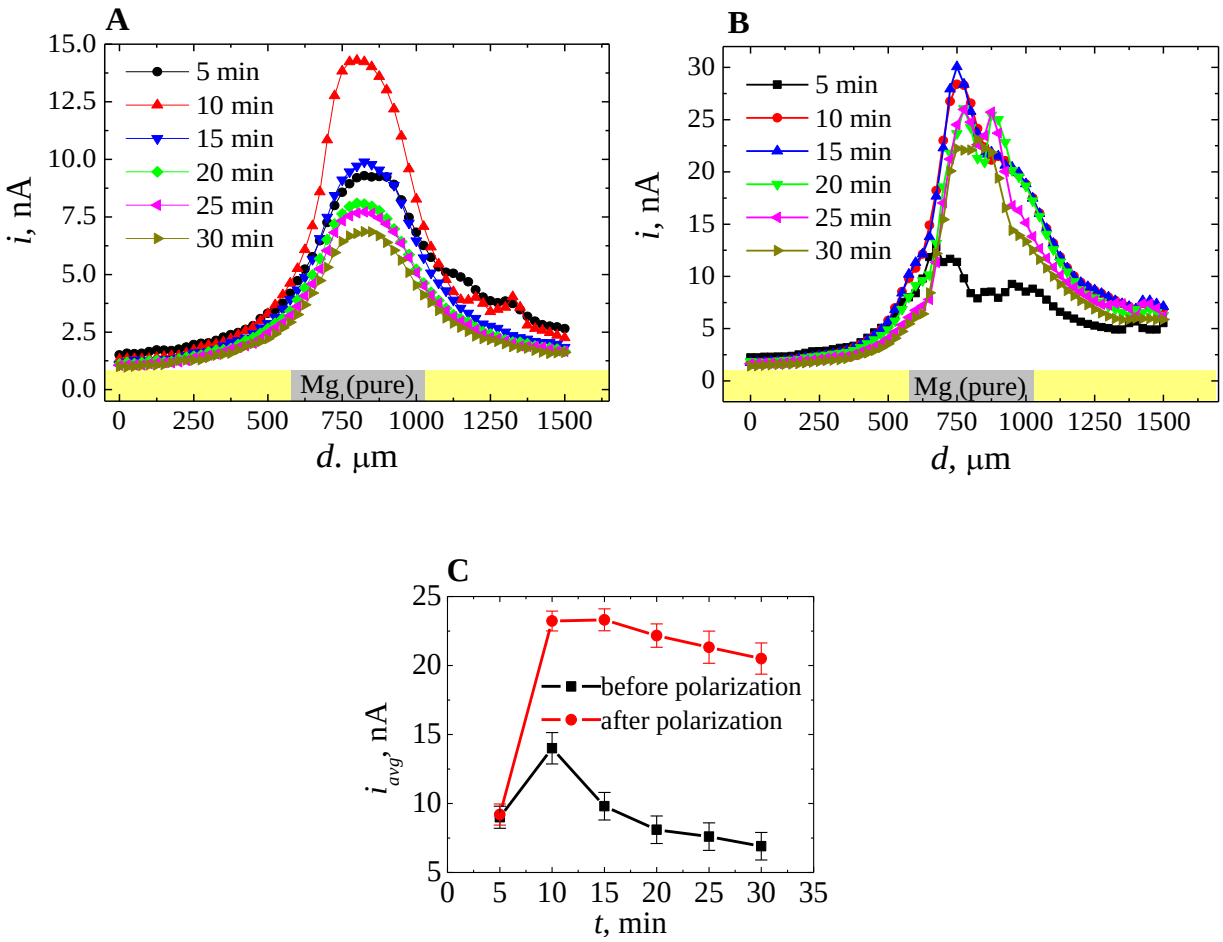

Fig 54. Line scans demonstrating the time evolution of H_2 evolution on pure magnesium (**A**) before and (**B**) after the anodic polarization stage. (**C**) Time dependence of the average current values of the plateaus the line scans. 20 µm vertical distance and 25 µm/s scanning rate.

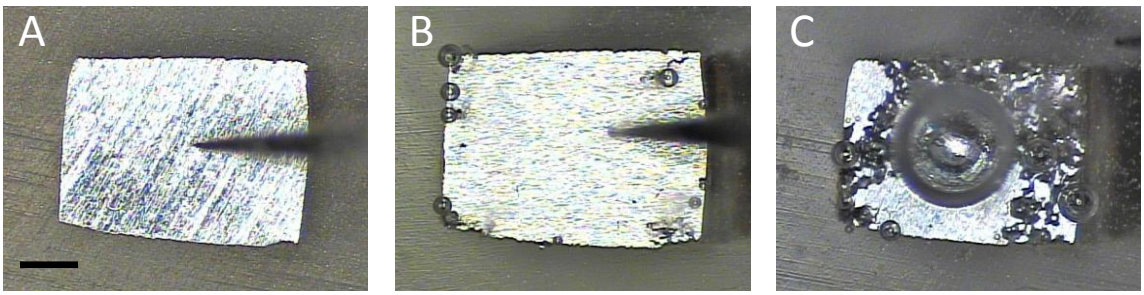

Fig 55. Optical micrographs of an AZ63 alloy sample immersed in 1 mM NaCl: (**A**) prior to the addition of the test solution; (**B**) at the spontaneous OCP in the test solution; (**C**) following the application of an anodic polarization step at -1.0 V vs. Ag/AgCl/ KCl (3.0 M) for 10 min.

The enhanced H_2 evolution after anodic polarization was further characterized from a sequence of micrographs taken during an independent experiment, which is shown in **Fig 55**. The freshly polished sample of the alloy placed at the bottom of the SECM small cell can be seen in **Fig 55A** prior to the addition of the 1 mM NaCl solution. In **Fig 55B** the micrograph was taken immediately after the saline solution was added to the cell, while **Fig 55C** depicts the state of the system immediately after the anodic polarization was stopped. The greater H_2 fluxes arising from the magnesium alloy following anodic polarization are readily observable, although the OCP values did not change significantly from those recorded prior to the application of the anodic polarization step. The increased fluxes of hydrogen gas are in good accordance with the observations of the SECM experiments.

III.3.4. Effect of Mg^{2+} ions on the hydrogen evolution rate

The previous section demonstrated that the formation of the $Mg(OH)_2$ enhanced the hydrogen evolution rate on Mg. Although the comparison of the pure Mg and the alloy provided some evidences that the "noble" impurities have no significant role in the HER, the anodic polarization not only promoted the formation of the magnesium oxide/hydroxide but also the oxides/hydroxides of the alloying and the impurity metals. For this reason, an alternate approach was envisaged to enhance the $Mg(OH)_2$ layer formation selectively. The second assumption listed in the introduction of this chapter predicts that the addition of Mg^{2+} ions to the electrolyte will increase the hydrogen evolution rate. It was shown in the previous chapter that the pH increases rapidly in the close vicinity of the magnesium sample often reaching pH values higher than 10. Hence, enhanced formation of the oxide layer is expected due to the precipitation of the Mg^{2+} ions in the electrolyte. As opposed to the anodic polarization, the addition of Mg^{2+} containing electrolyte would only result in the enhancement of $Mg(OH)_2$ layer formation, but has no direct influence on the growth of other metal oxides and hydroxides. On the other hand, the previous findings showed that there is a decay in the rate of the HER with time. This was previously explained by assuming a dual role for the Mg oxi-hydroxide bilayer, that is apart from the catalytic activity on the HER, and thus contribute to isolate the metal surface. To test this hypothesis, $MgCl_2$ solutions of two different concentrations were employed assuming that the less concentrated one (namely, 1 mM) would contribute to increase the rate of the HER, whereas the higher concentration (0.1 M) would produce the opposite effect. The experiments were repeated in NaCl solutions with identical Cl^- concentration to those in the $MgCl_2$ solutions. **Fig 56** shows the H_2 evolution distribution on the AZ63 alloy immersed in 1 mM NaCl + 1 mM $MgCl_2$ solution. Due to the increased chloride concentration in the test solution, the experiments were repeated in 3 mM NaCl solution for comparison. Differences in the rates of HER from AZ63 samples immersed in the two electrolytes could be directly observed from the SECM maps. It was found that greater fluxes of hydrogen gas were recorded when the magnesium alloy was immersed in a solution containing Mg^{2+} ions. In addition, when the experiment was repeated on freshly prepared

AZ63 samples using an Sb-based ME for potentiometric SECM operation, significant pH differences were observed between the samples immersed in either electrolyte as shown in **Fig 57**. It was found that the pH above the corroding metal was higher by 0.5 units when it was immersed in the solution containing $MgCl_2$, a fact consistent with the higher rate of HER in this case. Although only a few selected images are shown here, the SECM experiments were repeated several times as to derive reproducible observations from the data.

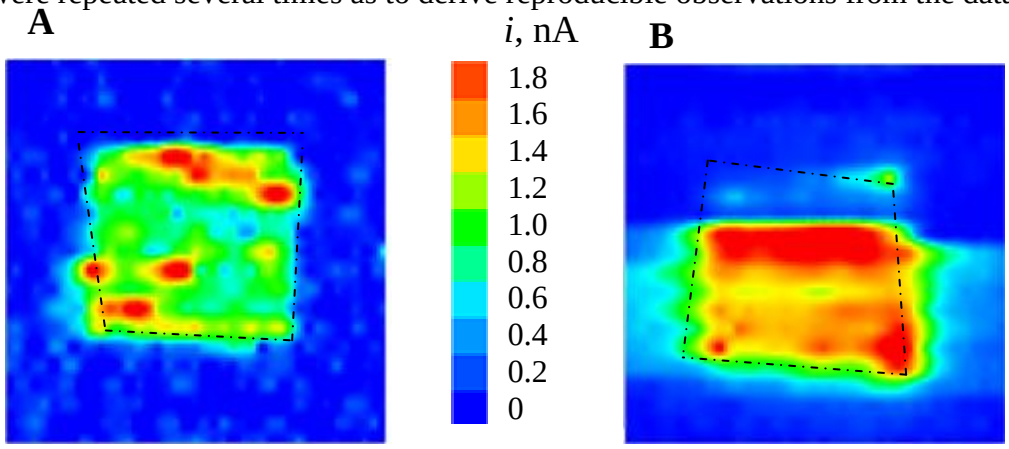

Fig 56. H_2 evolution maps recorded using a Pt microelectrode scanned over an AZ63 alloy sample immersed in (**A**) in 3 mM NaCl, and (**B**) in 1 mM NaCl +1 mM $MgCl_2$. 20 μm vertical distance and 25 μm/s scanning rate.

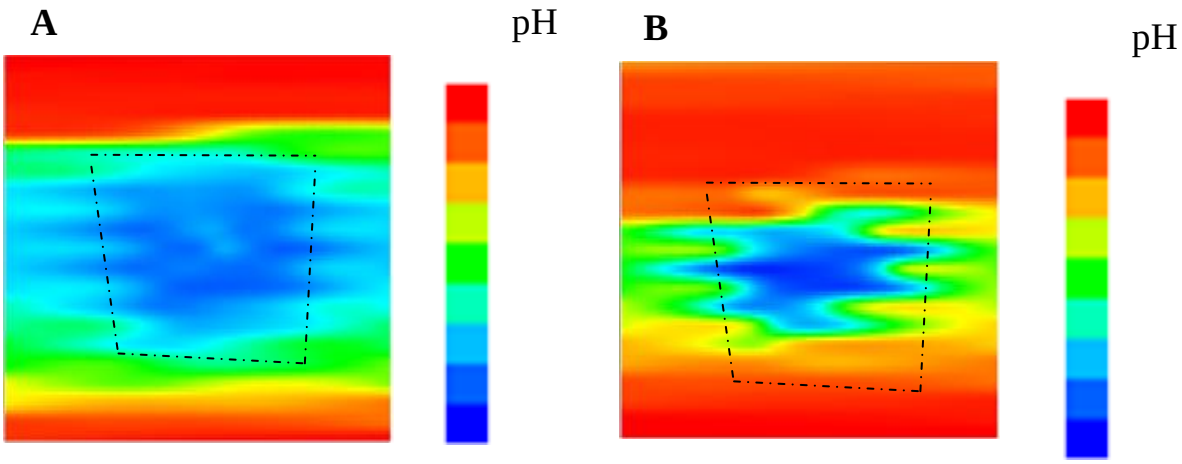

Fig 57. pH maps recorded with a Sb microelectrode in 3 mM NaCl over an AZ63 alloy sample immersed in (**A**) in 3 mM NaCl, and (**B**) in 1 mM NaCl +1 mM $MgCl_2$. 20 μm vertical distance and 25 μm/s scanning rate.

The corresponding results for pure magnesium can be seen in **Fig 58.** Similarly to the previous case, the hydrogen flux arising from the sample increased significantly in the solution containing $MgCl_2$. The behavior of the alloy and the pure magnesium was compared as follows. Lines were selected from the 2D scans in which the tip crosses the sample and similarly to the line scan, the plateaus were averaged. In this way, a rough estimation can be made for the hydrogen evolution rate, thus the increases in the rate of the HER due to the addition of $MgCl_2$ could be compared. Despite the rough estimation involved (that is, since

the elapse of time during scan acquisition cannot be taken into consideration, the map is effectively regarded as an instantaneous image of the H_2 flux), a significant difference between the alloy and the pure magnesium could be observed. In the case of the alloy, the addition of $MgCl_2$ caused an about 1.76 times higher hydrogen evolution rate, whereas the increase was 2.91 times for pure magnesium. This is in a good agreement with the conclusion made in **Section 3.2.** The line scans also revealed a decay of the rate of the HER in time that was faster in the case of the alloy. It seemed that the oxides formed in the anodic dissolution partially insulate the magnesium surface. In order to test this conclusion, a new series of line scans were performed above the pure magnesium in either 0.1 M $MgCl_2$ or 0.2 M NaCl solutions. This high concentration of Mg^{2+} would favor the fast formation of the $Mg(OH)_2$/MgO bilayer, and the insulator role was expected to be more pronounced than the catalytic effect. The line scans crossing the pure Mg stripe and the Mg alloy were recorded every 5 min for 40 min (the average current values are plotted in **Fig 59A** and **59B**, respectively). In the case of the 0.1 M $MgCl_2$ solution the plateaus presented a rather smooth decay with time, although there was a small increase after 20 min (see **Fig 59A**). On the other hand, a greater fluctuation of the plateaus could be observed in the measurements performed in 0.1 M NaCl, and the decreasing tendency in the rate of the HER after 5 minutes could not be resolved explicitly. It has also to be mentioned that in the presence of Mg^{2+} ions, the initial line scan shows more than 1.5 times higher HE rate than in 0.2 M NaCl. That is, initially the catalytic effect of the $Mg(OH)_2$ layer can be clearly observed. Afterwards the decay in the HE rate seems to be faster in the presence of the high concentration $MgCl_2$. Although these findings seem to support our hypothesis, 2D scans were performed after 60 min immersion time to obtain the total distribution of hydrogen evolution on the pure magnesium. **Fig 60** shows the H_2 maps recorded in the two electrolytes. In a good agreement with the line scans, a higher H_2 flux was detected in the 0.2 M NaCl for both materials. That is, these maps exhibit the opposite behavior towards the HER with $MgCl_2$ addition to that previously described for the previous experiments with a smaller concentration of $MgCl_2$.

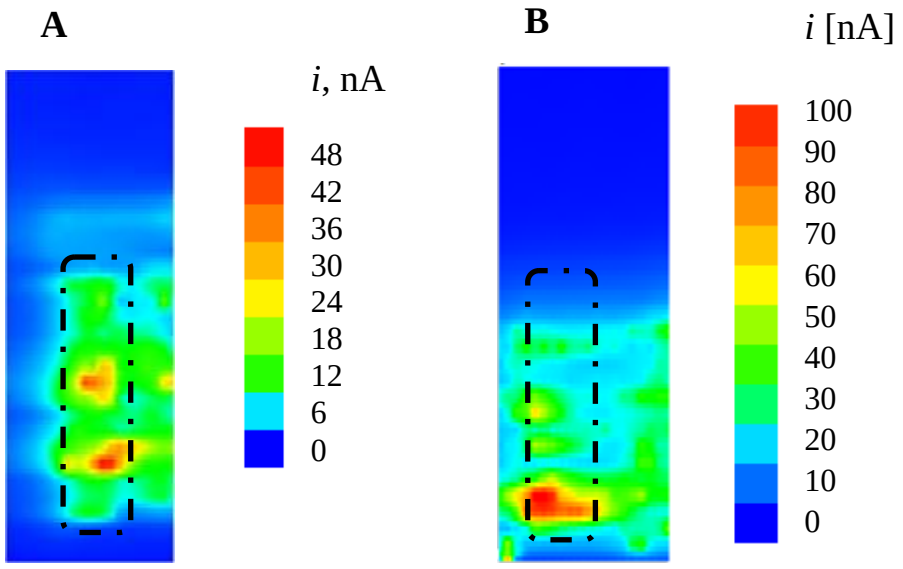

Fig 58. H_2 evolution maps recorded over pure Mg after 40 min immersion in: (**A**) 3 mM NaCl; (**B**) 1 mM $MgCl_2$ + 1mM NaCl. Scan dimensions: 1000 µm × 3000 µm.

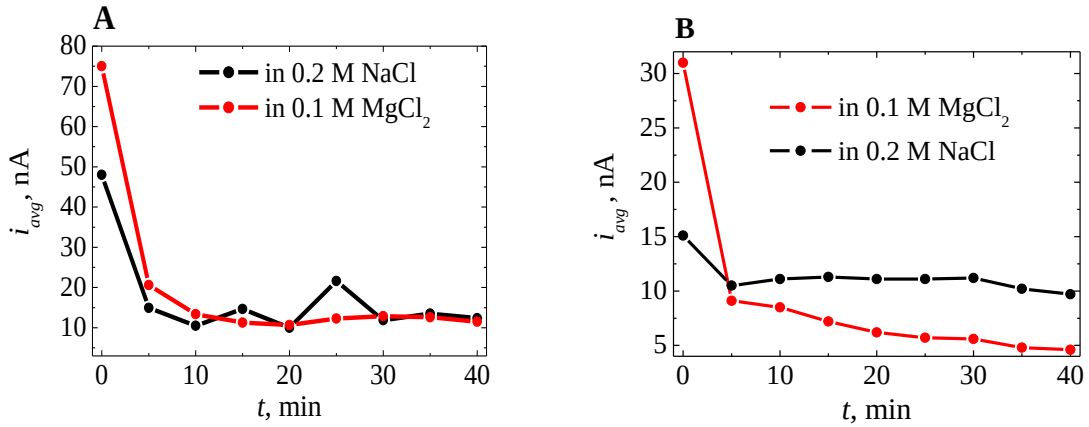

Fig 59. Time evolution of the average H_2 fluxes derived from selected line scans recorded over (**A**) pure Mg, and (**B**) AZ63 alloy samples.

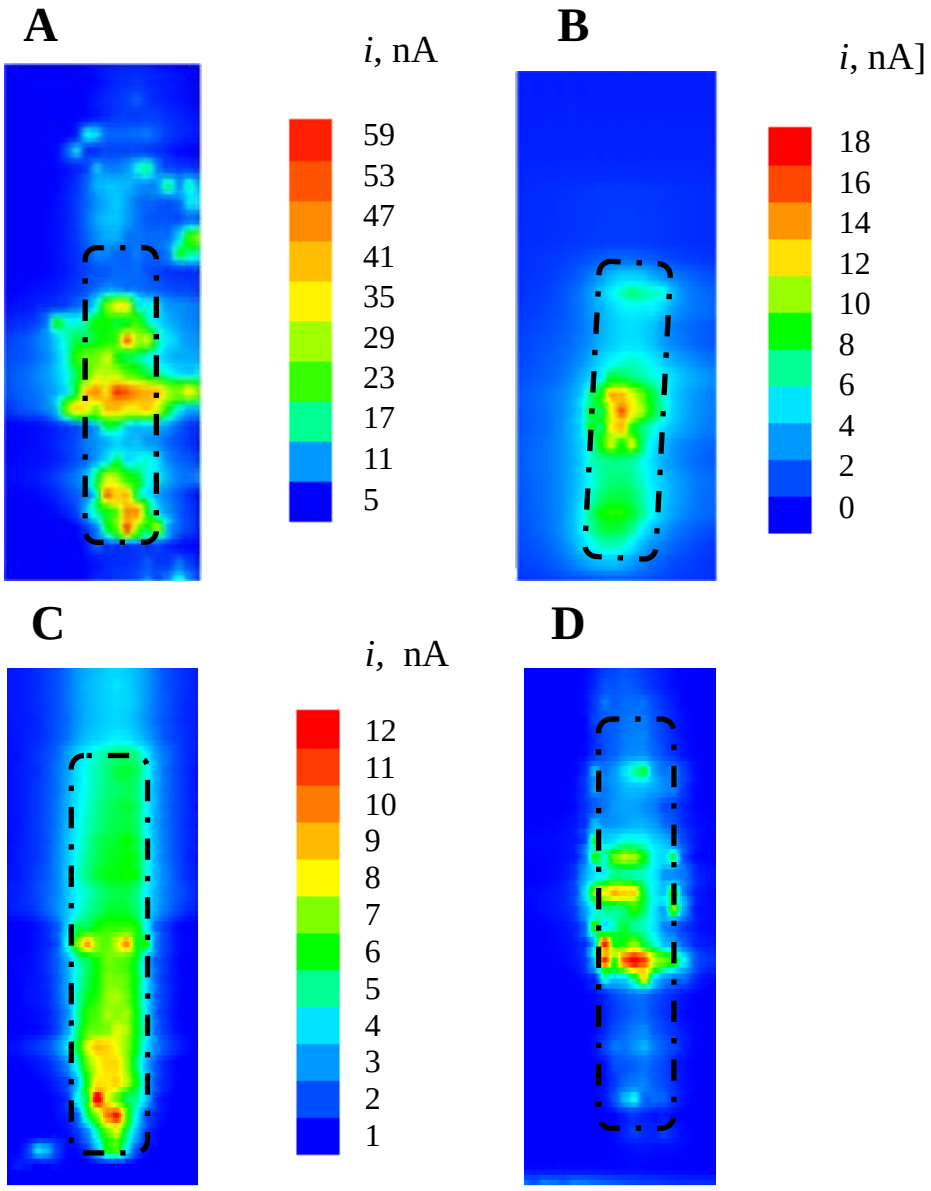

Fig 60. H_2 reduction amperometric current maps recored over (**A**, **B**) pure magnesium and (**C**, **D**) AZ63 alloy samples after 60 min immersion in: (**A**, **C**) 0.2 M NaCl, (**B,D**) 0.1 M $MgCl_2$. Scan dimensions: 1000 µm × 3000 µm.

III.3.5. Effect of a complexing agent for Mg^{2+} ion on the hydrogen evolution rate

The findings presented in the previous two Sections have already demonstrated the kind of effect produced on the rate of the hydrogen evolution by promoting the formation of the $Mg(OH)_2$ layer.. The results are not as implicit as it was stated in our first two assumptions in the introduction of this Chapter, hence some modifications have been made in our hypothesis, namely the invocation of the dual role of the magnesium-oxide layer. Nevertheless, the line scans and H_2 maps recorded in different electrolytes for both materials are fully consistent with this new hypothesis. It seemed to be beneficial if a new approach is introduced to simplify the picture. That is, inasmuch that catalytic layer formation is hindered, one would expect slower hydrogen evolution. The advantage of this approach is that we can exclude the thickness dependence from the overall impact of the layer. Since the removal of the layer in acidic media would also increase hydrogen generation on the corroding magnesium surface, no unambiguous results could be expected from such experiment. On the other hand, the addition of a complexing agent that captures the free Mg^{2+} released from the sample seemed to be an option with minimal eventual perturbation of the system under investigation. Ethylene-diammine-tetraacetic acid (EDTA) has been used for a long time in complexometric titrations for Mg^{2+} determination. The titrations are carried out in alkaline (pH=10) media, implying that the complexation reaction is fast even within the pH range that can be expected in the vicinity of a corroding Mg sample. That is, the complexation reaction will happen to a greater extent than the precipitation of the magnesium-hydroxide, thus formation of the catalytic layer is hindered.

Fig 61 displays the H_2 evolution maps recorded over the AZ63 alloy. For easier comparison the same color scale was employed in the two maps. Significantly smaller hydrogen evolution can be observed when the solution contains the complexing agent. The experiment was also repeated under anodic (i.e., at -1.0 V vs. Ag/AgCl/KCl (3 M)) polarization (**Fig 62**). The decreased hydrogen generation rate due to the hindering of the catalytic layer formation is readily observable here, as well.

Very similar results were obtained in the case of the pure magnesium. **Fig 63** shows typical results for pure magnesium at the OCP. The different behavior related to the addition of the complexing agent is even more noticeable in this case.

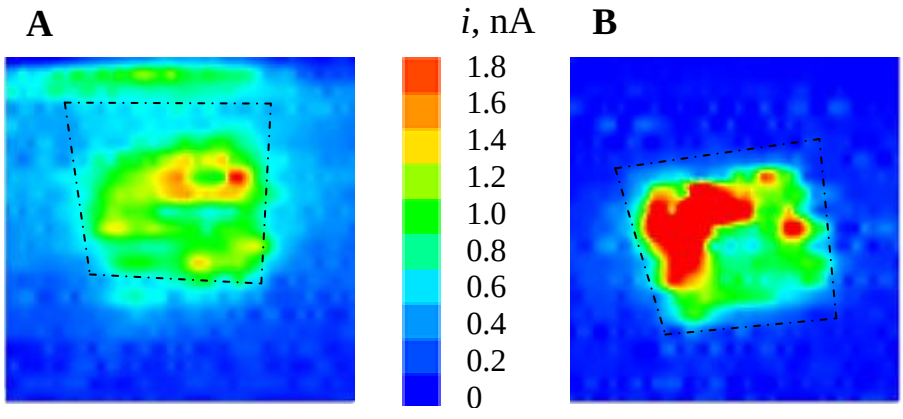

Fig 61. H_2 evolution maps recorded over the freely corroding magnesium in: (**A**) 1 mM NaCl + 10 mM EDTA, (**B**) in 1 mM NaCl solutions. Scan dimensions: 2000 µm × 2000 µm.

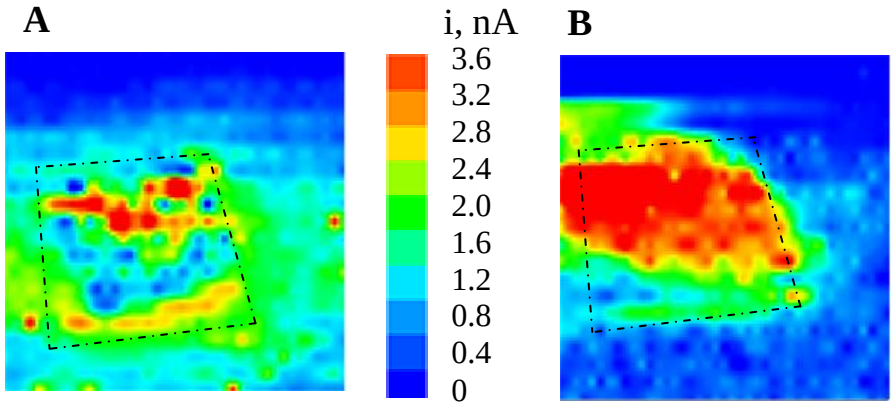

Fig 62. H_2 evolution maps recorded over the anodically magnesium polarized at -1.0 V vs. Ag/AgCl/KCl (3 M) while immersed in: (**A**) 1 mM NaCl + 10 mM EDTA, (**B**) 1 mM NaCl solutions. Scan dimensions: 2000 µm × 2000 µm.

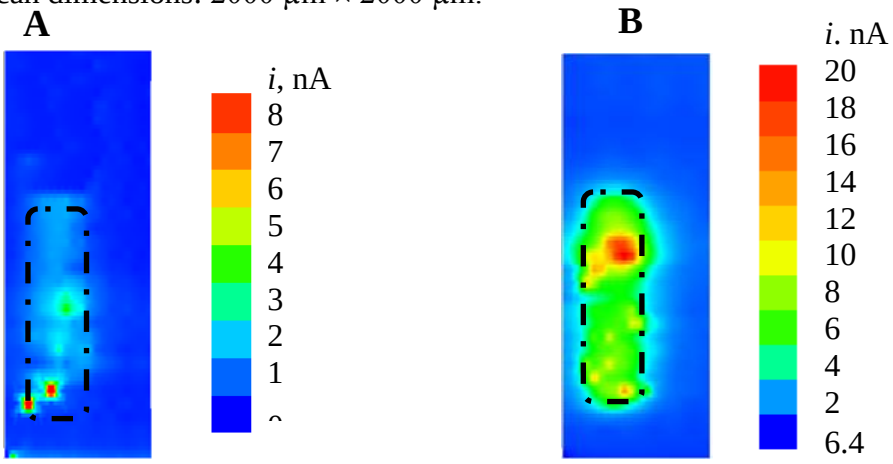

Fig 63. H_2 evolution maps recorded over pure Mg immersed in: (**A**) 1 mM NaCl + 10 mM EDTA, (**B**) 1 mM NaCl solutions. Scan dimensions: 950 µm × 3000 µm.

III.3.6. SVET measurements on anodically polarized samples

The Scanning Vibrating Electrode Technique (SVET) was employed to detect local anodic and cathodic activities above a cathodically and anodically polarized magnesium sample compared to its behavior during spontaneous corrosion at the OCP. By repetitions of the Tafel experiments (one example was shown in **Fig 50**) the shift of the E_{corr} was noticed, thus prior to the SVET measurements OCP measurement was carried out to select the potential values for cathodic and anodic polarization. The cathodic polarization potential was selected 300 mV below the measured OCP (namely, -1.40 V vs. Ag/AgCl/KCl (3.0 M)), the weak anodic polarization was 100 mV higher than the OCP, and the effect of the frequently applied polarization in this work at -1.0 V was also investigated. The local current density maps for the AZ63 alloy at the four different applied potentials can be seen in **Fig 64.** The experiments were implemented on freshly prepared samples. In the case of the cathodic

polarization, the whole sample acted as a big cathode, and no localized phenomena could be detected with the vibrating probe. At the open circuit potential, some anodic activity could be also detected, mainly occurring close to the edges of the sample. By increasing the potential to -1.3 V , the anodic activity increased, but more interestingly a large local cathode was observed as well (**Fig 64C**) at the top right corner of the image (cf. **Fig 64C**). The negative current densities are related to the diffusion of the OH^- ions released as the consequence of the hydrogen evolution reaction. The last map (**Fig 64D**) shows the result for the anodic polarization at -1.0 V that was applied in the previous sections. At this potential, the whole sample became electrochemicaly active (in maps **B** and **C**, some areas remained inactive during the scan time). The anodic activity increased further reaching relatively high local current density values, however, the local cathodes still exist on the sample surface. It is noteworthy that the local cathodic areas are not as finely distributed on the sample as one would expect according to the noble impurities theory.

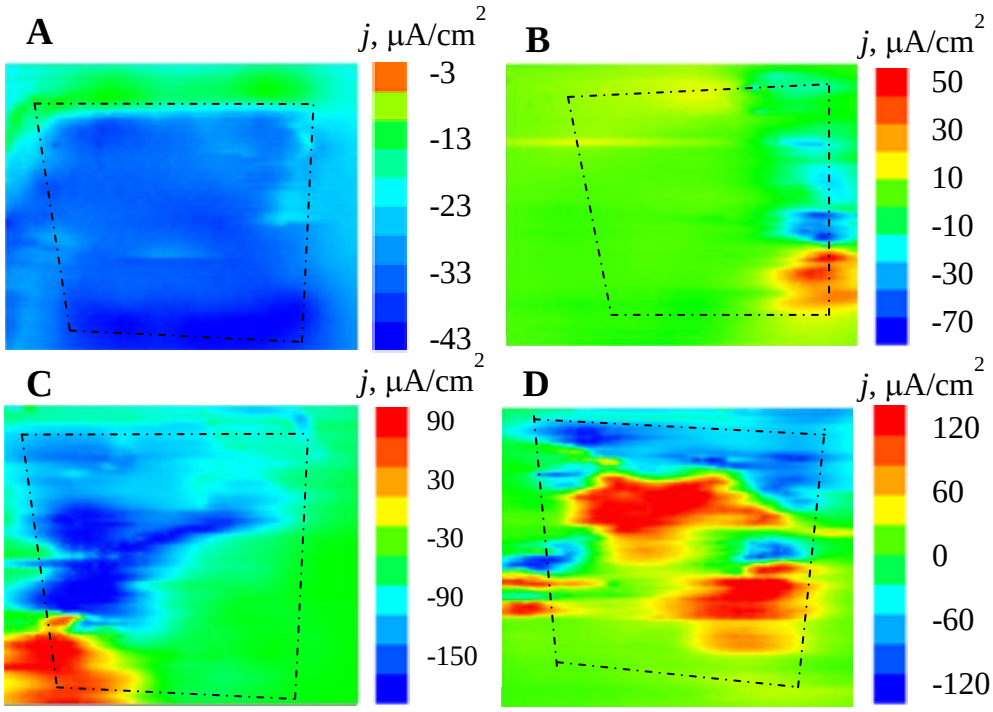

Fig 64. Ionic current maps recorded over an AZ63 sample immersed in 1 mM NaCl. Electrical condition of the sample: (**A)** polarized at –1.7 V vs. Ag/AgCl/KCl (3.0 M), (**B)** OCP, (**C)** -1.3 V, and (**D)** -1.0 V. The images represent an area of 1500 µm × 1250 µm. The average height of the vibrating tip was 50 µm; vibration amplitude along *Z* axis: 20 µm; step width: 18 µm.

Chapter 4 - Investigation of the anomalous hydrogen evolution on magnesium during galvanic corrosion

III.4.1. Resume

In the previous chapter a systematic study of the negative difference effect was presented. The results obtained with the amperometric SG-TC mode of the SECM supported the catalytic effect of the $Mg(OH)_2$/MgO bilayer. The comparative experiments of the pure Mg and the AZ63 alloy helped to separate the effect of the noble impurities from the catalytic effect. Next, the experiments done above prepolarized and nonpolarized magnesium and AZ63 provided additional new information on the hydrogen evolution reaction. This Chapter aims to investigate the role of the alloying metal on the HER. To this end, samples containing an Mg-Al galvanic pair were prepared, in order to study the HER separately on the metals. The galvanic connection creates similar conditions to those in the microenvironment of a matrix containing nobler impurities. The experiments themselves will be very similar to those presented in Chapter 3, although the hydrogen 2D maps were recorded while the galvanic connection was established. That is, the measurements were performed under *in situ* polarization condition, thus a closer look can be made to the negative difference effect.

III.4.2. SVET measurements above the AZ63 anode of the AZ63/Fe galvanic pair

There are many differences between anodic polarization at constant potential and the anodic polarization in the connected galvanic pair. In the latter case the potential difference between the anode and the cathode is not constant, but it is decreasing just as in a battery. This potential difference, which is the driving force of the corrosion, depends also on the electrolyte conductivity. On the other hand, when a potentiostat is connected, the potential against the reference electrode is set by the potentiostat "taking the conductivity into account" and any change is compensated by driving current through the auxiliary electrode in order to mantain the constant potential on the sample during the experiment.

In Chapter 3 the distribution of the local current densities on Mg at different potentials were mapped using SVET. In the case of galvanic corrosion, it is possible to record the evolution of the corrosion process with time. The SVET equipment is provided with an optical microscope videocamera that takes images before and after recording single maps. The photographs show the cumulative effect of corrosion on the sample and help to evaluate the current density maps that depict the active areas at the time the maps were recorded. **Fig 65** shows a series of scans recorded above the AZ63 specimen while it was electrically connected to iron and immersed in 1 mM NaCl. During the experiment vigorous hydrogen bubbling could be observed with the videocamera, and this feature is also recorded in the micrographs (**Fig 65B, D** and **F**).

Initially, the two sides of the alloy were electrochemically active (see **Fig 65A** and **B**). Although one would expect that the galvanic connection to the iron specimen would produce

the complete separation of the anodic and cathodic areas, however, likewise in the previous findings with SVET described in Chapter 3, both anodic and cathodic spots appear on the surface of the magnesium anode. The distribution of these active areas correlates well between the current density map and the photograph, yet the distribution of the cathodic and the anodic areas cannot be easily distinguished in the photograph. The location of the bubbles indicate the cathodic areas, although the travel of the vibrating tip above the sample may also toss the bubbles away from their original source, and the bubbles spontaneously detache from time to time too, thus the micrograph by itself does not provide fully reliable information on the distribution of the anodic and cathodic sites. Interestingly, after 2 hours of immersion, the two sides of the sample have become inactive and a new corroded area appeared in the middle of the sample displaying high ionic flows (**Fig 65C** and **D**). Again, the shape of the new dark corroded area seems to correlate well with the current density map, although the previously active and corroded areas can be still seen in the micrograph. After 4 hours, **Fig 65E** and **F** show that the active areas were located on the right side of the sample. On the micrograph a relatively big bubble can be seen on the top left corner of the sample which possibly was left behind from a previous stage of the corrosion. The cathodic activity is still very significant on the AZ63 anode.

This experiment showed that active areas in the galvanic corrosion of the magnesium alloy are more localized than it could be seen in the previous chapter where almost the complete sample was active under potentiostatic polarization condition. This is in agreement with the findings of the multi-barrel measurements in Chapter 2. The localized character of the anodic dissolution implies that line scans are not representative for the whole sample and comparison between two measurements can only be made if the line scan is recorded along the same line and the two measurements are performed successively.

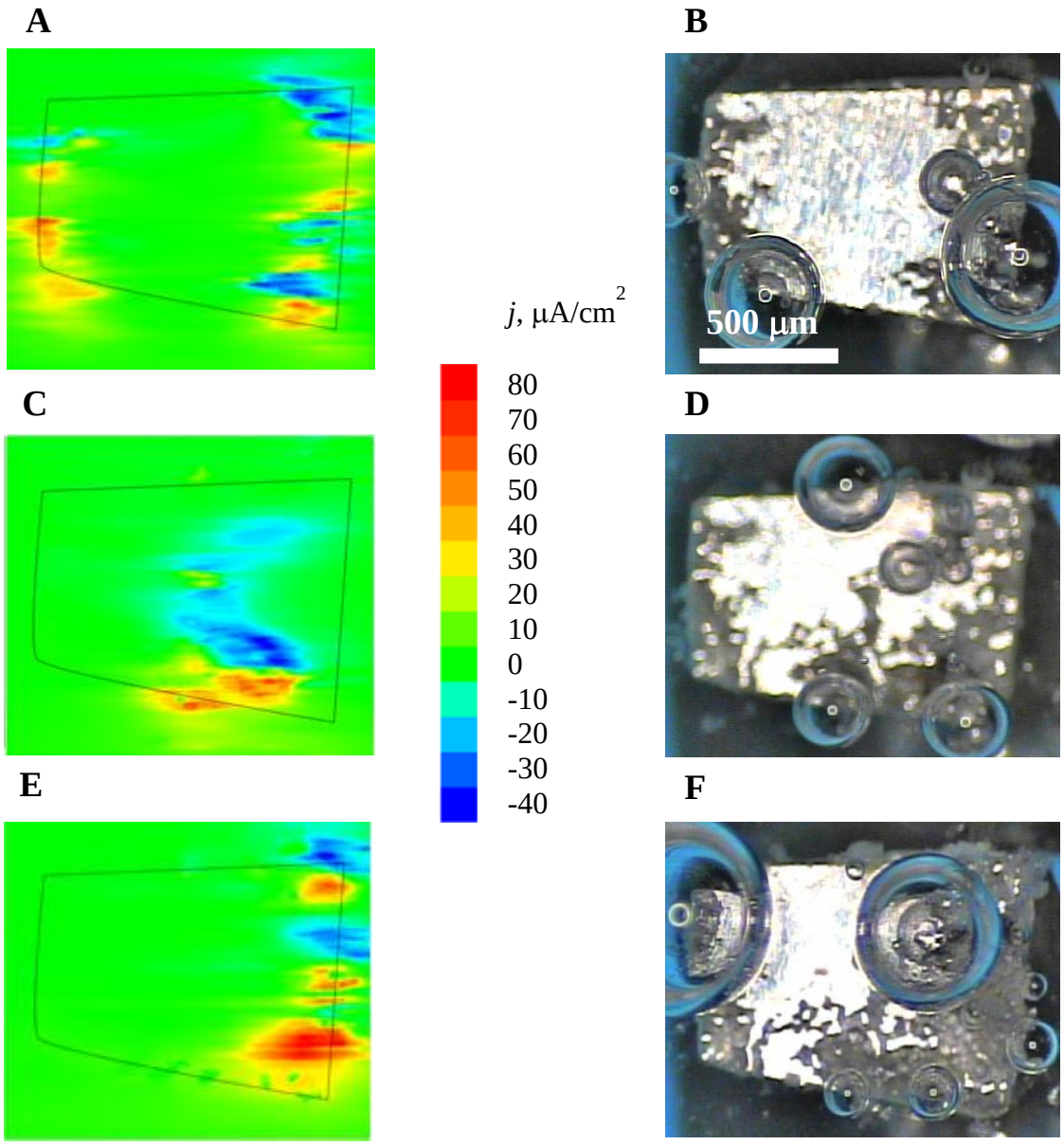

Fig 65. Stages of the galvanic corrosion of an AZ63 alloy sample connected to iron in 1 mM NaCl after different elapsed times: (**A**, **B**) 0, (**C**, **D**) 120, and (**E**, **F**) 240 min. (**A**, **C**, **E**) SVET current density maps and (**B**, **D**, **F**) microphotographs of the sample. Scan dimensions: 1400 μm × 1300 μm.

III.4.3. Characterization of the Mg-Al galvanic pair

In order to obtain a deeper insight of the alloying role of aluminum metal on the NDE, a sample containing pure Mg and Al strips was prepared. In this way, the effect of the different additives considered in Chapter 3 (namely, $MgCl_2$ and EDTA) on hydrogen evolution could be investigated separately. The Tafel plots of the two metals can be seen in **Fig 66.** According to the mixed potential theory, the corrosion potential of the electrically connected metals can be estimated from the Tafel plots of the individual metals as the intersection of the anodic branch of AZ63 with the cathodic branch of aluminum. The intersection point of is indicated in **Fig 66** with an arrow and it is about -1.54 V vs. Ag/AgCl/KCl (3.0 M). This value means that in the case of galvanic corrosion, H_2 evolution will occur on both surfaces: as the cathodic reaction on the Al and as the consequence of the NDE on the Mg. On the other hand, this negative mixed potential value also implies that the potential values applied in the line scans described in Chapter 3 (that is, -1.0 V vs. Ag/AgCl/KCl (3M)) corresponds to an anodic polarization condition for both metals. That is, no hydrogen evolution should occur on the Al sample, whereas HER should take place on the Mg if the metals are polarized at this potential value. To test this hypothesis, line scans were recorded above the sample containing the two metals while -1.0 V were applied on the metals either separately or together (the latter is modelling the behavior of the alloy where both galvanic corrosion and anodic polarization may occur). In **Fig 67** the line scans can be seen. As it was expected, no hydrogen evolution was observed on the Al sample, whereas Mg produced H_2 in each experiment. When solely the Mg was polarized, a similar HER rate was observed to the polarized galvanic couple. When only Al was polarized, milder HER could be detected on the Mg surface due to the cathodic reaction of the spontaneous corrosion of Mg. The higher H_2 evolution rates on the polarized Mg are due to the negative difference effect.

These findings confirm that the prepolarization experiments described in Chapter 3 did not produce hydrogen on the Al impurities. On the other hand, in the case of galvanic connection, as the Tafel plot indicated, there should be hydrogen evolution on the Al sample, as well, since E_{corr} is sufficiently low (~ -1.54 V vs. Ag/AgCl/KCl (3M)). In **Fig 68**, line scans can be seen on the spontaneously corroding and galvanically connected samples. Accordingly to our expectations, the HER peak appeared above the Al, yet significantly higher hydrogen flux was detected above the magnesium anode, too. The increased rate of the hydrogen evolution due to the galvanic connection could be observed. However, the rates of the HER cannot be compared between the Al and Mg, because as we have seen earlier, in the case of galvanic corrosion, HER is also very localized, hence 2D maps should be recorded to obtain a global picture of the corrosion of the samples.

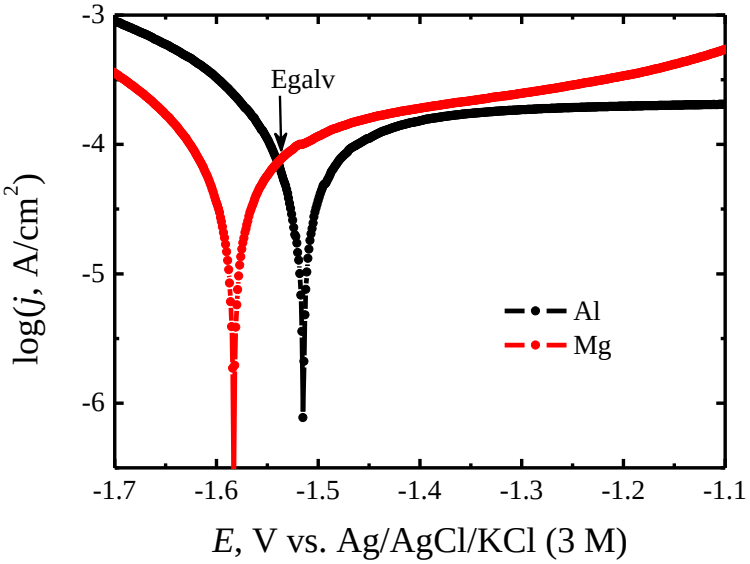

Fig 66. Tafel plots of pure Mg and Al samples after 30 min immersion in 1 mM NaCl. The reference electrode was Ag/AgCl/KCl (3M) and the counter electrode was a platinum mesh. The arrow shows the estimated potential of the galvanically connected metals. Metal dimensions: 300 μm × 2000 μm.

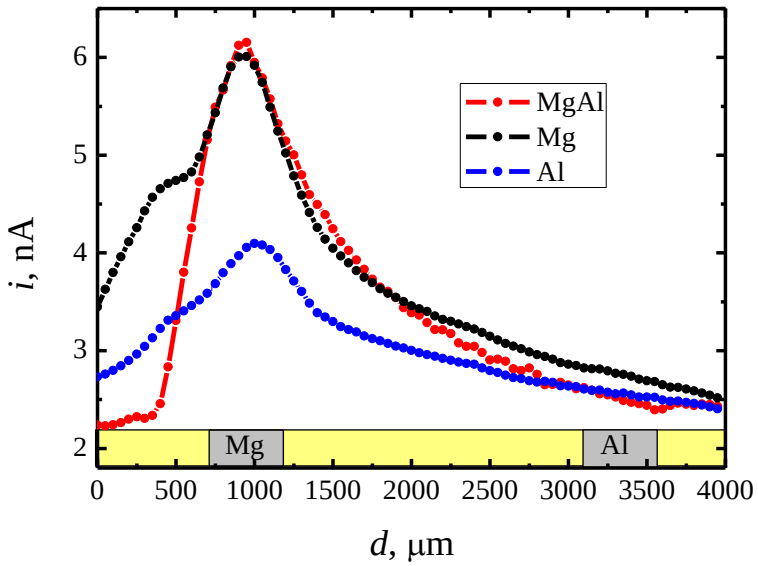

Fig 67. Line scans recorded above the polarized Mg-Al pair immersed in 1 mM NaCl. The samples were polarized at -1.0 V vs. Ag/AgCl/KCl (3M) throughout the scans. The red curve corresponds to the direct electrical connection between the Mg and the Al samples, hence both of the metals were polarized at -1.0 V vs. Ag/AgCl/KCl (3M). 20 μm vertical distance and 25 μm/s scanning rate.

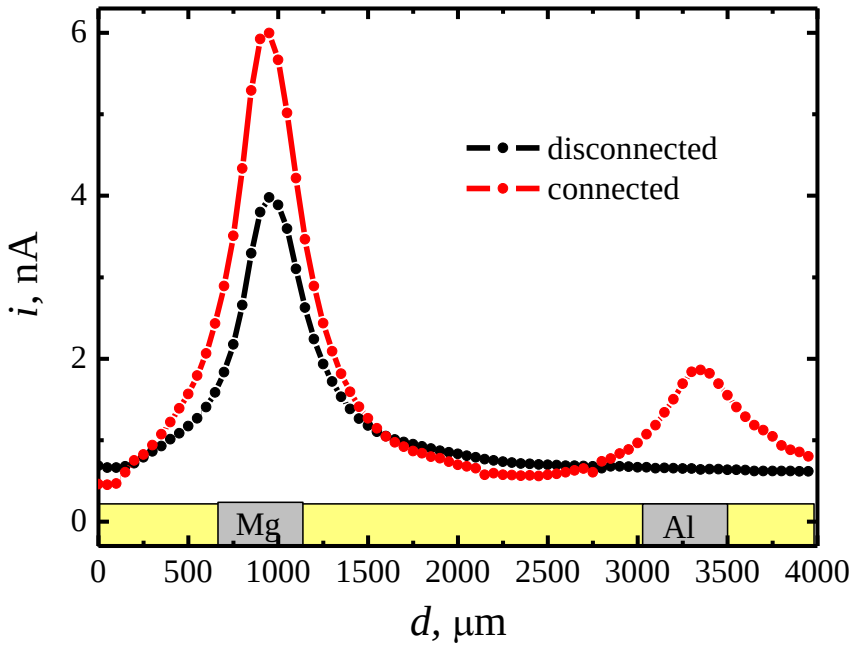

Fig 68. Line scans recorded above the galvanically connected and disconnected Mg-Al pair immersed in 1 mM NaCl. 20 μm vertical distance and 25 μm/s scanning rate.

III.4.4. Hydrogen evolution on the Mg-Al galvanic couple in the presence of Mg^{2+} ions

In the next experiments, amperometric H_2 evolution 2D maps were recorded above the connected Mg-Al galvanic couple, and the effect of the different electrolytes on the HER was investigated. In **Figs 69** and **70** two maps of the hydrogen fluxes are shown, respectively in the absence and in the presence of Mg^{2+} ions. The chloride concentration was the same (e.g., 2 mM) in both solutions, thus the difference between the maps could be solely attributed to the nature of the Na^+ and Mg^{2+} ions. It can be seen that just as in our experiments in **Section 3.4**, the addition of $MgCl_2$ significantly enhanced the HER on the magnesium (cf. **Fig 70**). The distribution of the hydrogen formation is not uniform, but the most active areas show peaks about 14 nA, whereas in **Fig 69**, the current barely exceeds 6 nA above the Mg strip. The difference in the case of Al is not that obtrusive. In both experiments the current maxima above the Al are 8-10 nA, although the Al strip is apparently more active in **Fig 70** since there are no blue regions on the surface. Nevertheless, after repeating the measurements this was not always unambiguous. That indicates that Al impurities might have a minor role in the increased hydrogen evolution observed in our experiment with $MgCl_2$ discussed in the previous chapter.

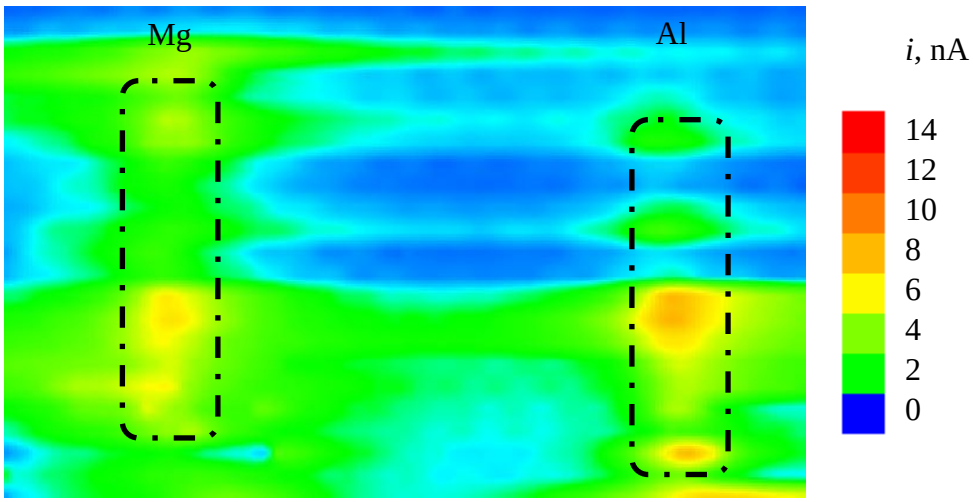

Fig 69. H_2 evolution map recorded above the connected Mg-Al galvanic couple immersed in 2 mM NaCl. Scan dimensions: 2200 µm × 4000 µm.

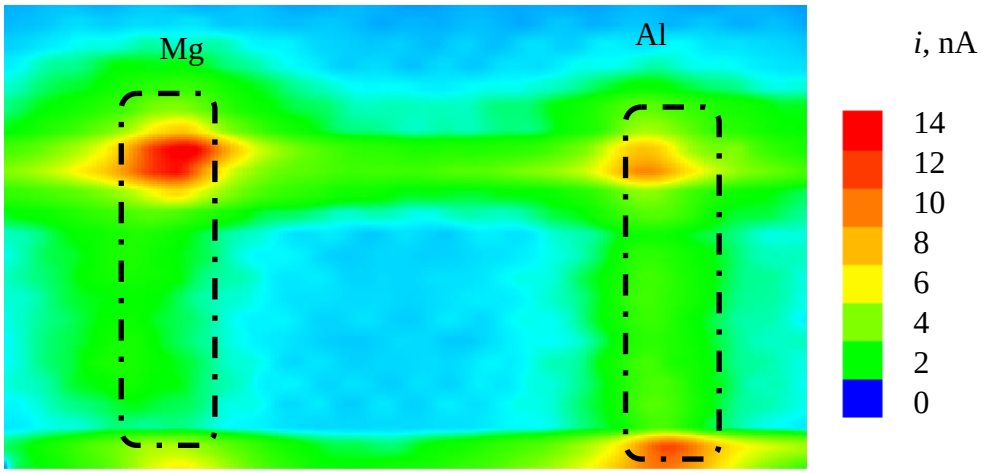

Fig 70. H_2 evolution map recorded above the connected Mg-Al galvanic couple immersed in 1 mM $MgCl_2$. Scan dimensions: 2200 µm × 4000 µm.

III.4.5. Hydrogen evolution on the Mg-Al galvanic couple in the presence of EDTA

In **Section 3.5**, the maps showed very perceptible image of the HER distribution over the magnesium surface when EDTA was added to the solution. The mitigated hydrogen formation was attributed to the hindered formation of the $Mg(OH)_2$ layer. Similarly, the experiments were repeated for the Mg-Al galvanic couple in the presence of EDTA with the purpose to see its effect on the HER. It must be noticed that some works suggest other roles for EDTA in hydrogen evolution. Lov and Wolf found that the increase of EDTA concentration increases the hydrogen evolution rate during the photodissociation of water using colloidal Pt catalyst supported with TiO2 [151]. EDTA served as the sacrificial electron-donor and no hydrogen production was observed in the absence of EDTA. Others said EDTA to be a poison for hydrogen recombination in [152]. In one way or another, the experiment in Chapter 3 had to be further developed to be able to make a fair comparison. Another reason for the modification is as follows. The rate of the galvanic corrosion depends very much on the electrolyte conductivity. Although the differences in the rate of the HER could be seen when the sample was either corroded at its OCP or its potential was controlled by the potentiostat, in the case of galvanic corrosion it was not the case. Hence I decided to create very similar conditions regarding the chloride and EDTA concentration. So in the comparative experiments described here, both electrolytes contained EDTA in 10 mM concentration, but in the first electrolyte, EDTA was inactivated by adding equimolar quantity of $MgCl_2$. In this way, the Mg-EDTA complex is already formed in the test electrolyte and it would be unable to capture the Mg^{2+} formed in the corrosion reaction. The other test solution contained 10 mM EDTA + 20 mM NaCl to maintain the same total Cl^- concentration. **Fig 71A** and **B** show the results for the 2D H_2 mapping experiments in these two electrolytes. In **Fig 71A** much faster hydrogen evolution occurs on the magnesium than on the aluminum. It demonstrated that the circumstances are ideal to study the NDE *in situ*. Both experiments were conducted in 10 mM EDTA, so the concern about the hydrogen recombination poison role could not apply here; instead we can see the pure complexing effect. In the case of **Fig 71B**, both metals produce less H_2, but this time, the HER is dominant on the Al and only slightly mitigated compared to **Fig 71A**. On the other hand, on the surface of magnesium (pure), significantly less H_2 is being evolved. These findings demonstrate that the addition of EDTA affects the HER on the Mg surface and has no significant impact on the cathodic reaction on the Al.

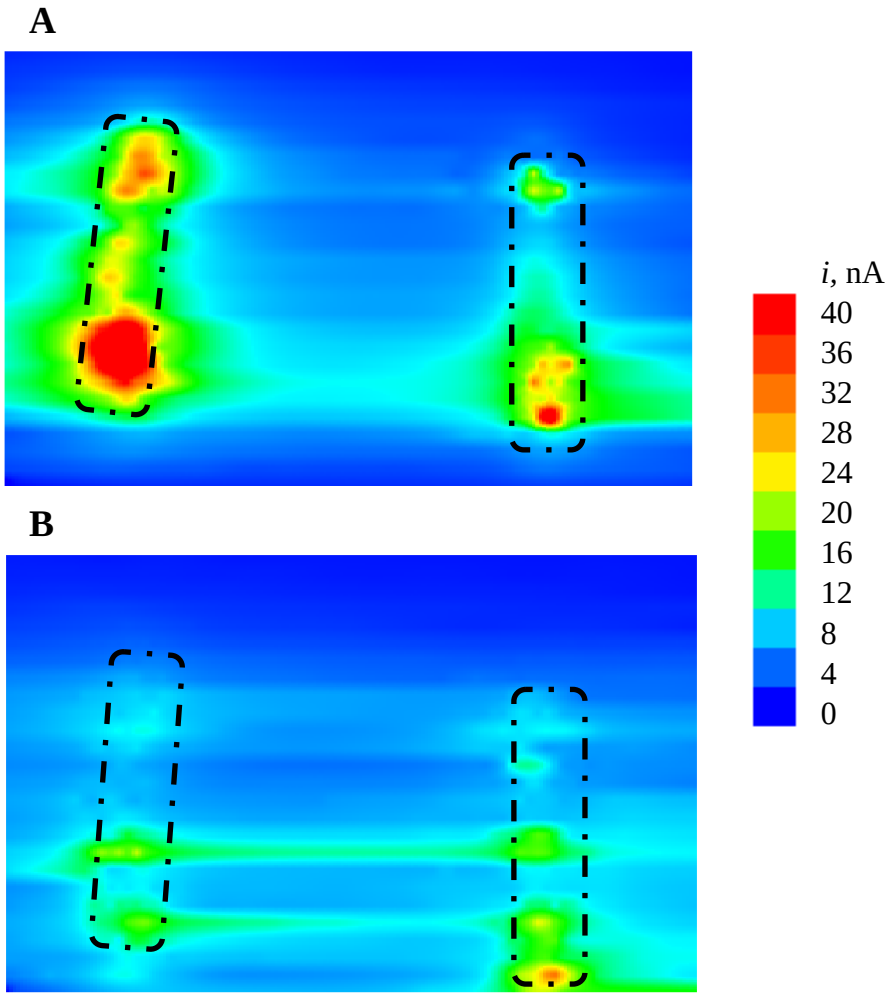

Fig 71. Hydrogen evolution maps recorded above the connected Mg-Al galvanic pair in: (**A**) 10 mM EDTA + 10 mM $MgCl_2$, and (**B**) 10 mM EDTA + 20 mM NaCl. Scan dimensions: 2500 μm × 4000 μm.

Conclusions

This work is aimed to bring attention to new possible and highly selective routes that can facilitate corrosion research. The most important findings are summarized in thesis points, as follows.

1. I have developed and characterized a new Cu^{2+}-selective microelectrode. It was found to be excellent for the potentiometric SECM mapping of Cu^{2+} distributions.
2. Combined double-barrel electrodes containing a Zn ISME and a pH sensitive antimony microelectrode were prepared. Using the double-barrel probes, the possibility of precise tip-sample distance determination and simultaneous detection of Zn^{2+} ions and pH could be achieved
3. I studied the transient signals of ion selective microelectrodes. In quantitative analytical chemistry the long time selectivity coefficient dominates the applicability. It is different in SECM where relatively short time is available to take electrode response. In my experimental work the time dependence of the selectivity that has major importance in SECM was investigated for the first time. In the case of potassium interference of ammonium micro tip, I clearly could show that in SECM care must be taken for finding the right scanning rate that is not disturbed by the time dependent selectivity coefficient.
4. A new evaluation method was introduced to enhance the selectivity of ion selective electrodes in SECM measurements for corrosion applications. It was demonstrated on the Zn^{2+}/Cu^{2+} selective microelectrode containing double-barrel tip developed in this work.
5. I developed and used double-barrel electrodes containing combinations Mg ISME/microreference and Sb/microreference electrodes to minimize the electric field effects in potentiometric mapping, and they showed superior performance over single-barrel electrodes previously reported in the literature. In addition, a new triple-barrel electrode was used in SECM experiments to achieve more realistic simultaneous imaging.
6. I investigated the hydrogen evolution reaction on Mg under different conditions to get insight to the so-called negative difference effect. Interestingly, hydrogen evolution is happening at certain spots on Al/Mg alloy during anodic polarization. The mechanism has been long time debated. The hydrogen evolution reaction on AZ63 and 99% purity Mg was compared using the generator-collector mode of the SECM under different experimental conditions. The results provided new support for the enhanced catalytic activity of the $MgO/Mg(OH)_2$ containing bilayer on the HER.
7. Using the tools developed in my work, I investigated the events on Mg/Al galvanic pair to study the anomalous hydrogen evolution separately on the anodic and cathodic areas. My results could not support the so-called noble impurity theory proposed by several group.

References

[1] E. J. Abbott, F. A. Firestone, D. J. Whitehouse, R. E. Reason, Specifying surface quality, *Mech. Eng.* 55 (1933) 569-572.

[2] J. B. P. Williamson, Microtopography of surfaces, *Proc. Inst. Mech. Eng.* 182 (1967) 21-30.

[3] G. Binnig, H. Rohrer, Scanning tunneling microscopy, *IBM J. Res. Dev.* 30 (1986) 355–369.

[4] A. J. Bard, F. R. F. Fan, J. Kwak, O. Lev, Scanning electrochemical microscopy. Introduction and principles, *Anal. Chem.* 61 (1989) 132-138.

[5] A. Asserghine, D. Filotás, L. Nagy, G. Nagy, Scanning electrochemical microscopy investigation of the rate of formation of a passivating TiO_2 layer on a Ti G4 dental implant, *Electrochem. Commun.* 83 (2017) 33-35.

[6] D. Sidane, O. Devos, M. Puiggali, M. Touzet, B. Tribollet, V. Vivier, Electrochemical characterization of a mechanically stressed passive layer, *Electrochem. Commun.* 13 (2011) 1361–1364.

[7] S. Bergner, P. Palatzky, J. Wegener, F.-M. Matysik, High-resolution imaging of nanostructured Si/SiO_2 substrates and cell monolayers using Scanning Electrochemical Microscopy, *Electroanalysis* 23 (2011) 196–200.

[8] A. Davoodi, J. Pan, C. Leygraf, S. Norgren, The role of intermetallic particles in localized corrosion of an aluminum alloy studied by SKPFM and integrated AFM/SECM, *J. Electrochem. Soc.* 155 (2008) C138-C146.

[9] N. Aouina, F. Balbaud-Célérier, F. Huet, S. Joiret, H. Perrot, F. Rouillard, V. Vivier, Single pit initiation on 316L austenitic stainless steel using scanning electrochemical microscopy, *Electrochim. Acta* 56 (2011) 8589–8596.

[10] Y. Yuan, L. Li, C. Wang, Y. Zhu, Study of the effects of hydrogen on the pitting processes of X70 carbon steel with SECM, *Electrochem. Commun.* 12 (2010) 1804–1807.

[11] D. Ruhlig, H. Gugel, A. Schulte, W. Schuhmann, Visualization of local electrochemical activity and local nickel ion release on laser-welded NiTi/steel joints using combined alternating current mode and stripping mode SECM, *The Analyst* 133 (2008) 1700-1706.

[12] D. Ruhlig, W. Schuhmann, Spatial imaging of Cu^{2+}-ion release by combining alternating current and underpotential stripping mode Scanning Electrochemical Microscopy, *Electroanal*ysis 19 (2007) 191-199.

[13] F. Meng, E. H. Han, J. Wang, Z. Zhang, W. Ke, Localized corrosion behavior of scratches on nickel-base Alloy 690TT, Electrochim. Act. 56 (2011) 1781-1785.

[14] L. Aïnouche, L. Hamadou, A. Kadri, N. Benbrahim, D. Bradai, Interfacial barrier layer properties of three generations of TiO_2 nanotube arrays, *Electrochim. Acta* 133 (2014) 597–609.

[15] M. Janotta, D. Rudolph, A. Kueng, C. Kranz, H. S. Voraberger, W. Waldhauser, B. Mizaikoff, Analysis of corrosion processes at the surface of diamond-like carbon protected zinc selenide waveguides, *Langmuir* 20 (2004) 8634-8640.

[16] K. Eckhard, X. Chen, F. Turcu, W. Schuhmann, Redox competition mode of scanning electrochemical microscopy (RC-SECM) for visualisation of local catalytic activity, *Phys. Chem. Chem. Phys.* 8 (2006) 5359–5365.

[17] B. R. Horrocks, M. V. Mirkin, D. T. Pierce, A. J. Bard, G. Nagy, K. Tóth, Scanning electrochemical microscopy. 19. Ion-selective potentiometric microscopy, *Anal. Chem.* 65 (1993) 1213-1224.

[18] C. Wei, A. J. Bard, I. Kapui, G. Nagy, K. Tóth, Scanning electrochemical microscopy, 32. Gallium ultramicroelectrodes and their application in ion selective probes, *Anal. Chem*. 68 (1996) 2651-2656.

[19] O. Bluh, B. Scott, Vibrating probe electrometer for the measurement of bioelectric potentials. *Rev. Sci. Instrum.* 10 (1950) 867-868.

[20] L. F. Jaffe, R. Nuccitelli, An ultrasensitive vibrating probe for measuring steady extracellular currents, *J.Cell Biol*. 63 (1974) 614-628.

[21] H.S. Isaacs, G. Kissel, Surface preparation and pit propagation in stainless steels, *J. Electrochem. Soc*., 119 (1972) 1628–1632.

[22] A. C. Bastos M. C. Quevedo, O. V. Karavai, M. G. S. Ferreira, Review—On the application of the Scanning Vibrating Electrode Technique (SVET) to corrosion research, *J. Electrochem. Soc*. 164 (2017) C973-C990.

[23] I. L. Rosenfeld, I. S. Danilov, Electrochemical aspects of pitting corrosion, *Corros. Sci.* 7 (1967) 129-142.

[24] S. V. Lamaka, M. Taryba, M. F. Montemor, H. S. Isaacs, M. G. S. Ferreira, Quasi-simultaneous measurements of ionic currents by vibrating probe and pH distribution by ion-selective microelectrode, *Electrochem. Commun.* 13 (2011) 20–23.

[25] A. C. Bastos, O. V. Karavai, M. L. Zheludkevich, K. A. Yasakau, M. G. S. Ferreira, Localised measurements of pH and dissolved oxygen as complements to SVET in the investigation of corrosion at defects in coated aluminum alloy, *Electroanalysis* 22 (2010) 2009-2016.

[26] I. R. Ramos S. B. Valdez, K. R. Zlatev, W. M Schorr, B. M. Carrillo, M. S. Stoytcheva, I. R. Garcia, M. M. Martinez. A virtual instrument for quantitative assessment of pitting corrosion. *Anti-Corros. Method. M.*, 61 (2014) 287 – 292.

[27] R. M. Souto, J. Izquierdo, L. Nagy, S. González,G. Nagy, J. J. Santana. Resolution of the apparent experimental discrepancies observed between SVET and SECM for the characterization of galvanic corrosion reactions *Electrochem. Commun.* 27 **(**2013) 50–53.

[28] W. E. Morf, *The Principles of Ion-Selective Electrodes and of Membrane Transport;* Akadémiai Kiadó: Budapest, 1981.

[29] G. Trümpler, The electromotive behavior of metal compounds with electronic conduction, *Z. Phys. Chem.* 99 (1921) 9-18.

[30] I. M. Kolthoff, H. L. Sanders, Electric potentials at crystal surfaces, and at silver halide surfaces in particular, *J. Am. Chem. Soc.* 59 *(*1937) 416-420.

[31] E. Pungor, E. Hollós-Rokosinyi; Über die Anwendung von membranelektroden bei der Untersuchung von ionenkoncentrazionen, *Acta Chim. Hung.* 27 (1961**)** 63-70.

[32] B. P. Nikolski, M. M. Schultz, *Zh. Fiz. Khim.* 36 (1962) 704.

[33] B. C. Pressman, E. J. Harris, W. S. Jagger, J. H. Johnson, Antibiotic mediated transport of alkali ions across lipid barriers, *Proc. Natl. Acad. Sci.* 58 (1967) 1949-1956

[34] M. S. Frant, J. W. Ross Jr., Electrode for sensing fluoride ion activity in solution, *Science* 154 (1966) 1553–1555.

[35] P. C. Caldwell, An investigation of the intracellular pH of crab muscle fibres by means of micro-glass and micro-tungsten electrodes *J. Physiol. London* 126 (1954) 169–180.
[36] J. L.Walker Jr., Ion specific liquid ion exchanger microelectrodes, *Anal. Chem.* 43 (1971) 89-93.
[37] S. Levy, J. A. Coles, Intracellular pH of Limulus ventral photoreceptor measured with a double-barrelled pH microelectrode *Experientia* 33 (1977) 553–554.
[38] E. R. Gyurcsanyi, A. S. Nyback, K. Toth, G. Nagy, A. Ivaska, Novel polypyrrol based all-solid-state potassium-selective microelectrodes, *Analyst* 123 (1998) 1339–1344.
[39] E. Bakker, P. Bühlmann, E. Pretsch, Carrier-based ion-selective electrodes and bulk optodes. 1. General characteristics, *Chem. Rev*. 97 (1997) 3083−3132.
[40] Y. Umezawa, P. Bühlmann, K. Umezawa, K. Tohda, S. Amemiya, Potentiometric selectivity coefficients of ion-selective electrodes. Part I. Inorganic cations- (Technical Report), *Pure Appl. Chem.* 72 (2000) 1851-2082.
[41] Y. Umezawa, K. Umezawa, P. Buhlmann, N. Hamada, H. Aoki, J. Nakanishi, M. Sato, K. P. Xiao, Y. Nishimura, Potentiometric selectivity coefficients of ion-selective electrodes Part II. Inorganic anions - (IUPAC Technical Report), *Pure Appl. Chem.* 74 (2002) 923-994.
[42] Y. Umezawa, P. Buhlmann, K. Umezawa, N. Hamada, Potentiometric selectivity coefficients of ion-selective electrodes. Part III. Organic ions - (IUPAC Technical Report), *Pure Appl. Chem.* 74 (2002) 995-1099.
[43] E. Bakker, M. Nagele, U. Schaller, E. Pretsch, Applicability of the phase boundary potential model to the mechanistic understanding of solvent polymeric membrane-based ion-selective electrodes, *Electroanalysis* 7 (1995) 817-822.
[44] F.G. Donnan Theorie der Membrangleichgewichte und Membranpotentiale bei Vorhandensein von nicht dialysierenden Elektrolyten. Ein Beitrag zur physikalisch-chemischen Physiologie (The theory of membrane equilibrium and membrane potential in the presence of a non-dialyzable electrolyte. A contribution to physical-chemical physiology), Z. Elektrochem. Angew. 17 (1911) 572-581.
[45] G. Eisenman, in R.A. Durst; *Ion-Selective Electrodes, Nat. Bur. Standards Spec.*, Publ. 314; Washington D.C., 1969.
[46] A. Lewenstam, Construction and response mechanism of sulphide-based ion-selective membrane electrodes, Dissertation, Warsaw University, Poland, 1977.
[47] A. Radu, A.J. Meir, E. Bakker, Dynamic diffusion model for tracing the real-time potential response of polymeric membrane ion-selective electrodes, *Anal. Chem.* 76 (2004**)** 6402-6409.
[48] W. E. Morf, E. Pretsch, N. F. de Rooij, Computer simulation of ion-selective nembrane electrodes and related systems by finite-element procedures, *J. Electroanal. Chem.* 602 (2007) 43-54.
[49] T. Sokalski, P. Lingenfelter, A. Lewenstam, Numerical solution of the coupled Nernst-Planck and Poisson equations for ion-selective membrane potentials, *J. Phys. Chem. B* 107 (2003) 2443-2452.
[50] R. W. Cattrall, I. C. Hamilton, Coated-wire ion-selective electrodes, Ion Sel. Electrode Rev. 6 (1984) 125-172.
[51] A. Cadogan, Z. Gao, A. Lewenstam, A. Ivaska, D. Dermot, All-solid-state sodium-selective electrode based on a calixarene ionophore in a poly(vinyl chloride) membrane with a polypyrrole solid contact, *Anal. Chem.* 64 (1992) 2496–2501.

[52] E. Lindner, Csapadék- és Ionofór Alapú Potenciometriás érzékelők Jelképzése, Dissertation, Budapest, 1993.
[53] M. L. Zheludkevich, S. V. Lamaka, M. G. S. Ferreira, Micropotentiometric mapping of local distributions of Zn^{2+} relevant to corrosion studies, *Electrochem. Commun*. 12 (2010) 394-397.
[54] O. V. Karavai, A. C. Bastos, M. L. Zheludkevich, M. G. Taryba, S. V. Lamaka, M. G. S. Ferreira, Localized electrochemical study of corrosion inhibition in micro-defects on coated AZ31 magnesium alloy, *Electrochim. Acta* 55 (2010) 5401-5406.
[55] A. Kiss, G. Nagy, Deconvolution of potentiometric SECM images recorded with high scan rate, *Electrochim. Acta* 163 (2015) 303-309.
[56] K. Ogle, V. Baudu, L. Garrigues, X. Philippe, Localized electrochemical methods applied to cut edge corrosion, *J. Electrochem. Soc*.- 147 (2000) 3654-3660.
[57] J. Izquierdo, B. M Fernández-Pérez, D. Filotás, Z. Őri, A. Kiss, R. T. Martin-Gómez, L. Nagy, G. Nagy, R. M. Souto, Imaging of concentration distributions and hydrogen evolution on corroding magnesium exposed to aqueous environments using Scanning Electrochemical Microscopy, *Electroanalysis* 28 (2016) 2354-2366.
[58] S. V. Lamaka, O. V. Karavai, A.C. Bastos, M. L. Zheludkevich, M. G. S. Ferreira, Monitoring local spatial distribution of Mg^{2+}, pH and ionic currents, *Electrochem. Commun.* 10 (2008) 259-262.
[59] J. Millar, M. Armstrong-James, Z. L. Kruk, Polarographic assay of iontophoretically applied dopamine and low-noise unit recording using a multibarrel carbon fibre microelectrode, *Brain Res.* 205 (1981) 419-424.
[60] J. Fu, J. F. Lorden, An easily constructed carbon fiber recording and microiontophoresis assembly, *J. Neurosci. Res.* 68 (1996) 247-251.
[61] B. M. Li, Z. T. Mei, K. Kubota, Multibarreled glass-coated tungsten microelectrode for both neuronal activity recording and iontophoresis in monkeys, *Neurochem. Res*. 8 (1990) 214-219.
[62] M. Armstrong-James, K. Fox, Z. L. Kruk, J. Millar, Quantitative ionophoresis of catecholamines using multibarrel carbon fibre microelectrodes, *J. Neurosci. Methods* 4 (1981) 385-406.
[63] E. Ujec, E. E. O. Keller, N. K. V. Pavlík, J. Machek, Low-impedance, coaxial, ion-selective, double-barrel microelectrodes and their use in biological measurements, *Bioelectrochem. Bioenergetics* 7 (1980) 363-369.
[64] P. T. McCarthy, R. Madangopal, K. J. Otto, M. P. Rao, Titanium-based multi-channel, micro-electrode array for recording neural signals, *Conf. Proc. IEEE Eng. Med. Biol. Soc.* 5 (2009) 2062-2065.
[65] A. Piironen, M. Weckström, M. Vähäsöyrinki, Ultrasmall and customizable multichannel electrodes for extracellular recordings, *J. Neurophysiol.* 105 (2011) 1416–1421.
[66] D. J. Walker, S. J. Smith, A. J. Miller, Simultaneous measurement of intracellular pH and K^+ or NO_3^- in barley root cells using triplebarreled, ion-selective micro electrodes, *Plant Physiol*. 108 (1995) 743-751.
[67] J. Izquierdo, L. Nagy, I. Bitter, R. M. Souto, G. Nagy, Potentiometric scanning electrochemical microscopy for the local characterization of the electrochemical behaviour of magnesium-based materials, *Electrochim. Acta* 87 (2013) 283–293.
[68] R. M. Souto, A. Kiss, J. Izquierdo, L. Nagy, I. Bitter, G. Nagy, Spatially-resolved imaging of concentration distributions on corroding magnesium-based materials exposed to aqueous environments by SECM, *Electrochem. Commun.* 26 (2013) 25–28.

[69] N. A. Chaniotakis, J. K. Tsagatakis, E. A. Moschou, S. J. West, X. Wen, Magnesium ion-selective electrode: optimization and flow injection analysis application, *Anal. Chim. Acta* 356 (1997) 105-111.
[70] J. O'Donnell, H. Li, B. Rusterholz, U. Pedrazza, W. Simon, Development of magnesium-selective ionophores, *Anal. Chim. Acta*, 281 (1993) 129-134.
[71] J. Izquierdo, A. Kiss, J. J. Santana, L. Nagy, I. Bitter, H. S. Isaacs, G. Nagy, R. M. Souto, Development of Mg^{2+} ion-selective microelectrodes for potentiometric Scanning Electrochemical Microscopy monitoring of galvanic corrosion processes, *J. Electrochem. Soc.* 160 (2013) C451-C459.
[72] R. M. Souto, A. Kiss, J. Izquierdo, L. Nagy, I. Bitter, G. Nagy, Spatially-resolved imaging of concentration distributions on corroding magnesium-based materials exposed to aqueous environments by SECM, *Electrochem. Commun.* 26 (2013) 25–28.
[73] M. Taryba, S. V. Lamaka, D. Snihirova, M. G. S. Ferreira, M. F. Montemor, W. K. Wijting, S. Toews, G. Grundmeier, The combined use of scanning vibrating electrode technique and micro-potentiometry to assess the self-repair processes in defects on "smart" coatings applied to galvanized steel, *Electrochim. Acta* 56 (2011) 4475–4488.
[74] A. Kiss, D. Filotás, R. M. Souto, G. Nagy, The effect of electric field on potentiometric Scanning Electrochemical Microscopic imaging, *Electrochem. Commun.* 77 (2017) 138-141.
[75] D. R. Curtis, A method for assembly of "parallel" micro-pipettes, *Electroencephalogr. Clin. Neurophysiol.* 24 (1968) 587–589.
[76] B. Carette, A new method of manufacturing multi-barrelled micropipettes with projecting recording barrel, *Electroencephalogr. Clin. Neurophysiol*. 44 (1978) 248–250.
[77] A. R. Crossman, R. J. Walker, G. N. Woodruff, Problems associated with iontophoretic studies in the caudate nucleus and substantia nigra, *Neuropharma* 13 (1974) 547–552.
[78] C. Nicholson, Ion-selective microelectrodes and diffusion measurements as tools to explore the brain cell microenvironment, *J. Neurosci. Met.* 48 (1993) 199–213.
[79] N. Fedirko, N. Svichar, M. Chesler, Fabrication and use of high-speed, concentric H^+- and Ca^{2+}-selective microelectrodes suitable for in vitro extracellular recording, *J. Neurophysiol*. 96 (2006) 919–924.
[80] G. Somjen, R. Dingledine, B. Connors, B. Allen, Extracellular potassium and calcium activities in the mammalian spinal cord, and the effect of changing ion levels of mammalian neural tissues, in: Ion-Selective Microelectrodes and Their Use in Excitable Tissues, E. Sykova, (Ed.), Plenum Press, New York, 1981, pp. 159-180.
[81] D. Filotás, B. M. Fernández-Pérez, J. Izquierdo, L. Nagy, G. Nagy, R. M. Souto, Novel dual microelectrode probe for the simultaneous visualization of local Zn^{2+} and pH distributions in galvanic corrosion processes, *Corros. Sci.* 114 (2017) 37-44.
[82] D. Filotás, B. M. Fernández-Pérez, J. Izquierdo, L. Nagy, G. Nagy, R. M. Souto, Combined amperometric/potentiometric probes for improved chemical imaging of corroding surfaces using scanning electrochemical microscopy, *Electrochim. Acta* 221 (2016) 48–55.
[83] S. V. Lamaka, M. Taryba, M. F. Montemor, H. S. Isaacs, M. G. S. Ferreira, Quasi-simultaneous measurements of ionic currents by vibrating probe and pH distribution by ion-selective microelectrode, *Electrochem. Commun*. 13 (2011) 20–23.
[84] M. G. Taryba, M. F. Montemor, S. V. Lamaka, Quasi-simultaneous mapping of local current density, pH and dissolved O_2, *Electroanalysis* 27 (2015) 2725–2730.
[85] A. Alvarez-Pampliega S. V. Lamaka, M. G. Taryba, M. Madani, J. De Strycker, E. Tourwé, M. G. S. Ferreira, H. Terryn, Cut-edge corrosion study on painted aluminum rich

metallic coated steel by scanning vibrating electrode and micro-potentiometric techniques, *Electrochim. Acta* 61 (2012) 107–117.
[86] T. Yamamoto, Y. Oomura, H Nishino, S. Aou, Y. Nakakao, Driven shield for multi-barrel electrode, *Brain Res. Bull*. 14 (1985) 103-104.
[87] F. Sjöberg, G. Nilsson, Dual mode antimony electrode for simultaneous measurements of pO_2 and pH, Acta Anaesthesiol Scand. 44 (2000) 32-36.
[88] T. B. Abbott: Magnesium: Industrial and research developments over the last 15 years, *Corrosion* 71 (2014) 120-127.
[89] A. Bussy, Mémoire sur le radical métallique de la magnésie, *J. Chim. Méd. Pharm. Toxicol.* 6 (1830) 141.
[90] W. Beetz, On the development of hydrogen from the anode, *Phil. Mag.* 32 (1866) 269-278.
[91] T. R. Thomaz, C. R. Weber, T. Pelegrini Jr., L. F. P. Dick, G. Knörnschild, The negative difference effect of magnesium and of the AZ91 alloy in chloride and stannate-containing solutions, *Corros. Sci*. 52 (2010) 2235-2243.
[92] Z. M. Shi, J. X. Jia, A. Atrens, Galvanostatic anodic polarisation curves and galvanic corrosion of high purity Mg in 3.5% NaCl saturated with $Mg(OH)_2$, *Corros. Sci*. 60 (2012) 296-308.
[93] A. D. King, N. Birbilis, J. R. Scully, Accurate electrochemical measurement of magnesium corrosion rates; A combined impedance, mass-loss and hydrogen collection study, *Electrochim. Acta* 121 (2014) 394-406.
[94] G. Williams, N. Birbilis, H. N. McMurray, The source of hydrogen evolved from a magnesium anode, *Electrochem. Commun*. 36 (2013) 1-5.
[95] G. S. Frankel, A. Samaniego, N. Birbilis, Evolution of hydrogen at dissolving magnesium surfaces, *Corros. Sci*. 70 (2013) 104-111.
[96] N. Birbilis, A. D. King, S. Thomas, G. S. Frankel, J. R. Scully, Evidence for enhanced catalytic activity of magnesium arising from anodic dissolution, *Electrochim. Acta* 132 (2014) 277-283.
[97] S. Fajardo, G. S. Frankel, Effect of impurities on the enhanced catalytic activity for hydrogen evolution in high purity magnesium, *Electrochim. Acta* 165 (2015) 255-267.
[98] G. Song, Recent progress in corrosion and protection of magnesium alloys, *Adv. Eng. Mater*. 7 (2005) 563-586.
[99] E. Ghali, W. Dietzel, K. U. Kainer, General and localized corrosion of magnesium alloys: a critical review, *J. Mater. Eng. Perform*., 13 (2004) 7-23.
[100] R. L. Petty, A. W. Davidson, J. Kleinberg, The anodic oxidation of magnesium metal: evidence for the existence of unipositive magnesium, *J. Am. Chem. Soc*. 76 (1954) 363-366.
[101] A. Samaniego, B.L. Hurley, G.S. Frankel, On the evidence for univalent Mg, *J. Electroanal. Chem*. 737 (2015) 123-128.
[102] S. Fajardo, C. F. Glover, G. Williams, G. S. Frankel, The source of anodic hydrogen evolution on ultra high purity magnesium, *Electrochim. Acta* 212 (2016) 510-521.
[103] S. Fajardo, G. S. Frankel, A kinetic model explaining the enhanced rates of hydrogen evolution on anodically polarized magnesium in aqueous environments, *Electrochem. Commun.* 84 (2017) 36-39.

[104] M. Curioni, The behaviour of magnesium during free corrosion and potentiodynamic polarization investigated by real-time hydrogen measurement and optical imaging, *Electrochim. Acta* 120 (2014) 284-292.
[105] S. H. Salleh, S. Thomas, J. A. Yuwono, K. Venkatesan, N. Birbilis, Enhanced hydrogen evolution on $Mg(OH)_2$ covered Mg surfaces, *Electrochim. Acta* 161 (2015) 144-152.
[106] M. Curioni, J. M. Torrescano-Alvarez, Y. F. Yang, F. Scenini, Application of side-view imaging and real-time hydrogen measurement to the investigation of magnesium corrosion, *Corrosion* 73, 463 (2017).
[107] F. Cao, G.L. Song, A. Atrens, Corrosion and passivation of magnesium alloys, *Corros. Sci.* 111 (2016) 835–845.
[108] M. Esmaily, J. E. Svensson, S. Fajardo, N. Birbilis, G. S. Frankel, S. Virtanen, R. Arrabal, S. Thomas, L. G. Johansson, Fundamentals and advances in magnesium alloy corrosion, *Prog. Mater. Sci.* 89 (2017) 92–193.
[109] J. H. Nordlien, S. Ono, N. Masuko, K. Nisancioglu, Morphology and structure of oxide films formed on magnesium by exposure to air and water, *J. Electrochem. Soc*. 142 (1995) 3320-3322.
[110] M. E. Straumanis, B. K. Bhatia, Disintegration of magnesium while dissolving anodically in neutral and acidic solutions, *J. Electrochem. Soc.* 110 (1963) 357-360.
[111] G. L. Song, A. Atrens, Corrosion mechanisms of magnesium alloys, Adv. Eng. Mater. 1 (1999) 11–33.
[112] G. L. Song, A. Atrens, Recent insights into the mechanism of magnesium corrosion and research suggestions, *Adv. Eng. Mater*. 9 (2007) 177–183.
[113] A. Atrens, M. Liu, N. I. Zainal Abidin, Corrosion mechanism applicable to biodegradable magnesium implants. *Mater Sci Eng B: Solid-State Mater. Adv. Technol.* 176 (2011) 1609–1636.
[114] Z. Shi, J. X. Jia, A. Atrens, Galvanostatic anodic polarisation curves and galvanic corrosion of high purity magnesium in 3.5% NaCl saturated with $Mg(OH)_2$, *Corros. Sci.* 60 (2012) 296–308.
[115] N. T. Kirkland, G. Williams, N. Birbilis, Observations of the galvanostatic dissolution of pure Mg, *Corros. Sci.* 65 (2012) 5–9.
[116] E. J. Casey, R. E. Bergeron, G. D. Nagy, On the mechanism of dissolution of magnesium in aqueous magnesium chloride solutions, *Can. J. Chem*., 40, (1962) 463-479.
[117] C. D. Taylor, A first-principles surface reaction kinetic model for hydrogen evolution under cathodic and anodic conditions on magnesium, *J. Electrochem. Soc.* 163 (2016) C602-C608.
[118] G. L. Makar, J. Kruger, Corrosion studies of rapidly solidified magnesium alloys, *J. Electrochem. Soc*. 137 (1990) 412-421.
[119] S. Bender, J. Goellner, A. Heyn, S. Schmigalla, A new theory for the negative difference effect in magnesium corrosion, *Mater. Corros.* 61 (2011) 1-6.
[120] I. Marco, O. Van der Biest, Polarization measurements from a rotating disc electrode for characterization of magnesium corrosion, *Corros. Sci*. 102 (2015) 384–393.

[121] G. Williams, H. N. McMurray, Localized corrosion of magnesium in chloride-containing electrolyte studied by a scanning vibrating electrode technique, *J. Electrochem. Soc.* 155 (2008) C340-C349.

[122] G. Williams, N. Birbilis, H. N. McMurray, Controlling factors in localized corrosion morphologies observed for magnesium immersed in chloride containing electrolyte, *Faraday Discuss.* 180 (2015) 313–330.

[123] M. Taheri, J. R. Kish, N. Birbilis, M. Danaie, M. A. McNally, J. R. McDermid. Towards a physical description for the origin of enhanced catalytic activity of corroding magnesium surfaces, *Electrochim. Acta* 116 (2016) 396–403.

[124] D. Lysne, S. Thomas, M. F. Hurley, N. Birbilis, On the Fe enrichment during anodic polarization of magnesium and its impact on hydrogen evolution, *J. Electrochem. Soc.* 162 (2015) C396–C402.

[125] S. Fajardo, C. F. Glover, G. Williams, G. S. Frankel, The evolution of anodic hydrogen on high purity magnesium in acidic buffer solution, *Corrosion* 73 (2017) 482–493.

[126] S. Lebouil, O. Gharbi, P. Volovitch, K. Ogle, Mg dissolution in phosphate and chloride electrolytes: insight into the mechanism of the negative difference effect, *Corrosion* 71 (2015) 234–241.

[127] G. S. Frankel, S. Fajardo, B. M. Lynch, Introductory lecture on corrosion chemistry: a focus on anodic hydrogen evolution on Al and Mg, *Faraday Discuss*. 180 (2015) 11-33.

[128] T. W. Cain, I. Gonzalez-Afanador, N. Birbilis, J. R. Scully, The role of surface films and dissolution products on the negative difference effect for magnesium: Comparison of Cl^- versus Cl^- Free Solutions, *J. Electrochem. Soc.* 164 (2017) C300-C311.

[129] D. Hoche, C. Blawert, S. V. Lamaka, N. Scharnagl, C. Mendis, M. L. Zheludkevich. The effect of iron re-deposition on the corrosion of impurity-containing magnesium, *Phys. Chem. Chem. Phys.* 18 (2016) 1279–1291.

[130] M. R. Gennero de Chialvo, A. C. Chialvo, The polarisation resistance, exchange current density and stoichiometric number for the hydrogen evolution reaction: theoretical aspects, *J. Electroanal. Chem.* 415 (1996) 97-106.

[131] L. Rossrucker, A. Samaniego, J.- P. Grote, A. M. Mingers, C. A. Laska, N. Birbilis N, The pH dependence of magnesium dissolution and hydrogen evolution during anodic polarization, *J. Electrochem. Soc.*162 (2015) C333–C339.

[132] G. S. Frankel, A. Samaniego, N. Birbilis, Evolution of hydrogen at dissolving magnesium surfaces, *Corros Sci*. 70 (2013) 104-111.

[133] A. Samaniego, N. Birbilis, X. Xia, G. S. Frankel, Hydrogen evolution during anodic polarization of Mg alloyed with Li, Ca, or Fe, *Corrosion* 71 (2015) 224-233.

[134] N. Birbilis, A. D. King, S. Thomas, G. S. Frankel, J. R. Scully, Evidence for enhanced catalytic activity of magnesium arising from anodic dissolution, *Electrochim. Acta* 132 (2014) 277–283.

[135] S. S. Jamali, S. E. Moulton, D. E. Tallman, M. Forsyth, J. Weber, G. G. Wallace, Applications of scanning electrochemical microscopy (SECM) for local characterization of AZ31 surface during corrosion in a buffered media, *Corros. Sci.* 86 (2014) 93-100.

[136] A. Kiss, G. Nagy, New SECM scanning algorithms for improved potentiometric imaging of circularly symmetric targets, *Electrochim. Acta* 119 (2014) 169-174.

[137] C. Kranz, M. Ludwig, H. E. Gaub, W. Schuhmann, Lateral deposition of polypyrrole lines by means of the scanning electrochemical microscope, *Adv. Mat*. 7 (1995) 38-40.

[138] B. M. Fernández-Pérez, J. Izquierdo, S. González, R. M. Souto, Scanning electrochemical microscopy studies for the characterization of localized corrosion reactions at cut edges of coil-coated steel, *J. Solid State Electrochem*. 18 (2014) 2983–2992.

[139] B. M. Fernández-Pérez, J. Izquierdo, J. J. Santana, S. González, R. M. Souto, Scanning electrochemical microscopy studies for the characterization of localized corrosion reactions at cut edges of painted galvanized steel as a function of solution pH, *Int. J. Electrochem. Sci*. 10 (2015) 10145–10156.

[140] Á. Varga, L. Nagy, J. Izquierdo, I. Bitter, R. M. Souto, G. Nagy, Development of solid contact micropipette Zn-ion selective electrode for corrosion studies, Analytical Letters, 44 (2011) 2876-2886.

[141] S. V. Lamaka, M. G. Taryba, M. L. Zheludkevich, M. G. S. Ferreira, Novel solid-contact ion-selective microelectrodes for localized potentiometric measurements, Electroanal., 21 (2009) 2447-2453

[142] D. R. Lide, *CRC Handbook of Physics and Chemistry*, CRC Press, Boca Raton, FL, 2001.

[143] C. Wei, A. J. Bard, G. Nagy, K. Toth, Scanning Electrochemical Microscopy .28. Ion-selective neutral carrier-based microelectrode potentiometry, *Anal. Chem.* 67 (1995) 1346-1356.

[144] Z. Gao, D. Zhang, X. Li, S. Jiang, Q. Zhang, Current status, opportunities and challenges in chemical conversion coatings for zinc, *Coll. Surf. A: Physicochem. Eng. Aspects* 546 (2018) 221-236.

[145] M. Mokaddem, P. Volovitch, K. Ogle, The anodic dissolution of zinc and zinc alloys in alkaline solution. I: Oxide formation on electrogalvanized steel, *Electrochim. Acta* 55 (2010) 7867–7875.

[146] A. C. Bastos, M.C. Quevedo, M.G.S. Ferreira, The influence of probe vibration and probe movement on SVET measurements, *Corros. Sci*. 92 (2015) 309-314.

147 M. Calugareanu, G. Nagy, A. M. Josceanu, L. Nagy, Ion selective electrodes for microalgal biotechnology, *Rev. Chim.* 64 (2013) 205-209.

[148] S. V. Lamaka, R. M. Souto, M. G. S. Ferreira, In-situ visualization of local corrosion by Scanning Ion-selective Electrode Technique (SIET) in A. Méndez-Vilas, J Diaz, Microscopy: Science, Technology, Applications and Education, 2010, pp. 2162-2173.

[149] S. Thomas, N. V. Medhekar, G. S. Frankel, N. Birbilis, Corrosion mechanism and hydrogen evolution on Mg, *Curr. Opin. Solid State Mater. Sci*. 19 (2015) 85-94.

[150] I. Sanghi, M. Fleischmann, Some potentiostatic studies on zinc, *Electrochim. Acta* 1 (1959) 161-176.

[151] L. Lov, E. E. Wolf, Photo induced hydrogen evolution from water in the presence of EDTA and a Pt/TiO_2 supported catalyst, *Sol. Energ*. 34 (1985) 455-461.

[152] Comment raised by Gerald S. Frankel, the editor of Journal of Electrochemical Society on our manuscript. I would like to take this opportunity to thank him for his comments and suggested corrections.